THE MAGNETIC ACTIVITY, WINDS AND PLANETS OF YOUNG, COOL STARS

A Thesis Submitted by

Belinda A. Nicholson
BSc.(Uni.Melb.), MSc Physics (Uni.Melb.)

For the Award of

Doctor of Philosophy

2018

Abstract

This thesis uses spectropolarimetry to observationally investigate the properties of dynamos and winds of young cool stars, and search for young planets. The techniques of Doppler Imaging and Zeeman Doppler Imaging were used to reconstruct the surface brightness and large-scale magnetic field morphologies of four low-mass weak-line T Tauri stars. The first sample consists of two solar mass stars of different ages, V1095 Sco (1 Myrs) and TWA 9A (10 Myrs). The second sample analysed consists of two 10 Myr old, M-type stars, TWA 25 (0.7 $M_{\odot}$) and TWA 7 (0.4 $M_{\odot}$). Taken together, the reconstructed brightness maps of these young cool stars show a wide variety in their morphologies, as do the reconstructed large-scale magnetic fields. These findings are in agreement with the results of the wider Magnetic Topologies of Young Stars and the Survival of close-in giant Exoplanets (MaTYSSE) large programme, of which this thesis is a part. The variations in radial velocity are examined for all four stars, using the brightness information where available to filter out activity jitter, improving the detection limits for close-in giant planets around these stars.

In addition to this investigation of pre-main sequence stellar dynamos and young planetary systems, a time series of magnetic field observations of the planet-hosting young star τ Boötis spanning more than half a decade - the longest to date - is used to infer changes in the stellar wind, and the resulting potential impacts on the orbiting planet.

In overall terms, this thesis demonstrates that spectropolarimetry is a valuable tool for understanding the magnetic dynamos of young cool stars, modelling stellar winds, and for searching for planets in the presence of stellar activity. In future, spectropolarimetry used as part of radial velocity surveys can advance our understanding of the early evolution of cool stars and their planetary systems.

Certification of Thesis

This Thesis is the work of Belinda A. Nicholson except where otherwise acknowledged, with the majority of the authorship of the papers presented as a Thesis by Publication undertaken by the Student. The work is original and has not previously been submitted for any other award, except where acknowledged.

Student and supervisors signatures of endorsement are held at USQ.

Professor Bradley D. Carter
Principal Supervisor

Doctor Gaitee A. J. Hussain
Associate Supervisor

Doctor Leigh Brookshaw
Associate Supervisor

Doctor Aline A. Vidotto
Associate Supervisor

List of Contributions from Publication Co-authors

This section details contributions by the various authors for each of the papers presented in this thesis by publication.

Chapter 2, Nicholson et al. (2018):

Nicholson, B. A., Hussain, G. A. J., Donati, J.-F., Folsom, C. P., Mengel, M., Carter, B. D., & Wright, D. (2018). The surface magnetic activity of the weak-line T Tauri stars TWA 9A and V1095 Sco. Monthly Notices of the Royal Astronomical Society, 480(2), 1754–1766

Author	Percent Contribution	Tasks Performed
B. A. Nicholson	80	Performed analysis, interpretation, wrote all drafts of paper.
G. A. J. Hussain J.-F. Donati C. P. Folsom M. Mengel B. D. Carter D. Wright the MaTYSSE Collaboration	20	Conception and organisation of MaTYSSE large programme, data acquisition, provision of codes, conception of project, suggested edits to manuscript, assistance with radial velocity analysis

Chapter 3, Nicholson et al. (In Prep.):

Nicholson, B. A., Hussain, G. A. J., Donati, J.-F., Wright, D., Folsom, C. P., Wittenmyer, R.,& Carter, B. D. (In Prep.). The surface magnetic activity of the M-type weak-line T Tauri stars TWA 25 and TWA 7

Author	Percent Contribution	Tasks Performed
B. A. Nicholson	85	Conception of project, data acquisition, performed analysis, interpretation, wrote all drafts of paper.
G. A. J. Hussain J.-F. Donati D. Wright C. P. Folsom R. Wittenmyer B. D. Carter the MaTYSSE Collaboration	15	Conception and organisation of MaTYSSE large programme, data acquisition, provision of analysis codes, conception of project, suggested edits to manuscript, assistance with radial velocity analysis

Chapter 4, Nicholson et al. (2016):

Nicholson, B. A., Vidotto, A. A., Mengel, M., Brookshaw, L., Carter, B., Petit, P., Marsden, S. C., Jeffers, S. V., & Fares, R. (2016). Temporal variability of the wind from the star τ Boötis. Monthly Notices of the Royal Astronomical Society, 459(2), 1907–1915

Author	Percent Contribution	Tasks Performed
B. A. Nicholson	80	Running simulations, performed analysis, interpretation, wrote all drafts of paper.
A. A. Vidotto M. Mengel L. Brookshaw B. D. Carter P. Petit S. C. Marsden S. V. Jeffers R. Fares the BCool Collaboration	20	Conception of BCool project, steering committee of BCool collaboration long term observing project, suggested edits to manuscript, conception of project, running simulations, data acquisition, interpretation, provision of codes

Acknowledgments

Anything I say here is entirely inadequate for how grateful I am to so many people who have supported me over the last four and a half years, but here goes anyway:

First and foremost, a big thank you goes to my Mum, without whom I wouldn't be here, and who has inspired, encouraged and supported me in so many ways to follow my dreams. Thanks also to Coral and Charles for their support and care of me and of Mum over the years.

I thank my Principal Supervisor Brad Carter for his support and encouragement at every stage of this PhD. I also thank my three Associate Supervisors Gaitee Hussain, Aline Vidotto and Leigh Brookshaw for the knowledge, wisdom and individual expertise you have shared with me.

There are many colleagues who have also helped and guided me during my candidature, too many to name them all. A special shout out goes Matthew Mengel, who started his PhD with me, and provided invaluable support and advice on many things both then and now. A shout out also to Jason Grunhut, a mentor and friend during my time at ESO and beyond, and also Duncan Wright for his help and guidance, particularly with Chapter 3.

Thanks also goes out to my wonderful network of friends that have also become family in the different places I have lived. Here in Toowoomba, thanks goes to my housemate Pete Harris, who has been a great friend and support,

especially over the last few weeks. To Anna Balzer and Sharyn Carnahan, who have also shared this PhD journey with me form the beginning, Jake 'Matey Potaty' Clark and Jack Soutter who have shared it with me towards the end, and the wonderful students and fellows at ESO, who shared it with me in the middle, and made Munich feel like home, too! A special mention to Johanna Hartke, for her well-timed messages of encouragement.

During my candidature I have joined various sports clubs (and started one), and they deserve recognition here for helping to keep me sane. A special thanks to Emma and Wendy and my wonderful team mates at Olympus Cheer. Olympus has been a great support network for me from the moment I arrived in Toowoomba, and I am so proud and grateful to be a part of it. Also thanks to the USQ Phoenix Cheerleading team for embracing the club and carrying on the banner (hopefully) long after I am gone. Thanks also goes to the USQ Cougars AFL Senior Women's team for being such a lovely and supportive group, and encouraging me to try new things even when it scares me.

There are so many to thank, and so many I haven't named, but I guess I have to stop somewhere?

Funding acknowledgements:

I have received Australian Commonwealth Government fee contribution for my PhD candidature through the Research Training Program (RTP) Fees Offset scheme.

Contents

List of Figures

(Excluding publications included in Chapters 2-4)

List of Tables

(Excluding publications included in Chapters 2-4)

1 Introduction

1.1 Overview

Cool stars (spectral types late-F or later) are the most abundant type of star in the universe, and are expected to each host at least one planet (Christiansen et al., 2016). Despite their large numbers, many of the processes that govern the formation and evolution of cool stars and their planetary systems are poorly understood. Magnetic fields are understood to play a key role in the formation and evolution for stars and planetary systems, but direct observations of these fields throughout the evolution of young stars has been lacking. Recently, the systematic observation of the magnetic fields of young stars has begun through international large programmes, of which this thesis forms a part. By observing young stars with high-resolution spectropolarimetry, their surface brightness maps and large-scale magnetic field morphologies can be reconstructed and characterised. Furthermore, using the information about

the large-scale magnetic field of a star, the wind properties can be estimated, and the impact on orbiting planets inferred. The same spectropolarimetric observations can be used to search for planets, using the surface brightness information and spectral tracers of activity to help disentangle planetary signals from the behaviour of the host star. The detection and characterisation of planets around young, active stars enables a more complete picture of planetary formation and evolution. This thesis therefore aims to use high-resolution spectropolarimetry to investigate the dynamo generation magnetic fields of young, cool stars, and the potential impacts of these magnetic fields on planetary systems.

1.2 The Early Evolution of Cool Stars: Birth to the Main Sequence

Stars are born from the fragmentation and collapse of molecular hydrogen clouds, and their mass determines what path they take onto the main sequence (Kippenhahn et al., 2012). Stars with masses less than ~2 $M_\odot$ will transition through a T Tauri phase (Carroll & Ostlie, 2007) before entering the zero age main sequence (ZAMS) and main sequence (MS). The T Tauri phase occurs in the later stages of star formation where the star is no longer shrouded by the gas cloud from which it formed, but is still contracting and undergoing evolution in its internal structure towards the main sequence. T Tauri stars (TTS) are separated into two categories: classical T Tauri Stars (cTTS) that are still accreting matter from a surrounding disc of gas and dust, and weak-line T Tauri stars (wTTS) that have cleared their inner disc of gas and have stopped accreting (Bertout, 1989). Both populations of TTSs overlap on the Hertzsprung-Russell (HR) diagram, as demonstrated in Figure 1.1 occupying both the Hayashi track (vertical section of mass tracks), and across onto the Henyey track (horizontal section of mass tracks) for stars > 0.5 $M_\odot$. In practical terms, wTTS and cTTS are typically classified into either category based on the amount of Hα emission in their spectra, quantified by the Hα equivalent width (HαEW). An HαEW of 5 Å is the typical boundary above which a star is classed as a cTTS (Bertout, 1989), as the spectrum is then deemed to contain accretion driven Hα. This boundary increases as a function of decreasing spectral

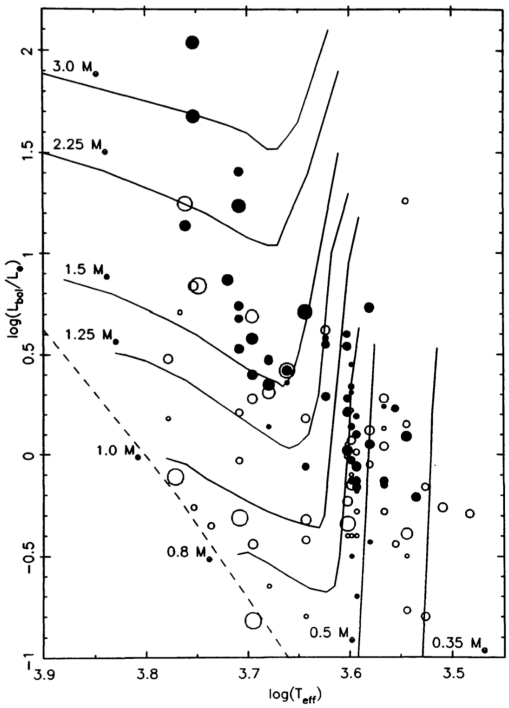

Figure 1.1: Hertzsprung-Russell diagram of a sample of classical (filled circles) and weak-line (open circles) T Tauri stars, with point sizes scaled by $v \sin i$. The solid lines represent theoretical approximate evolutionary mass tracks from Cohen & Kuhi (1979), and the dashed line indicates the transition onto the zero-age main sequence. Figure reproduced from Bertout (1989).

type, as lower mass pre-main sequence (PMS) stars tend to have higher levels of intrinsic Hα emission (Navascués & Martín, 2003). Once the energy from hydrogen burning in the core of the star balances with the gravitational force driving contraction, the star becomes a zero age main sequence star (Kippenhahn et al., 2012), where it will shift marginally in temperature and brightness to eventually become part of the main sequence.

Over these stages of evolution, stars also undergo an evolution in their spin. This is illustrated in Figure 1.2, which shows the simulation by Gallet & Bouvier (2013) of the spin evolution of solar-type stars from the 'birth' to the main sequence. The plot shows separate trajectories for stars that start in different regimes of rotation, with those considered 'rapid' rotators (blue), following a different evolution to those that are 'moderate' (green) or 'slow' (red) rotators. The flat rotation curve at the start is

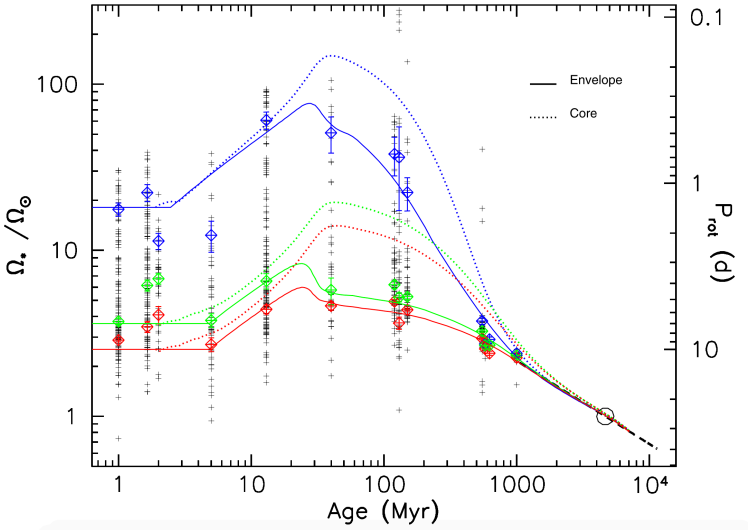

Figure 1.2: Rotation evolution of a solar type star, showing the difference in evolution of stars staring as rapid (blue), moderate (green) or slow (red) rotators. Figure reproduced from Gallet & Bouvier (2013).

where the star is a cTTS still coupled to its disc, keeping the rotational velocity constant. Once the star has decoupled from the disc and is a weak-line T Tauri, it spins up as it contracts toward the main sequence. At the peak of these rotation curves is when the star reaches the ZAMS and begins its rotational breaking caused by strong magnetic fields and stellar winds, until the main sequence where the different rotation curves converge and follow the Skumanich relation of rotation decreasing with age as $\Omega \propto t^{-1/2}$ on the main sequence (Skumanich, 1972).

Stellar magnetic activity and rotation are intimately linked. Rapid rotation drives stronger magnetic fields, and in turn the strong magnetic fields break stellar rotation through the stellar wind, as seen in the downward slope in the later half of Figure 1.2. Figure 1.3 is an example of this activity rotation relation for a sample of M dwarfs from Newton et al. (2017). In this figure, activity is parameterised as the luminosity in Hα luminosity relative to an inactive star, and rotation is parameterised by the Rossby Number, R_o, which is defined as the rotation period divided by the convective turnover time - the duration of one convention cycle, derived from either modelling of stellar interiors, or semi-empirical relations with colour or stellar mass (Gray, 2008; Wright et al., 2011). This figure demonstrates the increase in activity with decreasing

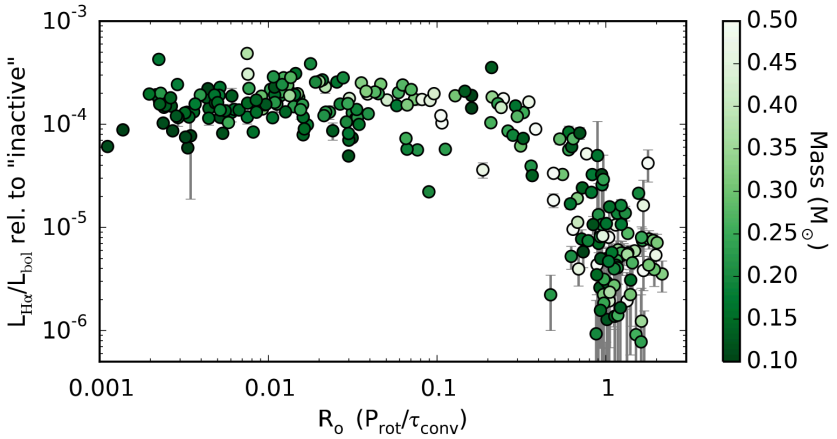

Figure 1.3: Activity-Rotation relation for a sample of M dwarfs. Activity is parametrised as Hα luminosity relative to an inactive star, and rotation is parametrised as the Rossby number, R_o. This plot demonstrates the saturation in activity at low R_o (high rotation). Figure reproduced from Newton et al. (2017).

Rossby number, down to $R_o = 0.1$ where the activity level saturates. This saturation point is also observed in other magnetic activity indicators across the cool star population, such as the magnetic field strength (see e.g. Donati & Landstreet, 2009) and X-ray luminosity (see e.g. Wright et al., 2018).

1.3 Stellar Magnetism

Magnetic fields are known to strongly influence stellar evolution, from the controlling of accretion onto the stellar surface in the classical T Tauri phase, to driving mass loss and angular momentum loss at all stages of stellar evolution (Gallet & Bouvier, 2013). The work to understand the generation of magnetic fields in cool stars is still ongoing. Even for the best studied star, the Sun, there is no consensus on a model to describe the solar dynamo (Brun & Browning, 2017), let alone for other stars for which there are fewer observational constraints.

Many models for describing stellar dynamos have originated from the magnetic induction equation derived from mean field theory. A summary and derivation of this, as well as an extended discussion on dynamos can be found in Brun & Browning (2017). These classical dynamo models are classified by the location of the origin of

the field within the star, and which of the first two terms in the induction equation (equation 13 in Brun & Browning, 2017) dominates the production of poloidal and toroidal fields. The first term in the induction equation represents the motions of the large-scale field by meridional flows, or differential rotation (the Ω effect). The second the term, called the α effect, describes the conversion between poloidal and toroidal field by the lifting and twisting of magnetic flux by convection and Coriolis forces.

The solar dynamo is typically described as an interface layer $\alpha - \Omega$ dynamo (Parker, 1993; Charbonneau & MacGregor, 1997), where the origin of the toroidal field generated by the ω effect lies at the interface between the radiative core and convective envelope, called the tachocline. In this dynamo model, the α effect then transforms the toroidal field back to a poloidal field with the opposite polarity of the original poloidal field. This dynamo model agrees well with many phenomena observed in our Sun, such as the cyclic polarity reversals, and the numbers and locations of spots over the Solar cycle (Charbonneau & MacGregor, 1997).

Some stars exhibit little or no differential rotation, i.e. appear to rotate as solid bodies. For stars with no differential rotation, the changes in the field can be described by an α^2 model, where the α effect is the source for both the poloidal and toroidal fields, producing either steady or cyclical fields depending on the circumstances (Rüdiger et al., 2003).

In recent years, 3D magnetohydrodynamic (MHD) simulations have been employed to expand beyond the models from mean field theory, and simulate more completely the Solar dynamo (see e.g. Hotta et al., 2016), and other solar-like main sequence stars (see e.g. Guerrero et al., 2016). However, there have been few studies specifically simulating the dynamos in PMS cool stars as they evolve onto the main sequence. A recent attempt by Emeriau-Viard & Brun (2017) finds broad agreement with the observations of magnetic field morphology across the PMS section of the HR digram from the Magnetic Protostars and Planets[1] (MaPP) program, namely that stars without or with very small radiative cores exhibit large, poloidal, axisymmetric fields, but form weaker, non-axisymmetric fields as the radiative core becomes larger than half the stel-

[1] https://wiki.lam.fr/mapp/FrontPage

lar radius (Gregory et al., 2012). This model, however only follows the evolution of a 1 $M_{\odot}$ star on the slow rotation track described by Gallet & Bouvier (2013), and so does not address the evolution of lower mass stars that remain fully convective, or those that form as rapid rotator. The agreement of these simulations to observations of wTTS is explored in this thesis and discussed in Chapter 5.

1.4 Observing Stellar Magnetic Activity

Stellar magnetic activity can be observed in a multitude of ways, due to the variety of phenomena caused by the stellar magnetism. Stellar activity is typically measured using activity indicators in stellar spectra: particular regions of spectra that vary due to magnetic activity through various physical processes. Stellar activity is also indicated by the presence and amount of dark spots or bright regions on the surface, which can be mapped using Doppler Imaging. In addition, the large scale magnetic fields themselves can be reconstructed using high resolution spectropolarimetric observations through the technique of Zeeman Doppler Imaging. These complementary methods of probing stellar activity are described below. This thesis will concentrate on optical methods for measuring stellar activity, though activity is also studied at X-ray or radio wavelengths.

1.4.1 Activity Indicators

The depth, width and shape of absorption lines in stellar spectra probe the physical environment in which they are made. Different spectral lines can be sensitive to different aspects of that environment, such as the temperature, pressure, plasma velocity, and the stellar magnetic field (Gray, 2008). There are a handful of lines that are of particular interest for stellar and exoplanet astronomy due to their known sensitivity to stellar activity.

One activity tracer that is widely used is the Ca II H and K lines (λ3968.47 Å and λ3933.66 Å). These lines are created in the lower chromosphere, and are well correlated with chromospheric activity caused by the stellar magnetic fields, and as such are

used as a proxy for measuring stellar magnetic cycles, as well as for comparing activity levels between stars (see e.g. Noyes et al., 1984; Boisse et al., 2009). It is typically quantified as the S-index, which is calculated as the ratio of the flux in each line over a defined bandpass and calibrated to the Mt. Wilson catalogue, or the log R'_{HK} index, which is corrected for photospheric flux. However, this line is not used for stars with B-V colours greater than 1.2 due to a lack of calibration (Gomes da Silva et al., 2011), and in faint, cool stars where there is little flux in this end of the spectrum, as is the case for this thesis.

The hydrogen Balmer lines, and more specifically Hα is another common, if imperfect, activity indicator, indicative of magnetic activity in the upper chromosphere of cool stars. However, given the ubiquity of hydrogen in stars, it is also sensitive to other physical processes. For young and active stars, such as T Tauri stars, Hα can indicate mass motions to and from the star, such as stellar winds indicated with a P Cygni profile shape in the line, or accretion onto the stellar surface, typically indicated by very high emission.

The Na I Doublet (λ5895.92 Å and λ5889.95 Å) is known to be a tracer of activity in stars with $(B - V) \geq 1.1$ (Díaz et al., 2007). It is formed between the lower-to-middle chromosphere, and so complements the Ca II H and K and Hα lines (Mauas, 2000). Díaz et al. (2007) caution that the relation between the Na I doublet index and the chromospheric activity as measures by Ca H&K differs from star to star, and so should be used only for monitoring changes in activity for a given stars, and not for comparing activity levels between stars. However, Gomes da Silva et al. (2011) do find a correlation between the mean Na I doublet index and S-index for a sample of M-dwarfs surveys as part of the HARPS planet search. Given this, the Na doublet is used to monitor the surface activity of the two M-type stars in this thesis.

Lastly, the behaviour of the He I D_3 line (λ5875.62 Å) is considered, but only in the context of a possible flaring event. Whilst it does appear to be correlated with the presence of plage (Landman, 1981), Gomes da Silva et al. (2011) found it to only correlate weakly with activity in low mass stars.

Used in combination, these activity indices serve in this thesis to trace patterns of

activity on the stellar surface by inspecting their variation with rotation, and complements the surface brightness, and radial velocity analysis.

1.4.2 Mapping large-scale Surface Brightness

Stars, particularly those that are very active, are not uniform in brightness, but display brighter (plage) or darker (spot) regions on the stellar photosphere. These features are intimately tied with the stellar magnetic field, which can suppress convection in some areas causing spots (Berdyugina, 2005), or excite regions in the upper chromosphere and photosphere causing plages (Lean, 1997). As the magnetic field on a star changes, so do the presence of spots and plages. These brightness inhomogeneities can be observed in great detail on the Sun, which undergoes an 11 year cycle of changing spot frequency and location (Babcock, 1961).

Despite stars being generally unresolved point sources, we are able to infer their large-scale surface brightness topologies using the technique of Doppler Imaging (DI). By taking multiple high-resolution spectra at different stellar rotational phases, we are able to reconstruct bright and dark areas on the surface by examining changes in the shape of absorption lines with stellar rotation. Despite the signal of the surface brightness inhomogeneities being small in a single absorption line, a least squares deconvolution (LSD) is typically performed to combine the lines together and increase the signal-to-noise ratio (SNR), producing an LSD profile (see Donati & Brown, 1997, for more details). A time series of LSD profiles is then used for the surface brightness reconstruction. A schematic illustration of DI is given in Figure 1.4. This shows the changes in an LSD profile as the spot moves across the stellar surface.

The resolution of the reconstructed image is dependent on the $v \sin(i)$ of the star: the greater the degree of rotational broadening projected along the line of sight, the more spatial information can be probed, at a given instrumental resolution. The lower limit of $v \sin(i)$ for DI is the point at which rotation is no longer the dominant form of broadening in the line. Additional broadening sources, such as microturbulence and macroturbulence, are temperature and gravity dependent, and so this limit varies according to the spectral type of a star. In low mass stars, the broadening contribution

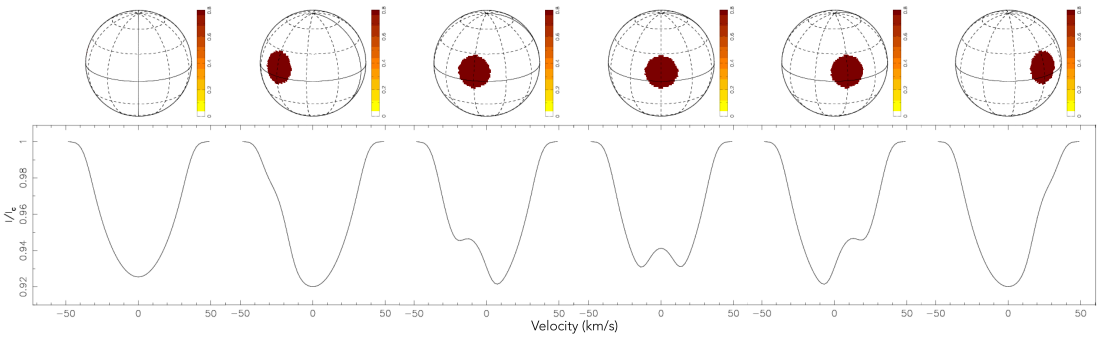

Figure 1.4: An illustration of the effect of an idealised spot (illustrated on the sphere) on the shape of LSD intensity profiles (line below the sphere), and the change in shape of the LSD as the spot moves across the line of sight. Figure is as adaptation of an animation by Donati et al. (2015)

of microturbulence is about 1-2km/s, and the contribution of radial-tangential macroturbulence is around 3km/s (Gray, 2008). In practice, however, the instrumental resolution limits this further, with the lower limit of $v \sin(i)$ for active stars being around 10 km/s or higher. In the MaTYSSE program, the system with the lowest $v \sin(i)$ for which brightness maps could be produced had a $v \sin(i)$ of 9.5 km s^{-1} (Donati et al., 2015).

The timing of observations for reconstructing the large-scale brightness is crucial. The total time span of a given set of observations used for a single reconstruction must be shorter than the evolutionary timescale of the stellar surface features, which is typically a few weeks to a few months for cool stars (Giles et al., 2017). In addition, the observations should be ideally spaced to sample the rotation period well, ideally at least ten phases covering the rotation cycle as evenly as possible. For more rapid rotators where higher spatial resolution is possible more phases are advantageous. Additionally, targets need to be bright enough relative to their rotation, so that the length of an exposure is not a significant fraction of their rotation cycle so as to avoid blurring out the surface features. While the $v \sin(i)$ constraints limit DI, it provides a uniquely useful way to observe stellar active regions for stars with at least moderate rotation rates.

1.4.3 Line-of-Sight Magnetic Field

Stellar magnetic fields can be observed and measured by the effect they have on absorption features in the stellar spectrum. In the presence of a magnetic field, the energy levels of atomic transitions split, and thus splitting the observed absorption features. This phenomenon is known as the Zeeman Effect, and was first observed in stars by Babcock (1947) in the chemically peculiar star 78 Vir. The line splitting width, in velocity space, is given by:

$$\Delta v = 1.4 \lambda_0 g B, \tag{1.1}$$

were λ_0 is the wavelength of the unspilt transition, B is the magnetic field strength, and g is the Landé factor, which characterises the sensitivity of a given transition to a magnetic field (Reiners, 2010). An illustration of the Zeeman effect is given on the left-hand panel of Figure 1.5, reproduced from Reiners (2010). Here the transition that remains the same in energy in the presence of a magnetic field is denoted π, and the two components that do change are denoted σ. In stars, this effect is observed as a characteristic broadening of the line, as other effects such as thermal and Doppler sources of broadening prevent a clear separation of the energy levels. By measuring the degree of broadening, the unsigned average magnetic field strength $\langle B \rangle$ can be measured. Given the wavelength dependance of the Zeeman effect, Zeeman broadening measurements are easier at infrared wavelengths.

Another method to observe magnetic fields is by measuring the polarisation in the stellar absorption lines. Polarised light can be described using the Stokes vector [I, Q, U, V], where I is the total intensity of the light, U and Q are the two linear polarisation states, and V is the circular polarisation (Donati & Landstreet, 2009). The polarisation of light due to the Zeeman effect is illustrated in the right hand panel of figure 1.5. The π component is always linearly polarised, where as the σ components are seen to be linearly or circularly polarised depending on the line of sight to the magnetic field (Reiners, 2012). In practice, the Stokes V component of polarisation is preferentially observed, as the Zeeman signatures in Stokes Q and U are much smaller and harder to detect than in Stokes V (Reiners, 2012).

Observations of Zeeman signatures in circularly polarised light are done as a set of 4 exposures. The orientation of a quarter wave plate is alternated between exposures, with exposure 1 and 4 set with one alignment, and 2 and 3 set as the opposite alignment (Petit et al., 2003). This is done to remove any instrumental polarisation as a systematic error in the observations. From these exposures, the unpolarised Stoke I spectrum is calculate by summing all the spectra together, and the Stokes V spectrum is calculated by constructively adding the polarisation states (Donati et al., 1997). A null spectrum is also generated by destructively adding the polarised spectra (Donati et al., 1997), and is used to assess if any residual spurious sources of signal remain (Bagnulo et al., 2009). The signal of a Zeeman signature in Stokes V is small compared to the overall spectral intensity. To improve the SNR for Stokes V detections, lines are combined using LSD, including a weighting for the Landé factor to account for the sensitivity of each line to the magnetic field (Donati et al., 1997).

From the Stokes V Zeeman signatures, an averaged line-of-sight, or longitudinal, magnetic field, B_l can be calculated as an integration of the line. This thesis uses the method of Mathys (1989); Donati et al. (1997), where B_l is calculated as:

$$B_l = -\frac{2.14 \times 10^{11}}{\lambda g c} \frac{\int (v - v_0) V(v) \mathrm{dv}}{\int [1 - I(v)] \mathrm{dv}}, \tag{1.2}$$

where $I(v)$ and $V(v)$ are the Stokes I and V LSD profiles as a function of velocity, v_0 is the central velocity, c is the speed of light, and λ and g are the mean wavelength and Landé factor of the LSD profiles. This measurement is a lower limit of the total field at a given line of sight, as areas of opposite polarity will cancel. In this way, B_l is limited in what it can probe about the stellar magnetic field. However, longitudinal field measurements are useful for measuring the rotation period of the star. In addition, there can be a strong rotational modulated B_l signal without a signal present in the spectral indices (see Chapter 3 for an example), making it another useful indicator for stellar sources of radial velocity signals.

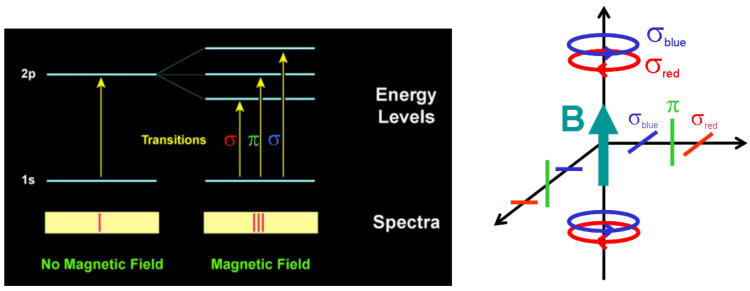

Figure 1.5: Illustration of Zeeman splitting (left) and the induced polarisation (right), reproduced from Reiners (2010)

1.4.4 Mapping Large-Scale Magnetic Fields

The large-scale magnetic fields of stars can be mapped using the technique of Zeeman Doppler Imaging (ZDI) (Semel, 1989; Brown et al., 1991; Semel et al., 1993). ZDI is a uniquely useful technique for observing and mapping stellar magnetic field, and so has provided the observational basis for numerous stellar dynamo studies. ZDI originated in the late 1980's and early 90's, and has since been employed to survey stellar magnetic fields across the HR diagram, through a range of international collaborative programs, such as BCool (Marsden et al., 2014), TouPIES (Folsom et al., 2016; Folsom et al., 2018), MaPP (e.g. Donati et al., 2008) and MaTYSSE (e.g. Donati et al., 2015).

ZDI measures and reconstructs the large-scale surface magnetic fields based on the shape and size of Zeeman signatures in Stokes V line profiles. The size and shape of a Zeeman signature in Stokes V, and the way these signatures change with stellar rotation, encodes information about surface magnetic features, such as their size, field strength, orientation (radial, azimuthal or meridional) and sign (positive or negative).

To reconstruct the large-scale fields, observations are taken over several consecutive stellar rotations, covering as many phases as possible to best constrain the field morphology, as well as estimate any surface differential rotation. The field is then reconstructed by solving for the map with the minimum information (maximum entropy) that reproduces the observed Stokes V profiles, within the level of noise in the data. This thesis uses the ZDI code ZDIPy by Folsom et al. (2018), which is based on the ZDI code of Donati et al. (2006). In this code, as with most modern ZDI codes, the magnetic field is described as a series of spherical harmonics. This allows a quantitative

analysis of the magnetic field topology, by allocating amounts of energy to different harmonic components. The implementation of the ZDI code employed in this thesis has been calibrated against the code of Donati et al. (2006) and reconstructions compared with the zDOTS ZDI code (Hussain et al., 2000, 2016).

For a more detailed analysis and summary of the technique of ZDI and its scientific outcomes, see the review papers by Donati & Landstreet (2009), Reiners (2012) and Brun & Browning (2017).

1.4.5 Measuring Differential Rotation

The latitude dependence of stellar surface rotation, i.e. differential rotation, provides an important empirical constraint on stellar dynamo models. Differential rotation is a technically challenging measurement that is achieved through the process of Doppler and Zeeman Doppler Imaging (see e.g. Petit et al., 2002; Donati et al., 2003). Through using a time series of high signal to noise Stokes I or V LSD profiles that typically span multiple rotation periods, the surface brightness and magnetic field maps are solved as an inverse problem, incorperating the surface differential rotation needed to best reproduce the observed profiles. Calculation of a unique reliable differential rotation measurement depends on the signal to noise, completeness of the phase coverage and the number of rotations observed (Mengel, 2017).

1.5 Stellar Winds and Exoplanetary Systems

The direct observation of winds from cool stars is beyond present techniques and technologies, as the wind is too diffuse to view directly (Wood, 2004). In very active and young stars, the interaction of the wind with the interstellar medium (ISM) is only observable in cases of very young active stars with very strong winds, where excess blue-ward absorption can be seen in Lyα (λ1216 Å, Wood, 2004), or in cases where this interaction is strong enough to emit X-rays (Wargelin & Drake, 2001). Strong stellar winds can also be observed in Hα emission spectra of hot stars, as well as red

giants and super-giants by a characteristic P Cygni shape in the line profile (Wood, 2004). For solar-type main sequence stars, direct observation remains impossible, so estimates of the wind properties are done through simulations.

The information gained about the large-scale magnetic fields from ZDI can be used to estimate the properties of the stellar wind and its impact on the formation and evolution of planetary systems. By applying the magnetic field information from ZDI to magnetohydrodynamic solar wind simulation codes, the wind properties of other stars can be estimated. ZDI has thus given rise to a number of stellar wind studies, with a particular focus on stellar evolution, and planetary evolution and habitability.

With the availability of long term ZDI observations for some stars, it is now possible to estimate the changes in wind properties throughout a stellar magnetic cycle, and the resulting impact on exoplanet space weather.

This thesis uses the 3D MHD Block-Adaptive-Tree Solar Wind Roe-type Upwind Scheme (BATS-R-US, Powell et al., 1999; Tóth et al., 2005, 2012) code to simulate the wind for several epochs of ZDI observations. BATS-R-US was originally written as a Solar wind simulation, using magnetograms from Solar observations and measurements of the solar coronal properties. Today, BATS-R-US is still extensively used to simulate Solar wind phenomena (see e.g. Walsh et al., 2018), but in recent years has been adapted to model stellar winds (Alvarado-Gómez et al., 2016; Vidotto & Donati, 2017, see e.g.). The modelling in this thesis builds on the work of Vidotto et al. (2012) and Vidotto et al. (2014).

1.6 Exoplanets Around Active Stars

The sample of confirmed exoplanets to date are almost exclusively orbiting stars of low activity. This is deliberate, as stellar activity can obscure and mimic planetary signals. This is particularly a problem in the two most common methods for exoplanet detection, transit photometry and radial velocity, as both rely on studying stellar behaviour to infer the presence of a planet. The radial velocity method relies on accurately measuring shifts in the wavelength of absorption features in stellar spectra. The variations

in surface brightness can skew the absorption lines, which can be mistakenly measured as a shift in wavelength. These apparent shifts then change as the star rotates and different surface features come into and out of the line of sight. In this way, a signal can be induced in the radial velocity data, typically on the same period as the stellar rotation, or an alias of the stellar rotation period. On very active stars, these surface features are sometimes so large that the amplitude of the stellar activity signal in the radial velocities can exceed that of even a close in giant planet.

This activity presents a problem for trying to understand planet formation and migration timescales. Young stars are very active making it difficult to find and characterise newly formed and evolving planetary systems. In recent years, however, there has been some success in using radial velocities to detect planets around young, active stars. This success is due to the development of techniques to characterise, and hence mitigate, these stellar activity signals in radial velocity data. Donati et al. (2014) developed a method to remove the influence of large stellar activity on radial velocity curves by using the surface brightness information gained from DI to measure the radial velocity contribution of the surface spots and plage, and subtract it from the observed radial velocities. With this method there have been two young exoplanet discoveries, one each around V830 Tau (Donati et al., 2016, 2017), and TAP 26 (Yu et al., 2017). This thesis applies the method of Donati et al. (2014) to the sample of wTTSs presented here to search for young, close-in giant planets, and so further investigate the occurrence rate of these types of planets around young stars.

There are two methods of measuring stellar radial velocities used in this thesis. The first and most widely used method in this thesis follows that Donati et al. (2014), and is based on measurement of the first order moment of the Stokes I LSD profiles. This first order moment is calculated as:

$$RV = \frac{\sum v(1 - I(v))}{\sum 1 - I(v)}, \tag{1.3}$$

where v is the velocity at each point in the Stokes I LSD profile, $I(v)$. This same equation is applied to the Doppler Imaging fit to the Stokes I profiles to quantify the con-

tribution of surface brightness inhomogeneities to the stellar radial velocity measurement. The uncertainties in our radial velocities are calculated as per the method of Butler & Marcy (1996),

$$\sigma_{RV} = \frac{1}{\sqrt{\sum \left(\frac{dI(v)/dv}{\sigma_I} \right)^2}}, \tag{1.4}$$

where σ_I is the uncertainty in each Stokes I point (points in the DI fit spectrum are taken as having zero error). This uncertainty estimate is the intrinsic Doppler error over the LSD profile, and does not include systematic sources of error such as instrumental error, or any error introduced by the data reduction and creation of the LSD profile.

The second method of radial velocity analysis was used for the spectra of TWA 7 to achieve a better radial velocity precision. This involves taking the HARPS pipeline reduced data, resampling it to a uniform velocity step of 300 m s^{-1} and creating a mean of all spectra. Each observed spectrum was then cross-correlated with the mean spectrum, creating a time-series of cross-correlation functions (CCFs). These CCFs are similar in to LSD profiles in that they represent a type of averaged line (although additionally broadened by the intrinsic broadening of the mean spectrum), but with smaller uncertainties than LSD profile and hence providing more precise radial velocities. CCFs however do not preserve line shape well, and hence are not used for DI and ZDI. The radial velocities are measured in the CCFs by fitting a Generalised Gaussian Distribution. This method is similar to that of Baranne et al. (1996); Pepe et al. (2002), but uses a mean spectrum as the template. The uncertainties in these radial velocities are calculated according to the method of Butler & Marcy (1996) as described above, applied to the CCFs.

1.7 Structure of this thesis

Given the preceding discussion, the aim of this thesis is to use high-resolution spectropolarimetry to explore the dynamo magnetic fields of young stars, and how this affects stellar evolution and the evolution or their planetary systems. In Chapter 2 I

explore what spectropolarimetry of two Solar-mass wTTSs at 2 Myrs and 10 Myrs can tell us about the evolution of the young stellar dynamo. In addition to this, a search for young planetary companions is made. In Chapter 3 I expand this sample to explore the changes in young stellar dynamos with mass, including the lowest mass wTTS observed to date. In addition, a search for young planetary companions is made. In Chapter 4, I apply the information gained from a time series of ZDI observation of the large scale fields to estimate the winds properties of a 1 Gyr Solar-type star, τ Boötis. From this I infer the expected impacts of the wind and activity on the close-in giant planet τ Boo b. Finally, in Chapter 5 I bring together the results of Chapters 2, 3 and 4 to offer conclusions as to the nature of the dynamos in young cool stars and the potential impacts of winds on stellar and planetary evolution.

2

The Surface Magnetic Activity of the Weak-Line T Tauri Stars TWA 9A and V1095 Sco

Published in the Monthly Notices of the Royal Astronomical Society, 2018, Volume 480, pp. 1754–1766

Monthly Notices of the ROYAL ASTRONOMICAL SOCIETY

MNRAS **480,** 1754–1766 (2018) doi:10.1093/mnras/sty1965
Advance Access publication 2018 July 25

The surface magnetic activity of the weak-line T Tauri stars TWA 9A and V1095 Sco

B. A. Nicholson,[1,2]★ G. A. J. Hussain,[2,3,4] J.-F. Donati,[3,4] C. P. Folsom,[3,4] M. Mengel,[1] B. D. Carter,[1] D. Wright[1] and the MaTYSSE collaboration

[1]*University of Southern Queensland, Computational Engineering and Science Research Centre, Toowoomba, Australia*
[2]*European Southern Observatory, Karl Schwarzschild Str. 2, D-85748 Garching, Germany*
[3]*Univ. de Toulouse, UPS-OMP, IRAP, 14 av Belin, F-31400 Toulouse, France*
[4]*CNRS, IRAP / UMR 5277, 14 av Belin, F-31400 Toulouse, France*

Accepted 2018 July 16. Received 2018 July 9; in original form 2018 May 4

ABSTRACT

We present a detailed analysis of high-resolution spectropolarimetric observations of the weak-line T Tauri stars (wTTSs) TWA 9A and V1095 Sco as part of a wider survey of magnetic properties and activity in weak-line T Tauri stars, called MaTYSSE (Magnetic Topologies of Young Stars and the Survival of close-in giant Exoplanets). Our targets have similar masses but differing ages which span the stage of radiative core formation in solar-mass stars. We use the intensity line profiles to reconstruct surface brightness maps for both stars. The reconstructed brightness maps for TWA 9A and V1095 Sco were used to model and subtract the activity-induced jitter, reducing the RMS in the radial velocity measurements of TWA 9A by a factor of ∼7, and for V1095 Sco by a factor of ∼3. We detect significant circular polarization for both stars, but only acquired a high-quality circular polarisation time-series for TWA 9A. Our reconstructed large-scale magnetic field distribution of TWA 9A indicates a strong, non-axisymmetric field. We also analyse the chromospheric activity of both stars by investigating their H α emission, finding excess blue-ward emission for most observations of V1095 Sco, and symmetric, double-peaked emission for TWA 9A, with enhanced emission at one epoch likely indicating a flaring event.

Key words: magnetic fields – techniques: polarimetric – stars: formation – stars: imaging – stars: individual: TWA 9A – stars: individual: V1095 Sco.

1 INTRODUCTION

Magnetic fields play an important role in the evolution of stars, particularly in the pre-main sequence stages. As a star evolves from a protostar obscured by a cloud of dust, it emerges as a young classical T Tauri Star (cTTS), accreting matter from a surrounding disc of gas and dust. Magnetic fields are understood to control this accreting matter, and dissipate excess angular momentum that would otherwise cause the star to break up as it forms (Bouvier 2013). Once accretion has stopped and the inner disc has been cleared of gas and dust, the star is classed as a weak-line T Tauri star (wTTS), so called because of a lack of accretion-driven H α emission in its spectra. Given that the distinct populations of wTTSs and cTTSs span a similar range of ages and internal structure development, magnetic field studies can be used to investigate intrinsic physical differences between the accreting cTTSs and non-accreting wTTSs, and determine the effect, if any, that accretion has on the large-scale magnetic fields of these stars.

The magnetic fields of a number of cTTSs have been studied in detail through the Magnetic Protostars and Planets (MaPP) project (e.g. Donati et al. 2007, 2008, 2010, 2011; Hussain et al. 2009; Donati et al. 2012). These show a range in the large-scale surface magnetic field topologies, which appears to correlate with internal structure evolution: fully convective cTTSs show predominantly dipolar and axisymmetric fields, whereas cTTSs that have evolved to form a radiative core demonstrate complex multipolar, non-axisymmetric fields (see Gregory et al. 2012 for a more detailed discussion).

In recent years, various wTTSs [V410 Tau (Skelly et al. 2010), LkCa 4 (Donati et al. 2014), V819 Tau (Donati et al. 2015), V830 Tau (Donati et al. 2015; Donati et al. 2016, 2017), TAP 26 (Yu et al. 2017), Par 1379 and Par 2244 (Hill et al. 2017)] have had their large-scale surface magnetic fields mapped, thanks to the Magnetic Topologies of Young Stars and the Survival of close-in giant Exoplanets (MaTYSSE) large programme, an international,

★ E-mail: belinda.annette.nicholson@gmail.com

© 2018 The Author(s)
Published by Oxford University Press on behalf of the Royal Astronomical Society

Downloaded from https://academic.oup.com/mnras/article-abstract/480/2/1754/5059584
by University of Southern Queensland user
on 23 August 2018

Table 1. Journal of observations for star TWA 9A. This table lists (1) the date of observation, (2) the Heliocentric Julian date, (3) the exposure time as a set of sub-exposures, (4) the stellar rotational phase based on a period of 5.01 d, with the zero-point set as the date of the first observation, (5) the peak SNRs in Stokes I per observation, (6) the peak SNR in Stokes V per observation, (7) the SNR after performing least-squares deconvolution (LSD, see Section 2.1) in Stokes I, and (8) the SNR after LSD in Stokes V.

Date (2014)	HJD (2456000+)	Exposure time (s)	Rotation phase	Stokes I obs. SNR	Stokes V obs. SNR	Stokes I LSD SNR	Stokes V LSD SNR
23 May	801.64194	4 × 1100	0.00	37	32	798	1731
25 May	803.59193	4 × 1100	0.39	56	58	1036	2873
26 May	804.58780	4 × 1100	0.59	60	56	1057	3190
27 May	805.58943	4 × 1100	0.79	41	37	1008	2894
30 May	808.59376	4 × 1700	1.39	82	73	1090	4225
31 May	809.51753	4 × 1700	1.57	93	83	1109	5161
1 June	810.53135	4 × 1700	1.77	92	84	1126	5178
2 June	811.52101	4 × 1700	1.97	116	103	1151	6670
3 June	812.58791	4 × 1700	2.18	49	45	856	2256
5 June	814.55552	4 × 1700	2.58	76	70	1067	4156
6 June	815.66190	4 × 1700	2.80	52	46	845	2454
7 June	816.55456	4 × 1700	2.98	76	66	1083	4075
8 June	817.54804	4 × 1700	3.17	76	71	1090	4239
9 June	818.54821	4 × 1700	3.37	83	75	1120	4732

multitelescope programme (CFHT, TBL, and ESO 3.6m) aimed at gathering spectropolarimetric observations of wTTSs. These studies have found an even larger range of magnetic topologies than was found in accreting stars; from predominantly dipolar, poloidal field in the case of V830 Tau, to a predominantly toroidal field configuration in the case of LkCa 4, implying that changing the accretion state may have an impact on surface field topology.

In addition to characterizing their surface features, the MaTYSSE programme also aims to search for close-in giant exoplanets around wTTSs, applying the surface brightness information from Doppler imaging (DI) to aid in reducing activity-induced jitter in the radial velocity curves. WTTSs are ideal targets for searching for young exoplanets, due to the lack of interference from accretion or obscuration by a disc, and their fast rotation rates making them suitable DI targets. With this jitter-reduction technique there have been two close-in, giant, exoplanets detected, one each around V830 Tau and TAP 26.

In this paper, we present an analysis of spectropolarimetric data for two wTTSs, TWA 9A and V1095 Sco. We reconstruct the surface brightness topologies of both TWA 9A and V1095 Sco, and for TWA 9A we reconstruct the surface large-scale magnetic field. We also present an analysis of radial velocity curves for both stars using one of the activity filtering techniques developed in previous MaTYSSE studies, and compare the effectiveness of different DI techniques on activity jitter reduction. TWA 9A and V1095 Sco are presented together as both of them were observed with the HARPS spectrograph, and provide an interesting contrast in rotation rates and evolutionary stages, while having similar spectral types, and can both be considered young solar analogues. TWA 9A is a well-characterized wTTS in the TW Hya association, with numerous existing observations from optical to X-ray wavelengths. V1095 Sco has also been the target of multiwavelength studies, but has not been characterized in much detail.

In Section 2, we detail the observations, and in Section 3 we determine the parameters and evolutionary statuses of our stars from the literature and our own calculations. Section 4 describes the process of creating the surface brightness and magnetic field maps, and we examine the H α emission in the spectra of both stars in Section 5. Section 6 presents analysis of the radial velocity curves of each star, and Section 7 explores the stellar rotation period measurements in our work. We summarize and discuss our findings in Section 8.

2 OBSERVATIONS

TWA 9A and V1095 Sco were both observed as part of the MaTYSSE programme using the HARPS spectropolarimeter on the 3.6m ESO Telescope at the La Silla Observatory in Chile. The journals of observations for TWA 9A and V1095 Sco are shown in Tables 1 and 2, respectively. A total of 14 observations were made of TWA 9A over 17 nights, and 13 observations of V1095 Sco over 13 nights, corresponding to approximately three rotations of TWA 9A, and over four rotations of V1095 Sco. Each observation was taken as a set of four sub-exposures in alternating configurations of the quarter-wave retarder to remove to first order any spurious polarization signals. The wavelength coverage of the spectra is from 383 to 691 nm with a spectral resolution of ∼115 000, and peak signal-to-noise ratios (SNRs) ranging between 36 and 116 for TWA 9A, and 60 and 100 for V1095 Sco.

The data were reduced using LIBRE-ESPRIT, a pipeline reduction tool designed for spectropolarimetric observations, with adaptations for use with HARPS polarimetric data (Hébrard et al. 2016), following the procedure outlined by Donati et al. (1997).

2.1 Least-squares deconvolution

To increase the SNR in our intensity and Stokes V line profiles, absorption lines are combined using LSD (Donati et al. 1997). This process involves de-convolving the observed stellar spectrum with an absorption line list, giving the profile of an average line (called an LSD profile) with an enhanced SNR compared to a single line profile in the original spectrum. In order to create this average profile, we first create a line list specifying the depths and Landé factors of selected photospheric lines based on the star's spectral type. For both stars, a list was generated using the VALD3 database (Ryabchikova et al. 2015), using the stars' respective effective temperatures ($T_{\rm eff}$) and log surface gravities ($\log g$) as inputs (determination of these quantities is detailed in Section 3.1). These lists were edited to remove lines that were contaminated by obvious emission features, strong stellar absorption features, and telluric absorption features,

Downloaded from https://academic.oup.com/mnras/article-abstract/480/2/1754/5059584
by University of Southern Queensland user
on 23 August 2018

Table 2. Table of observations for star V1095 Sco. For description, see caption of Table 1. A rotation period of 2.90 d was used for calculating the rotation phase.

Date (2014)	HJD (2456000+)	Exposure time (s)	Rotation phase	Stokes I obs. SNR	Stokes V obs. SNR	Stokes I LSD SNR	Stokes V LSD SNR
14 June	823.63745	4 × 1250	0.00	67	62	839	2310
15 June	824.65217	4 × 1250	0.35	61	56	846	2168
16 June	825.72489	4 × 1250	0.72	67	61	877	2393
17 June	826.68254	4 × 1900	1.05	85	76	914	3190
18 June	827.68058	4 × 1900	1.39	85	80	905	3166
19 June	828.71628	4 × 1900	1.75	87	78	935	3358
20 June	829.62037	4 × 1900	2.06	81	75	913	2910
21 June	830.59708	4 × 1900	2.40	64	38	846	1363
22 June	831.64483	4 × 1900	2.76	92	78	980	3129
23 June	832.59325	4 × 1900	3.09	98	91	967	3605
24 June	833.59082	4 × 1900	3.43	68	64	828	2397
25 June	834.62734	4 × 1900	3.79	63	59	838	2233
26 June	835.59555	4 × 1900	4.12	67	63	771	2386

or had a line depth relative to the deepest line of less than 0.1. For each star, the LSD line profiles were renormalized and scaled by the mean equivalent width of the set of LSD profiles. The resulting LSD profiles have a mean SNR in Stokes V (Stokes I) of 3845 (1031) for TWA 9A and 2662 (881) for V1095 Sco. The peak SNR in Stokes V for all observations for both stars is given in Tables 1 and 2.

3 EVOLUTIONARY STATES OF TWA 9A AND V1095 SCO

3.1 Spectral classification

Determining the spectral type of a PMS star is not straightforward, and appears be sensitive to the procedure used. This is exemplified by the range in spectral types and temperatures found in the literature and determined here for both stars. For TWA 9A, the literature values for spectral type range between K5 (e.g. Manara et al. 2013) and K7 (e.g. Pecaut & Mamajek 2013), cooler than the K4 we determine here. Manara et al. determine the spectral types from the relative depths of several molecular bands using low-resolution, visible spectra in the range 580–900nm. Pecaut and Mamajek use low-resolution spectra in a narrower range of wavelengths (560–690nm), and compare several atomic lines, blends, and molecular bands to a set of PMS spectral standards. For cooler stars, the inclusion of cooler molecular bands and blends for spectral typing leads to a cooler temperature, as these features will be present in the spots on the surface, skewing the photospheric temperature. The exception to this is the use of TiO molecular bands, which Herczeg & Hillenbrand (2014) find to be poorly modelled for PMS stars, giving a hotter spectral type compared to when they are excluded. This potentially explains the difference in spectral types between Manara et al. who include TiO and Pecaut and Mamajek who do not.

Given the uncertainty in the literature, we re-determine the $T_{\rm eff}$ and $\log g$ of both stars using the spectral typing procedure outlined in Donati et al. (2012), which follows the method of Valenti & Fischer (2005) of comparing high-resolution optical spectra to a grid of synthetic spectra generated for a range of $T_{\rm eff}$ and $\log(g)$ values. For TWA 9A, we find a $T_{\rm eff}$ of 4400 ± 50 K and $\log g$ of 4.1 ± 0.2. Using the conversion table of Herczeg & Hillenbrand (2014), this corresponds to a spectral type around K4. This spectral typing procedure uses only atomic lines that are less sensitive down to spot temperatures.

For V1095 Sco, we find a$T_{\rm eff}$ of 4350 ± 50 K and $\log g$ of 3.8 ± 0.2, which also corresponds to a spectral type of K4. Krautter et al. (1997) found a spectral type of K5 using low-resolution spectra, and comparing with MS spectral standards from the MK star catalogue (Buscombe 1981, 1988). Gregory, Adams & Davies (2016) find that, at a given temperature, the use of MS spectral standards gives a systematically cooler spectral type for mid-G to mid-K stars. This may explain the slightly cooler spectral type found by Krautter et al. compared with our determined spectral type.

3.2 Determination of stellar parameters and inclination

In order to determine the most accurate surface maps, we must first determine the inclination of our stars with respect to the observer. This is evaluated based on rotation period, $v \sin i$ and radius of the star. The radius, along with mass and age, is determined from PMS stellar evolution tracks, in this case the models of Baraffe et al. (2015), using $T_{\rm eff}$ (see Section 3.1) and luminosity.

There are a variety of values of luminosity for TWA 9A in the literature, ranging from $0.13\,{\rm L}_{\odot}$ (McDonald, Zijlstra & Boyer 2012) up to $0.34\,{\rm L}_{\odot}$ (Pecaut & Mamajek 2013). The variation in these values can be at least partly accounted for by differences in the distance used. McDonald et al. use the *Hipparcos*-derived parallax distance of 46 pc for their luminosity calculation. Pecaut & Mamajek redetermine their own distance (70.0 ± 3.8 pc) using the kinematic parameters from Weinberger, Anglada-Escudé & Boss (2013), and the method described in Mamajek (2005). Manara et al. (2013) use the distance of ∼68 pc from Mamajek (2005), but assume a different apparent magnitude, and so find a lower luminosity of $0.25\ {\rm L}_{\odot}$. All luminosity calculations mentioned in the literature take the interstellar extinction, A_v, to be zero. This likely results from using low-resolution spectra to determine extinction, which can lead to zero, or negative extinction values, as in the case of Herczeg & Hillenbrand (2014). We re-determine the luminosity using the parallax measurement from *Gaia* Data Release 2 (DR2; Gaia Collaboration et al. 2016, 2018), which gives a distance of 76.4 ± 0.3 pc. We calculate extinction, A_v using apparent V-band magnitude, $m_V = 11.143 \pm 0.029$ mag, from Henden et al. (2016), V-band bolometric correction ${\rm BC}_V = -0.77 \pm 0.18$ and intrinsic colour $(B-V)_0 = 1.1 \pm 0.09$ from from Pecaut & Mamajek (2013), and observed colour $(B-V) = 1.244 \pm 0.067$ from Henden et al., giving $A_v = 0.42 \pm 0.35$ mag. This gives a luminosity of $0.48 \pm 0.09\ {\rm L}_{\odot}$. This luminosity is higher than any listed in

Downloaded from https://academic.oup.com/mnras/article-abstract/480/2/1754/5059584
by University of Southern Queensland user
on 23 August 2018

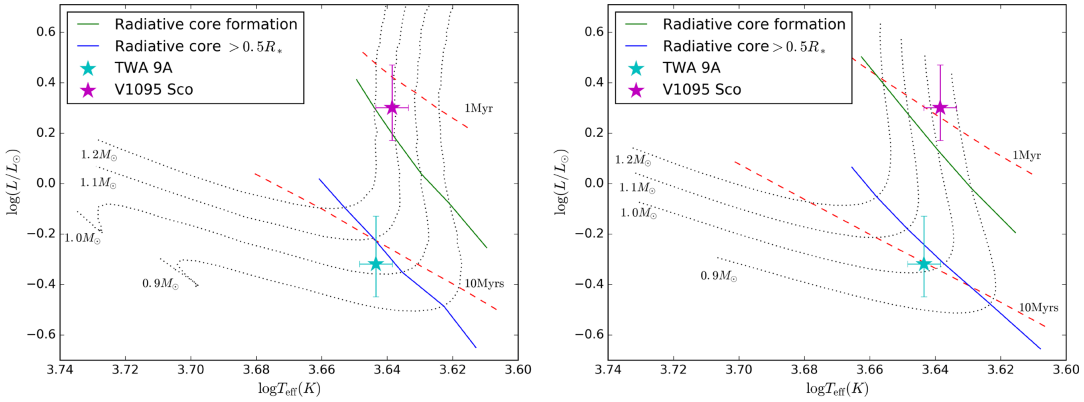

Figure 1. HR diagrams showing the locations, including 1σ uncertainties, of TWA 9A (cyan) and V1095 Sco (magenta) with relation to the Baraffe et al. (2015) (right), and Siess et al. (2000) (left) PMS evolutionary models. In both figures, the black dotted lines are evolutionary tracks for 0.9 $M_\odot$, 1.0 $M_\odot$, 1.1 $M_\odot$, and 1.2 $M_\odot$, and the red dashed lines are isochrones for 1 and 10 Myr. The green line indicates the boundary between full convection and the formation of a radiative core, and the blue line indicated the point at where the radiative core becomes larger than $0.5R_*$.

the literature. This higher luminosity is expected given our larger distance, and high value of A_v, which could be due to reddening from the presence of photospheric spots, rather than interstellar dust.

The literature values for the luminosity of V1095 Sco vary widely from 0.74 $L_\odot$ (Sartori, Lépine & Dias 2003) to 3.45 $L_\odot$ (Wahhaj et al. 2010). These differences can also be attributed to differences in distance and extinction corrections used. Since the distance to V1095 Sco had not been measured at the time, both authors use the distance to the Lupus star forming region. Sartori et al. takes this distance to be 147 pc from Bertout, Robichon & Arenou (1999), whereas Wahhaj et al. use 200 pc from Comerón (2008). Both authors differ in their choice of extinction, with Sartori et al. using $A_v = 0.0$, and Wahhaj et al. finding $A_v = 0.7$. These stark differences in extinction and distance values, as well as subtle differences in values of apparent magnitude, account for the large differences in luminosity. We recalculate the luminosity for V1095 Sco using the parallax measurement from *Gaia* DR2, which give a distance of 162 ± 1 pc. We take the observed colour $(B - V) = 1.309 \pm 0.045$ and apparent magnitude $V = 11.424 \pm 0.041$ from Henden et al. (2016), and intrinsic colour $(B - V)_0 = 1.11 \pm 0.09$ and bolometric correction BC $= -0.77 \pm 0.18$ from Pecaut & Mamajek (2013) and calculate an extinction $A_v = 0.62 \pm 0.31$, giving a luminosity of 2.0 ± 0.3 $L_\odot$. A higher estimate of A_v compared to TWA 9A is expected given the greater distance to this star, and is likely affected by both interstellar dust and reddening due to spots.

Fig. 1 shows the locations of TWA 9A and V1095 Sco on the HR diagram with respect to the PMS evolutionary models of Baraffe et al. (2015) (left), and, for comparison with other MaTYSSE stars, the models of Siess, Dufour & Forestini (2000) (right). Our mass, radius, and age estimates for our stars are based on the models of Baraffe et al. (2015), and are shown in Table 3. These models largely agree for stars on the Henyey track, as is the case of TWA 9A, but there are discrepancies for those on the Hayashi track, with a difference in mass estimate of $\sim$0.1 $M_\odot$ for V1095 Sco. However, this difference is within the 3σ uncertainty in temperature for V1095 Sco. Examining the proximity of these stars on the HR diagram with respect to the point of radiative core formation (green line), and the formation of a substantial radiative core ($>0.5R_*$, blue line), both models indicate that V1095 Sco is still fully convective, but close to forming a radiative core. TWA 9A, however, is estimated to have already formed a substantial radiative core ($0.60 \pm 0.06R_*$), and is more evolved than V1095 Sco.

Table 3. Summary of the properties of TWA 9A and V1095 Sco. Uncertainties are given where available.

	TWA 9A	V1095 Sco.
Mass, M_* ($M_\odot$)	1.00 ± 0.1	$0.96^{+0.05}_{-0.08}$
$R\sin i$, ($R_\odot$)	1.070 ± 0.003	1.75 ± 0.03
Radius, R_* ($R_\odot$)	$1.2^{+0.3}_{-0.2}$	$2.5^{+0.4}_{-0.5}$
Age (Myrs)	10^{+13}_{-5}	$0.9^{+1.1}_{-0.4}$
Luminosity, L_* ($L_\odot$)	0.5 ± 0.2	2.0 ± 0.7
Distance, (pc)	76.4 ± 0.3	162 ± 1
Extinction, A_v (mag)	0.42 ± 0.35	0.62 ± 0.32
$v\sin i$ (km s^{-1})	10.8 ± 0.02	30.6 ± 0.1
Rotation period, $P_{\rm rot}$ (d)	5.01 ± 0.01	2.9 ± 0.05
Effective temperature, $T_{\rm eff}$ (K)	4400 ± 50	4350 ± 50
Surface gravity, log (g)	4.1 ± 0.2	3.8 ± 0.2
Spectral type	K4	K4
Inclination angle, i (Degrees)	$\sim$65	$\sim$45

We calculate the inclination of each star with respect to the observer[1] from the radii, $v\sin i$'s and rotation periods given in Table 3. For V1095 Sco, we estimate an inclination of $\sim$45°, slightly higher than the inclination of $\sim$40° that results from the luminosity value of 3.45 $L_\odot$ from Wahhaj et al. For TWA 9A, we find an inclination of $\sim$65°. It is interesting to note that none of the literature luminosity values for TWA 9A result in a radius that gives a viable $\sin(i)$ value (i.e. $\sin(i) < 1$), supporting our larger luminosity determination.

[1]In this convention, $i = 0°$ means a pole-on view, and $i = 90°$ means an equator-on view.

Downloaded from https://academic.oup.com/mnras/article-abstract/480/2/1754/5059584
by University of Southern Queensland user
on 23 August 2018

4 TOMOGRAPHIC MODELLING

4.1 Brightness mapping

Using the stellar parameters described in Section 3 and our Stokes I LSD profiles (Section 2), we reconstruct surface brightness maps of TWA 9A and V1095 Sco using the technique of DI. For this, we use an updated version of the code DOTS (Collier Cameron 1997), which now reconstructs surface brightness, as described by Donati et al. (2014), allowing for both dark and bright regions, rather than spot filling alone. We estimate the local line profile assuming a Milne–Eddington model atmosphere, invert the profiles and use a maximum entropy regularization to reconstruct an image of surface brightness that requires the least amount of information to fit the observed data to a given level described by the reduced chi-squared, χ^2_r.

In the process of reconstructing the brightness map, we optimize for the mean radial velocity$v_{\rm rad}$, local line equivalent width (EW), $v\sin i$, and rotation period, $P_{\rm rot}$, for each star; the latter two of these parameters are given in Table 3. The fits to the intensity profiles are shown by the red lines in Figs 2 and 3.

The surface brightness maps of TWA 9A and V1095 Sco are shown in Figs 4 and 5, respectively. These plots are rectangular projections of the stellar surface in longitude and latitude.

Our reconstructions show both dark and bright spotted regions. TWA 9A shows a complex surface brightness map, with strong signatures of both spots and plage. The spots are located near the equator and mid-latitudes, whereas the bright plage is found at a higher latitude.

The surface brightness map of V1095 Sco is simpler, with one large polar spot, and three areas of plage at mid-latitudes. Inspection of the intensity profiles of V1095 Sco shows characteristic flat-bottomed profiles indicating the need for a dark polar spot in the resulting maps. The fact that the plage is preferentially associated with gaps in the phase coverage indicates that it could be spurious, though a better fit is achieved with the inclusion of plage than with spots alone.

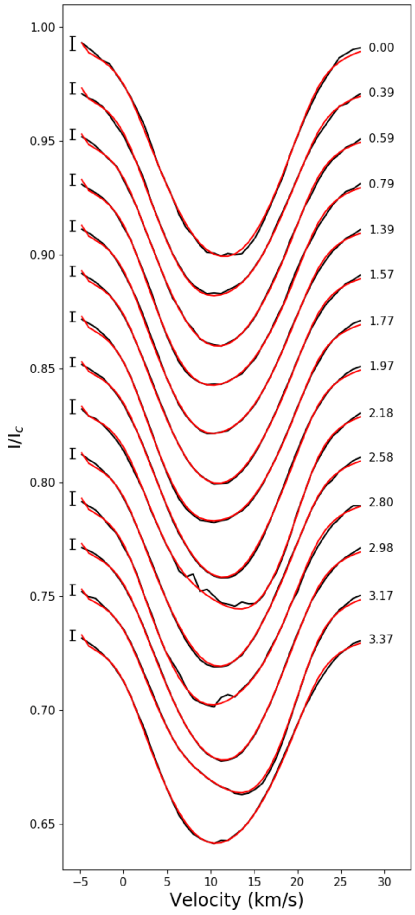

Figure 2. These plots show the Stokes I LSD profiles for TWA 9A (black), and the best-fitting synthetic line profile (red). The phases of observation are given to the right of each line, with the zero phase set as the first observation and our derived stellar rotation period $P_{\rm rot} = 5.01$ d. The error bar on the left is the mean 3σ error for each Stokes I profile.

4.2 Magnetic mapping

By inverting the Stokes V profiles, we can also reconstruct the large-scale magnetic fields of TWA 9A. Our reconstructions are shown in Fig. 6, with the fits to the Stokes V profiles of TWA 9A shown in Fig. 7. For this analysis, we used the ZDIPY code of Folsom et al. (2018). This is based on the Zeeman–Doppler imaging (ZDI) method of Semel (1989), Donati et al. (1997), and Donati et al. (2006), representing the field components as spherical harmonics and using the maximum entropy regularization of Skilling & Bryan (1984) to solve for the best-fittinf configuration. Its performance has been calibrated against the published code of Donati et al. (2006). We used the same stellar parameters determined from our analysis of the intensity profiles (see Table 3), and take into account the surface brightness variations in our reconstruction of the magnetic field. The Stokes I local line profile parameters are comparable to that used in the DOTS code. The Stokes V profile were modelled using the weak field approximation with mean Landé factor and central wavelength corresponding to those used to extract the LSD profiles and for the brightness reconstruction. The optimum value of χ^2_r aim was chosen using the method of Alvarado-Gómez et al. (2015), who choose the optimum target χ^2_r using the maxima in the second derivative of entropy as a function of χ^2_r in a set of converged magnetic field solutions. According to our analysis, this implies the map obtained fitting the data at a χ^2_r of 2.0. This solution gives a mean magnetic field of 113 G, with a maximum of 296 G. Analysing the amount of energy in different spherical harmonic components of this magnetic field solution, we find a non-axisymmetric (57 per cent energy in non-axisymmetric components), predominantly poloidal large-scale field (∼69 per cent poloidal, ∼31 per cent toroidal). In the poloidal component, the field is predominantly dipolar and quadrupolar, with only ∼11 per cent in octopolar or higher orders. The dipolar component of the field has a maximum intensity of 127 G, and is tilted at an angle of 36.5 deg to the rotation axis, with the pole located at phase 0.26. For comparison, we calculate the magnetic field configuration using zDoTS (Hussain et al. 2000, 2016) with the same local line profiles used for our brightness mapping. The best-fitting model also yields a predominantly non-axisymmetric field (55 per cent in non-axisymmetric components), and a predominantly poloidal field (∼64 per cent poloidal, ∼37 per cent toroidal). The poloidal field in this estimate is slightly more concentrated in the dipolar and quadrupolar components, with

Downloaded from https://academic.oup.com/mnras/article-abstract/480/2/1754/5059584
by University of Southern Queensland user
on 23 August 2018

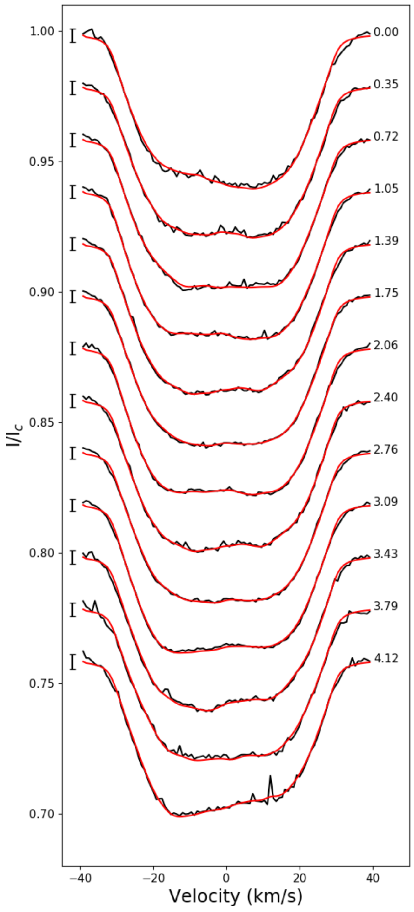

Figure 3. These plots show the Stokes I LSD profiles for V1095 Sco (black), and the best-fitting synthetic line profile (red). The phases of observation are given to the right of each line, with the zero phase set as the first observation and our derived stellar rotation period $P_{\rm rot} = 2.90$ d. The error bar on the left is the mean 3σ error for each Stokes I profile.

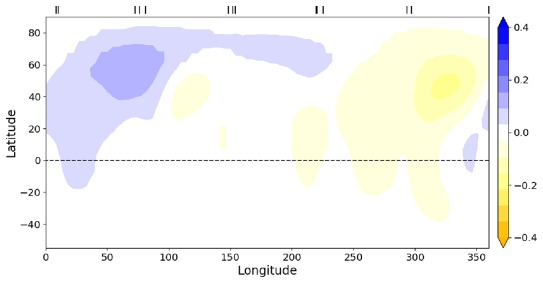

Figure 4. Surface brightness map of TWA 9A, shown as a rectangular projection of longitude and latitude. The colour scale indicates log surface brightness relative to a photosphere (0.0), with blue indicating the presence of plage, and yellow the presence of spots. The observations are marked by black ticks across the top, and black dashed line indicates the equator.

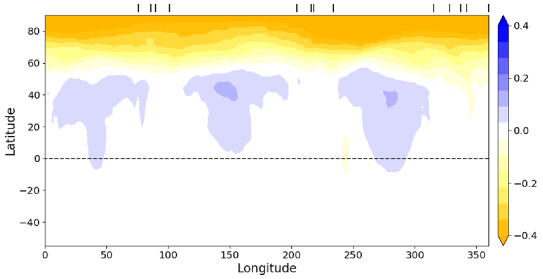

Figure 5. Surface brightness map of V1095 Sco, shown as a rectangular projection of longitude and latitude. Plot description same as for Fig. 4.

8.5 per cent of the poloidal field energy being containing in octopolar components or higher.

Magnetic mapping using the Stokes V LSD line profiles of V1095 Sco was attempted, but a reliable solution could not be found due to the poor SNR of the observations. The Stokes V spectra of observation for which there are marginal (false alarm probability between 10^{-5} and 10^{-3}) or definite (false alarm probability less than 10^{-5}) signal detections are plotted in Fig. 8. Comparing the Stokes V LSD profiles to the null for these observations suggests that the signal in some of these marginal detections is spurious. The phase coverage in the remaining robustly detected signatures was insufficient to yield a reliable surface magnetic field map.

4.3 Surface differential rotation

The surface differential rotation of both stars was determined through the process of reconstructing the surface brightness map and, for TWA 9A, also using our large-scale magnetic field maps. Here, we define differential rotation as:

$$\Omega(\theta) = \Omega_{\rm eq} - {\rm d}\Omega \sin^2(\theta), \quad (1)$$

where $\Omega(\theta)$ is the stellar rotation at latitude θ, $\Omega_{\rm eq}$ is the equatorial angular velocity, and dΩ is the difference in rotation, or shear, between the equator and the pole. To determine the differential rotation from surface brightness, we compute a grid of models, varying Ω and dΩ, and fit for the minimum in the resulting χ^2_r surface with a fourth order paraboloid. The 3σ error is determined by the 3σ contour of the paraboloid.

Performing this analysis on the intensity profiles of V1095 Sco, we find no clear differential rotation solution. For TWA 9A, however, we find minima for both our brightness and magnetic field reconstructions. These are plotted in Fig. 9, where each panel shows the χ^2_r surface as a function of Ω and dΩ. The left-hand panel shows the χ^2_r surface from ZDI, the right-hand panel shows the χ^2_r surface from DI, and the centre panel shows the paraboloid fits and minima for both the DI (blue lines and plus) and ZDI (green lines and plus) maps. The DI map gives a solution of $\Omega_{\rm eq} = 1.273 \pm 0.007$ rad d^{-1}, and d$\Omega = 0.05 \pm 0.02$ rad d^{-1}, meaning the equator will lap the pole once every 125.7 d. The ZDI map, however, gives a shear solution of $\Omega_{\rm eq} = 1.254 \pm 0.008$ and d$\Omega = -0.013 \pm 0.013$, which could indicate antisolar shear. Given the greater relative uncertainty on this value, we examine the overlapping region of our DI and ZDI 3σ elipses and take d$\Omega = 0$ for our ZDI analysis.

Downloaded from https://academic.oup.com/mnras/article-abstract/480/2/1754/5059584
by University of Southern Queensland user
on 23 August 2018

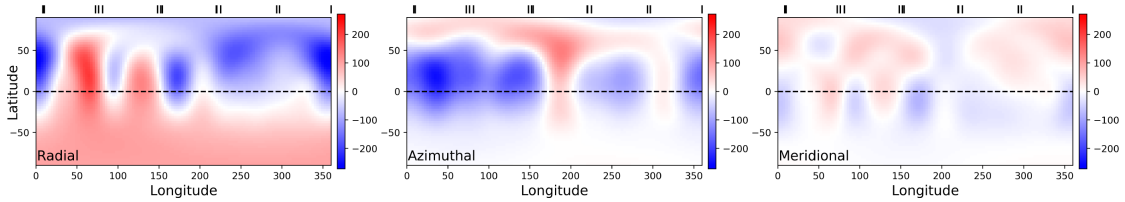

Figure 6. Maps of the radial, azimuthal, and meridional magnetic field components for TWA 9A. Colour scale is magnetic field strength in Gauss, the dashed line indicates the equator, and tick marks across the top indicate observed longitudes.

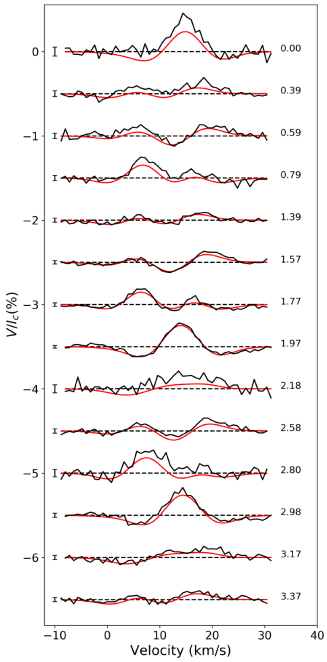

Figure 7. Stokes V intensity, expressed as a percentage of Stokes I continuum of TWA 9A (shown in Fig. 2). The black line is the observed data, and the red line the fit to the data with ZDI. Error bars on the left indicate the mean 1σ error for the observation, and the number on the right indicates the rotation phase of the observation based on 5.01 d rotation period.

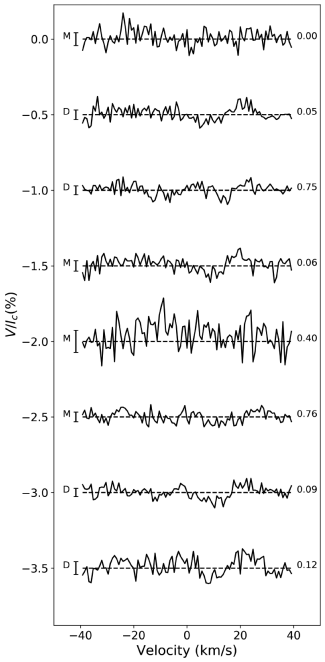

Figure 8. Stokes V intensity data for V1095 Sco, expressed as a percentage of Stokes I continuum. The letter on the right of reach spectrum indicated the level of magnetic field detection: 'M' for marginal detection (false alarm probability between 10^{-5} and 10^{-3}) and 'D' for a definite detection (false alarm probability less than 10^{-5}). Spectra for which there is no detection in stokes V are not shown. Error bars on the left are the mean 1σ errors for each observation, and the numbers on the right indicate the phase of observation, based on a rotation period of 2.9 d.

4.4 Longitudinal magnetic field

We also measure the line of sight, or longitudinal, magnetic field, B_l, for each Stokes V profile following Grunhut et al. (2013), using the mean Landé factor and central wavelength of our LSD profiles. To determine the amount of spurious signal in these measurements, the same calculation is performed for each null spectrum, denoted N_l here. For TWA 9A, these values are plotted in Fig. 10. The B_l values vary between -68.3 ± 6.9 G and 32.6 ± 5.5 G. Only two N_l values show spurious signal, although the associated B_l values are still consistent with the rest of the sample. The clustering of B_l values at the same rotation phase indicate minimal changes to the large-scale field over the period of observations. A generalized Lomb-Scargle period analysis of these values give a dominant period aligning with the stellar rotation period (see Section 7 for more details).

For V1095 Sco, we calculate the longitudinal field for each marginal or definite detection Stokes V profiles. These are not reliable, however, due to the high level of noise present, and these B_l values are mostly the same order as the null measurement. The observation of V1095 Sco with the strongest signal the least noise gives a longitudinal field of 25.9 ± 16.0 G.

5 TEMPORAL VARIABILITY OF CHROMOSPHERIC EMISSION

Both stars in our sample are magnetically active, and therefore have strong chromospheric emission in, for example, the Balmer lines. We explore this by examining the H α (λ656.285 nm) region of the

Downloaded from https://academic.oup.com/mnras/article-abstract/480/2/1754/5059584
by University of Southern Queensland user
on 23 August 2018

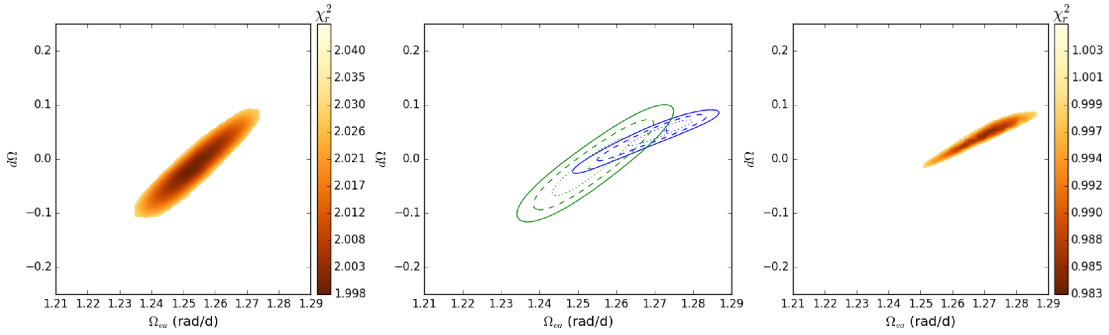

Figure 9. Differential rotation measurements of TWA 9A from modelling of Stokes V (left) and Stokes I (right). Left: Variations in χ^2_r as a function of equatorial rotation, Ω_{eq}, and shear, dΩ from circular polarisation profiles. Right: Variations in χ^2_r as a function of Ω_{eq} and dΩ from intensity profiles. Centre: Paraboloid fits to the χ^2_r surface from Stokes I (blue) and Stokes V (green). The central plus indicates the best-fitting values, the dashed line the 1σ contour from the paraboloid fit, and the solid line the 3σ contour.

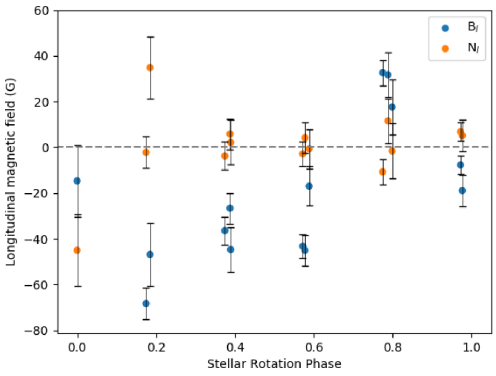

Figure 10. Longitudinal magnetic field for TWA 9A, calculated for each Stokes V profiles (B_l, blue circles), and in the null profiles (N_l, orange circles), with 1σ uncertainties.

stellar spectra to probe rotational modulation, and look for changes in activity over our period of observation.

For TWA 9A, we find strong, double-peaked emission across all observations, with enhanced emission during the observations on 2014 June 3 (rotation phase 2.18). A plot of the stacked H α spectra for these observations is shown in Fig. 11. We see variation in the strength of the emission with stellar rotation, but minimal variation in the shape of the line, indicating the variation is likely due to areas of different activity level on the stellar surface. This emission is narrow and weak enough to fall below the accretion cut-off for a cTTS as defined by Cieza et al. (2013), and therefore the emission is interpreted as chromospheric in nature.

For the epoch with significantly enhanced H α emission (2014 June 3), we also examine the H β, He I and Na I doublet regions of the spectrum, and compare these regions to those taken one rotation later (phase 3.17), and to the mean spectrum. This is shown in Fig. 13. Each of these regions exhibit different behaviour in the June 3 epoch, compared with that phase observed one rotation later and the mean spectrum. Both the He I and Balmer lines show enhanced emission, and the Na doublet shows emission in the cores of the lines that is absent from the other observations. These changes in the spectral features, and the short time-scales of the changes,

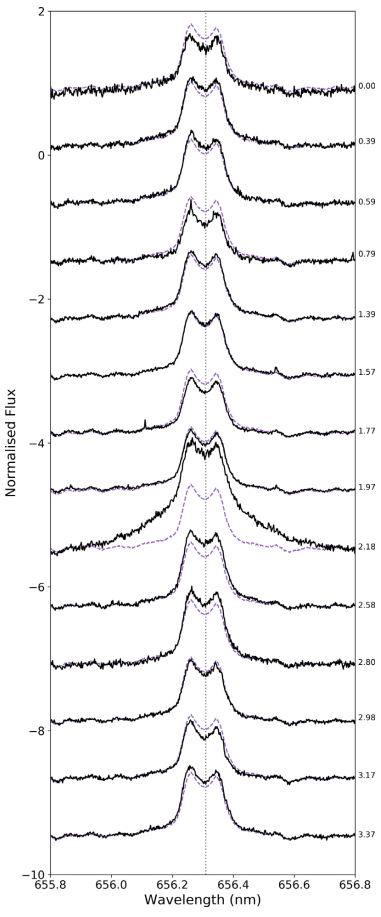

Figure 11. Stacked H α emission spectra for TWA 9A (black), plotted over the mean spectrum (purple, dashed), with the spectrum of the suspected flare excluded from the mean. Numbers on the right-hand side indicate the phase of observation. The grey dotted line indicated the centre of the H α line given the star's radial velocity.

Downloaded from https://academic.oup.com/mnras/article-abstract/480/2/1754/5059584
by University of Southern Queensland user
on 23 August 2018

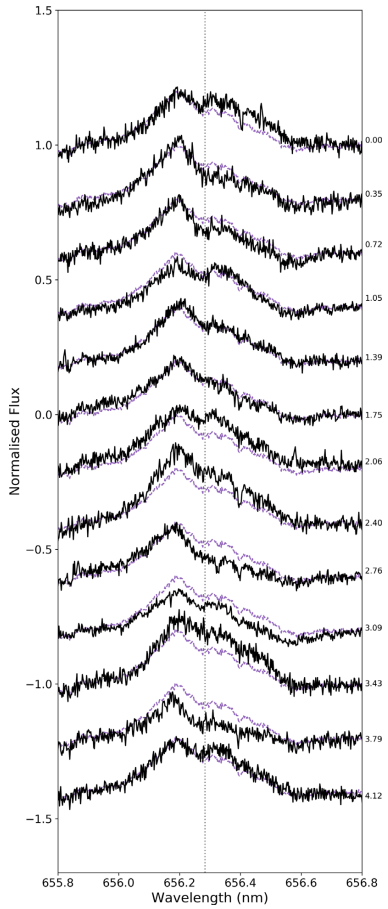

Figure 12. Stacked H α emission spectra for V1095 Sco (black), plotted over the mean spectrum (purple, dashed). Description as per Fig. 11.

suggest that this enhanced emisssion is most likely caused by a flare.

Examining the Stokes I and V LSD profiles for that observation, we find no significant difference between that profile and the Stokes I and V profiles at same phase observed post-flare, so can conclude that this has had negligible influence on our tomographic modelling and radial velocity analysis. This is expected, as regions containing emission lines or strong absorption features, such as Na I, are excluded from our line list for the LSD.

For V1095 Sco, a plot of the stacked H α spectra is shown in Fig. 12. Overall, the emission is weaker than in TWA 9A. We see enhanced emission on the blue-ward side of the profile (possibly indicating mass motion towards the observer) in a region around phase 0.4 and again in a region around phase 0.75, but more symmetric emission at phase 0.0–0.1.

We calculate an H α index for both stars as defined in equation (9) of Marsden et al. (2014), with a standard rectangular bandpass of 0.36 nm over the emission region, and two continuum bandpasses of 0.22 nm centred on 655.885 and 656.730 nm. These measurements are shown for both stars in Fig. 14, along with 3σ uncertainties. For V1095 Sco, whilst there does appear to be cyclical behaviour in the H α index, there also appears to be evolution over the period of observations, with an increase in the range of values in the later observations. For TWA 9A, the flare event is evident in the H α indices, with a significantly higher index for that observation compared to the rest, which seems to vary cyclically with stellar rotation (see Section 7 for period analysis). It should be noted that due to the breadth of the emission in the flare spectrum, the standard bandpass is saturated, and the standard continuum regions chosen fall within the emission region for that observation, so that index value is likely underestimated.

6 RADIAL VELOCITIES AND ACTIVITY JITTER

The process of reconstructing the brightness maps allows us to characterize and filter out the activity-induced jitter from the observed radial velocities (see e.g. Donati et al. 2015). Our radial velocities are calculated as the first order moment of the Stokes I profile (i.e. $1 - I$) as a function of velocity in the heliocentric rest frame. The radial velocity contribution of the stellar surface features is calculated as the radial velocity of our DI fits to the Stokes I LSD profiles. We then filter the activity jitter from the observed radial velocities by subtracting off the radial velocity values of these fits. The uncertainties for both the filtered and unfiltered radial velocities are calculated using the method of Butler et al. (1996).

Analysis of the radial velocities of TWA 9A is shown in Fig. 15. The RMS of the unfiltered radial velocities is 187 m s^{-1}, and the activity filtered radial velocities have an RMS of 25 m s^{-1}, with the 1σ uncertainties averaging 20 m s^{-1}. Since the dispersion of our radial velocities is smaller than the 3σ uncertainty across all RV measurements, we are unable to detect any significant signal in the data (see Section 7 for further period analysis). Additionally, this technique is insensitive to planets with periods equal to, or harmonics of, the stellar rotation period. With our current detection limits and RV measurements, we can rule out the presence of a planet with an $M_p \sin i$ greater than $\sim$0.4 Jupiter masses and closer than $\sim$0.1 au, assuming a circular orbit.

The same radial velocity analysis was performed for the radial velocities of V1095 Sco, shown in Fig. 16. The RMS of the unfiltered radial velocities is 137 m s^{-1}, and 1σ uncertainties averaging 39 m s^{-1}. Applying the same filtering technique, we obtain an RMS of 47 m s^{-1}. Since the dispersion is smaller than the 3σ uncertainties, we are again unable to detect any significant signal in the data (see Section 7 for further period analysis), but can rule out the presence of a planet with an $M_p \sin i$ greater than $\sim$1.0 Jupiter masses closer than $\sim$0.1 au, assuming a circular orbit.

To explore the difference in using plage and spot DI versus the spot-only version, we calculate the filtered radial velocities for TWA 9A and V1095 Sco using a spot-only model. For TWA 9A, the difference in the dispersion of the filtered radial velocities between the two models was insignificant ($<$ 1 per cent). For V1095 Sco, the dispersion of the plage and spot model filtered radial velocities was $\sim$9 per cent smaller than the dispersion of the spot-only model filtered radial velocities.

7 PERIODOGRAMS OF ACTIVITY JITTER AND PROXIES

There are a number of methods to search for rotational modulation in the multiple sets of diagnostics contained within our data sets to verify the rotation period determined from tomographic mapping. For both stars, we examine the periodic nature of the H α emission

Downloaded from https://academic.oup.com/mnras/article-abstract/480/2/1754/5059584
by University of Southern Queensland user
on 23 August 2018

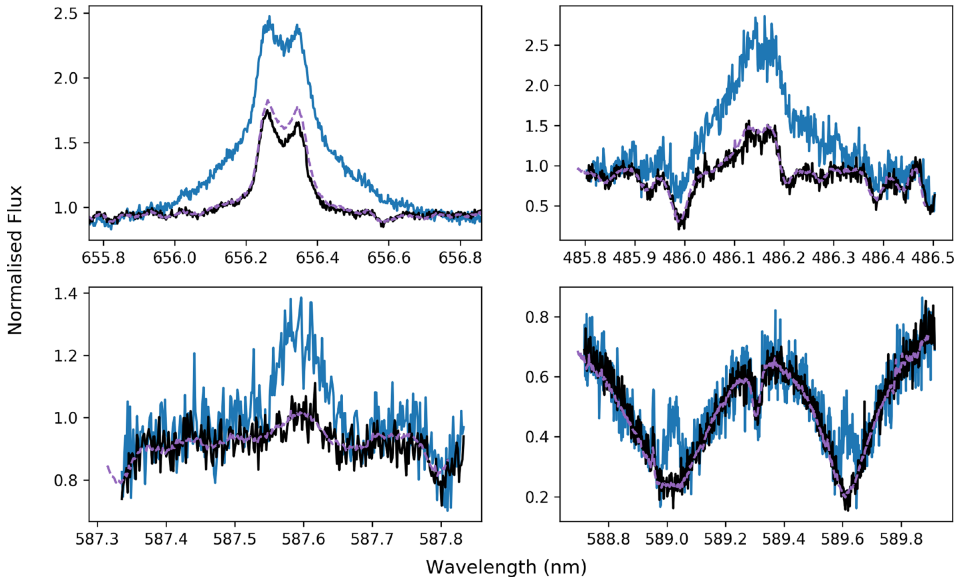

Figure 13. Emission in H α (top left), H β (top right), HeI (bottom left) and Na doublet (bottom right) of TWA 9A in the observation ascribed to a flare (blue), in an observation obtained one rotation later (black), and in the mean of the observed spectra (purple, dashed).

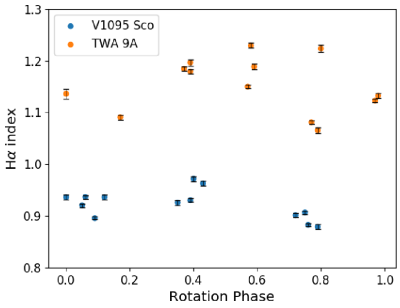

Figure 14. H α indices for V1095 Sco (blue) and TWA 9A (orange). Note that due to the large emission in the flare event of TWA 9A, that peak value of the H α index is underestimated due to saturation of the bandpass.

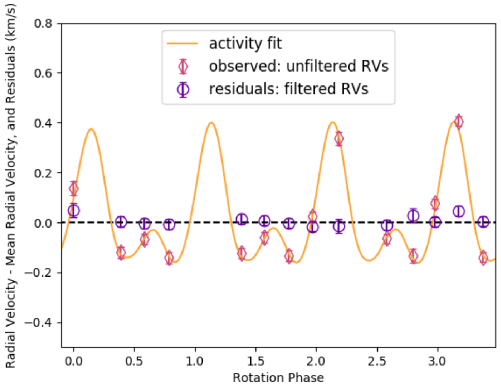

Figure 15. Radial velocity analysis of TWA 9A. The pink diamonds are the measured radial velocities from the observed intensity profiles (RMS 187 m s^{-1}), the orange line is the modelled radial velocity contribution of the activity measurement from the surface brightness reconstruction, and the purple circles are the residuals after subtracting the observation radial velocities from the activity fit radial velocities (RMS 25 m s^{-1}).

(Section 5), radial velocities, both unfiltered and filtered (Section 6), and for TWA 9A the B_l values (Section 4.4). For TWA 9A, we exclude the possible flare event from the H α index data set for our period analysis. We perform a period analysis with a generalized Lomb–Scargle periodogram (Zechmeister & Kürster 2009), using the PyAstronomy[2] package. The periodograms for TWA 9A are shown in Fig. 17, including false alarm probability (FAP) thresholds of 0.1 and 0.01. The FAP values are calculated as per equation (24) of Zechmeister & Kürster (2009). In each of the H α , B_l and unfiltered radial velocities, there is a peak in the power around our DI-determined stellar rotation period. The signal is clearest in the longitudinal field measurements compared to the H α indices whose peak is shifted to slightly longer periods, likely due to this diagnostic probing activity at higher altitudes. The stellar rotation period is absent from the filtered radial velocities, indicating that the jitter filtering process is effective at removing the first-order stellar rotation signal.

The periodogram for V1095 Sco is shown in Fig. 18. The periodicity in the unfiltered and filtered radial velocities is less clear than in the case of TWA 9A, likely resulting from the larger uncertainties in the radial velocity measurements and the poorer sampling, with the periods with the highest peaks being below our sample rate of $\sim$1 d^{-1}. As such, this diagnostic cannot be used to determine the

[2]https://github.com/sczesla/PyAstronomy

Downloaded from https://academic.oup.com/mnras/article-abstract/480/2/1754/5059584
by University of Southern Queensland user
on 23 August 2018

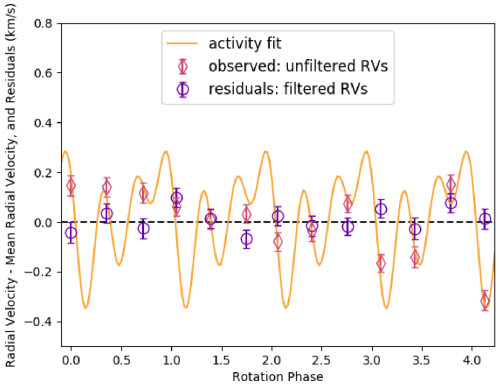

Figure 16. Radial velocity analysis of V1095 Sco. The pink diamonds are the measured radial velocities from the observed intensity profiles (RMS 137 m s^{-1}), the orange line is the modelled radial velocity contribution of the activity measurement from the surface brightness reconstruction, and the purple circles are the residuals after subtracting the observation radial velocities from the activity fit radial velocities (RMS 47 m s^{-1}).

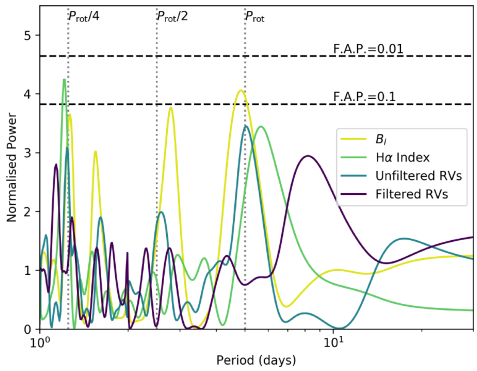

Figure 17. Generalized Lomb–Scargle periodogram for TWA 9A of B_l (yellow), H α (green), unfiltered radial velocities (blue), and filtered radial velocities (purple). Dashed black lines indicate the FAP thresholds, and grey dotted lines indicate the 1, 1/2, and 1/4 multiples of the rotation period.

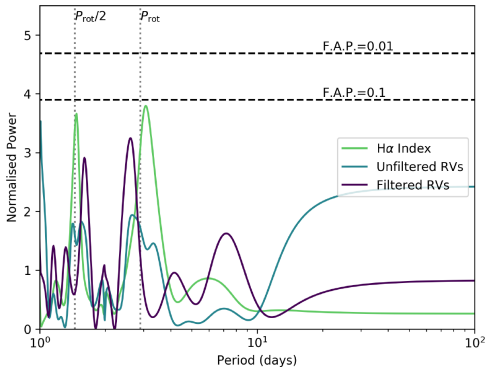

Figure 18. Generalized Lomb–Scargle periodogram for V1095 Sco of H α (green), unfiltered radial velocities (blue), and filtered radial velocities (purple). Dashed black lines indicate the FAP thresholds, and grey dotted lines indicate the 1 and 1/2 multiples of the rotation period.

effectiveness of our radial velocity filtering for this star. Nevertheless, the H α indices do show a peak of highest power around the DI determined rotation period, supporting our DI rotation period measurement for V1095 Sco.

8 SUMMARY AND DISCUSSION

This paper presents the results of spectropolarimetric observations of two wTTSs, TWA 9A and V1095 Sco, as part of the MaTYSSE Large Programme. These stars are studied as a pair as they represent two stages, pre- and post-radiative core formation, in 1 $M_\odot$ wTTS evolution. Observations for TWA 9A spanned 18 d, and for V1095 Sco spanned 13 d, and were obtained using the HARPS spectrograph on the ESO 3.6m Telescope at La Silla Observatory, Chile. The techniques of DI and ZDI were applied to both data sets to reconstruct the large-scale surface brightness and magnetic field features. From the surface activity information from the DI, we were able to filter the activity jitter from the radial velocities of both stars. This enabled radial velocity measurements that rule out the presence of close-in giant planets around these stars. We also examined the strongest of the Balmer emission lines, H α , as a source of information on the variability of chromospheric activity. We performed a period analysis on the H α activity index in combination with radial velocities (and longitudinal field in the case of TWA 9A) to verify the DI-determined rotation period, and demonstrate the effectiveness of the radial velocity filtering process in removing the stellar activity signal.

8.1 Dynamos of young, sun-like stars

TWA 9A and V1095 Sco have very different brightness maps, even when taking their different $v \sin i$ values and therefore different spatial resolution of the maps into account. This may imply a difference in the underlying flux emergence patterns of these stars. The brightness map of TWA 9A shows evidence of both cool spots and bright plage, and resembles the topology of V819 Tau (Donati et al. 2015) and Par 1379 (Hill et al. 2017), which are both younger than TWA 9A, but have similar rotation periods and masses. V1095 Sco's map is dominated by a large cool polar spot, with weak evidence of plage on its surface. This is in contrast to all other wTTSs mapped in the MaTYSSE sample so far, which all exhibit plage signatures on their surfaces. However, the large polar spot, rapid rotation, poorer SNR, and poorer phase coverage of V1095 Sco make it unclear if this star is truly an outlier in the MaTYSSE sample. Of particular contrast to V1095 Sco is V830 Tau, which exhibits a more complex brightness topology, despite having a similar age, mass, $v \sin i$, rotation period, and internal structure. This difference can potentially be explained by shorter time-scale magnetic field evolution in these types of stars, and were they to be observed at a different epoch, might display similar characteristics. V1095 Sco's surface activity does resemble that of AB Doradus, a 50 Myr old, rapidly rotating post-T Tauri star, which displays a large polar spot in addition to some lower attitude spot features (Donati & Collier Cameron 1997; Donati et al. 2003; Hussain et al. 2007).

The reconstructed magnetic field topology of TWA 9A is predominantly poloidal (69 per cent poloidal) and non-axisymmetric (57 per cent non-axisymmetric), with the dipolar component tilted at 36 deg from the rotation axis. The overall field has a mean strength of 113 G and a maximum strength of 296 G. This resembles the topology and complexity of V819 Tau and Par 1379, but has the weakest intensity of dipole field of any mapped in the MaTYSSE

Downloaded from https://academic.oup.com/mnras/article-abstract/480/2/1754/5059584
by University of Southern Queensland user
on 23 August 2018

sample so far (V1095 Sco likely has a weaker field, but its magnetic field has not been mapped). Comparing to the MAPP sample of cTTS, TWA 9A is of a similar age and mass to V4046 Sgr A (Donati et al. 2011), and displays a similar level of axisymmetry, but again has a weaker field strength, and a more poloidal field. Comparing to a wider sample of young (<250 Myrs) stars from the TOUPIES (TOwards Understanding the sPIn Evolution of Stars) project presented by Folsom et al. (2016), TWA 9A has magnetic field characteristics within the range seen in that sample, despite it being ∼10 Myr younger than the youngest stars in that sample. This is consistent with the notion that rotation speed and internal structure play a dominant role in determining the magnetic, and hence surface, activity for young stars (Folsom et al. 2016; Gregory et al. 2016).

The longitudinal magnetic field was calculated for each observation of TWA 9A, giving values ranging from -68.3 ± 6.9 G to 32.6 ± 5.5 G, and varying over a period coinciding with the stellar rotation period. The longitudinal field was measured for the strongest and most reliable observation of V1095 Sco, giving a value of 25.9 ± 16.0 G. There are only two wTTSs in the literature with published longitudinal field measurements, namely TAP 26 (Yu et al. 2017) and V410 Tau (Skelly et al. 2010). Both have far higher maximum B_l values than either of the stars presented here, which also correlates with those stars having greater large-scale magnetic field strengths.

Differential rotation was investigated for both stars, but a solution was only found for TWA 9A. The intensity profiles of TWA 9A indicate strong differential rotation with an equatorial rotation of $\Omega_{\rm eq} = 1.273 \pm 0.007$ rad d^{-1} and shear of $\mathrm{d}\Omega = 0.05 \pm 0.02$ rad d^{-1}. This is very similar to the solar shear value of ∼0.055 rad d^{-1}, and is the largest Stokes I differential rotation measurement of the published MaTYSSE sample to date (though only marginally higher than that of LkCa 4; Donati et al. 2014).

In both stars, we observe emission in the H α region of their spectra as a diagnostic of their chromospheric activity. The emission is weaker for V1095 Sco than for TWA 9A, which is consistent with the idea of a weaker magnetic field in the former star. The shapes of the profile are different in each case, with V1095 Sco showing variation in the shape of the line profile, and excess emission on the blue-ward side of the H α region, indicative of mass motion towards the observer. In contrast, TWA 9A shows symmetric, double peaked emission that varies cyclically in intensity, with the exception of a possible flare event on June 3 that exhibits far higher and broader emission.

In overall terms, the observed behaviour of both stars is consistent with intense magnetic activity. Comparing to the H α emission published for other stars in the MaTYSSE sample, namely Par 1379, Par 2244 and V410 Tau, the emission of V1095 Sco is the weakest, and V1095 Sco is the only one to exhibit excess emission on the blue-ward side of the profile. TWA 9A has emission intensity on the same order as the other MaTYSSE stars, but does not show the same level of rotational and temporal variability of intensity, or profile shape. Comparing to the H α emission of TWA 17 published by Skelly et al. (2009), a star of the similar age, mass and spectral type, we see on average weaker emission for TWA 9A, which is likely explained by the slower rotation of TWA 9A leading to comparatively lower activity. The broad 'pedestal' emission (emission in the line far outside the rotational broadening limits) seen in the mean H α of TWA 17, which is linked to the presence of microflaring (e.g. Fernandez et al. 2004), is absent from the H α emission of TWA 9A, but is seen in the enhanced emission on June 3, further supporting the idea that this enhanced emission has resulted from a flaring event.

8.2 Exoplanets around young stars

In addition to the study of wTTS dynamos, the other aim of the MaTYSSE Programme is the search for young, close-in, giant exoplanets. Here, we analyse the radial velocity curves of both stars to search for a planet-induced radial velocity signal. Since both stars exhibit strong surface activity, and hence activity jitter in their radial velocity curves, we use our DI analysis to characterize and remove this jitter. By doing this, we reduce the radial velocity RMS in V1095 Sco from 137 to 48 m s^{-1}, and in TWA 9A from 187 to 25 m s^{-1}. No signal is found in the filtered radial velocity curve, allowing us to rule out the presence of a ∼1.0 Jupiter mass planet closer than ∼0.1 au in the case of V1095 Sco, and a planet larger than ∼0.4 Jupiter masses and closer than ∼0.1 au for TWA 9A. This difference in detection limits for the two stars is likely due to the differences in rotation rates and quality of the respective data sets. V1095 Sco has a $v \sin i$ nearly three times that of TWA 9A, so has greater Doppler broadening of its spectra, which decreases the precision of the radial velocity measurements. In addition to that, V1095 Sco's data have a lower signal-to-noise ratio, which not only impacts the precision of the radial velocity measurements themsleves, but also affects the quality of the DI fits. This, in turn, results in a poorer filtering of the activity jitter, leading to less of a reduction in radial velocity RMS in V1095 Sco compared to TWA 9A.

Of the eight MaTYSSE stars studied so far, there have been two exoplanet detections, one each for V830 Tau (Donati et al. 2015; Donati et al. 2016, 2017) and TAP 26 (Yu et al. 2017). This puts the occurrence rate of close-in hot Jupiters in the MaTYSSE sample at 1 in 4, which appears remarkably high in comparison to the ∼1 per cent occurrence rate in MS stars from transit and radial velocity surveys (Guo et al. 2017). In addition to the planets found by MaTYSSE, David et al. (2016) found a close-in Neptune-sized planet around a 5–10Myr old star, detected through the transit method. Given these independent detections of young close-in planets, further work is needed to understand their formation and eventual fate as their host stars evolve onto the main sequence.

ACKNOWLEDGEMENTS

This work has made use of the VALD database, operated at Uppsala University, the Institute of Astronomy RAS in Moscow, and the University of Vienna. This work has made use of data from the European Space Agency (ESA) mission *Gaia* (http://www.cosmos.esa.int/gaia), processed by the *Gaia* Data Processing and Analysis Consortium (DPAC, http://www.cosmos.esa.int/web/gaia/dpac/consortium). Funding for the DPAC has been provided by national institutions, in particular the institutions participating in the *Gaia* Multilateral Agreement. We also warmly thank the IDEX initiative at Université Férale Toulouse Midi-Pyr´ees (UFTMiP) for funding the STEPS collaboration programme between IRAP/OMP and ESO and for allocating a 'Chaire d'Attractivité' to GAJH, allowing her to regularly visit Toulouse to work on MaTYSSE data. This research is supported by USQ's Strategic Research Initiative programme.

REFERENCES

Alvarado-Gómez J. D. et al., 2015, A&A, 582, A38
Baraffe I., Homeier D., Allard F., Chabrier G., 2015, A&A, 577, A42

Downloaded from https://academic.oup.com/mnras/article-abstract/480/2/1754/5059584
by University of Southern Queensland user
on 23 August 2018

Bertout C., Robichon N., Arenou F., 1999, A&A, 352, 574
Bouvier J., 2013, in Hennebelle P., Charbonnel C., eds, EAS Publ. Ser. Vol. 62, Angular Momentum Transport During Star Formation and Evolution. Cambridge Univ. Press, Cambridge, p. 143
Buscombe W., 1981, MK spectral classifications. Fifth general catalogue, 5th edn. Northwestern University, Evanston
Buscombe W., 1988, MK spectral classifications. Seventh general catalogue, 7th edn. Northwestern University, Evanston
Butler R. P., Marcy G. W., Williams E., McCarthy C., Dosanjh P., Vogt S. S., 1996, PASP, 108, 500
Cieza L. A. et al., 2013, ApJ, 762
Collier Cameron A., 1997, MNRAS, 287, 556
Comerón F., 2008, in Reipurth B., ed., ASP Monograph Publications, Vol. 5, Handbook of Star Forming Regions, Volume II: The Southern Sky. ASP Monograph Publ., San Francisco, CA, p. 295
David T. J. et al., 2016, Nature, 534, 658
Donati J. F., Semel M., Carter B. D., Rees D. E., Collier Cameron A., 1997, MNRAS, 291, 658
Donati J. F. et al., 2006, MNRAS, 370, 629
Donati J. F. et al., 2012, MNRAS, 425, 2948
Donati J. F. et al., 2014, MNRAS, 444, 3220
Donati J. F. et al., 2015, MNRAS, 453, 3706
Donati J. F. et al., 2016, Nature, 534, 662
Donati J.-F., Collier Cameron A., 1997, MNRAS, 291, 1
Donati J.-F. et al., 2003, MNRAS, 345, 1145
Donati J.-F. et al., 2007, MNRAS, 380, 1297
Donati J.-F. et al., 2008, MNRAS, 386, 1234
Donati J.-F. et al., 2010, MNRAS, 409, 1347
Donati J.-F. et al., 2011, MNRAS, 417, 1747
Donati J.-F. et al., 2017, MNRAS, 465, 3343
Fernandez M. et al., 2004, A&A, 427, 263
Folsom C. P. et al., 2016, MNRAS, 457, 580
Folsom C. P. et al., 2018, MNRAS, 474, 4956
Gaia Collaboration Brown A. G. A., Vallenari A., Prusti T., de Bruijne J. H. J., Babusiaux C., Bailer-Jones C. A. L., 2018, A&A, preprint (arXiv:1804.09365)
Gaia Collaboration et al., 2016, A&A, 595, A1
Gregory S. G., Donati J.-F., Morin J., Hussain G. A. J., Mayne N. J., Hillenbrand L. A., Jardine M., 2012, ApJ, 755, 97
Gregory S. G., Adams F. C., Davies C. L., 2016, MNRAS, 457, 3836
Grunhut J. H. et al., 2013, MNRAS, 428, 1686
Guo X., Johnson J. A., Mann A. W., Kraus A. L., Curtis J. L., Latham D. W., 2017, ApJ, 838, 25
Hébrard É. M., Donati J. F., Delfosse X., Morin J., Moutou C., Boisse I., 2016, MNRAS, 461, 1465
Henden A. A., Templeton M., Terrell D., Smith T. C., Levine S., Welch D., 2016, VizieR Online Data Catalog, 2336
Herczeg G. J., Hillenbrand L. A., 2014, ApJ, 786, 97
Hill C. A., Carmona A., Donati J. F., Hussain G. A. J., Gregory S. G., Alencar S. H. P., Bouvier J. The Matysse Collaboration, 2017, MNRAS, 472, 1716
Hussain G. A. J., Donati J.-F., Collier Cameron A., Barnes J. R., 2000, MNRAS, 318, 961
Hussain G. A. J. et al., 2007, MNRAS, 377, 1488
Hussain G. A. J. et al., 2009, MNRAS, 398, 189
Hussain G. A. J. et al., 2016, A&A, 585, A77
Krautter J., Wichmann R., Schmitt J. H. M. M., Alcal J. M., Neuh user R., Terranegra L., 1997, A&AS, 123, 329
Mamajek E. E., 2005, ApJ, 634, 1385
Manara C. F. et al., 2013, A&A, 551, A107
Marsden S. C. et al., 2014, MNRAS, 444, 3517
McDonald I., Zijlstra A. A., Boyer M. L., 2012, MNRAS, 427, 343
Pecaut M. J., Mamajek E. E., 2013, ApJS, 208, 9
Ryabchikova T., Piskunov N., Kurucz R. L., Stempels H. C., Heiter U., Pakhomov Y., Barklem P. S., 2015, Phys. Scr., 90, 054005
Sartori M. J. , Lépine J. R. D., Dias W. S., 2003, A&A, 404, 913
Semel M., 1989, A&A, 225, 456
Siess L., Dufour E., Forestini M., 2000, A&A, 358, 593
Skelly M. B., Unruh Y. C., Barnes J. R., Lawson W. A., Donati J. F., Cameron A. C., 2009, MNRAS, 399, 1829
Skelly M. B., Donati J.-F., Bouvier J., Grankin K. N., Unruh Y. C., Artemenko S. A., Petrov P., 2010, MNRAS, 403, 159
Skilling J., Bryan R. K., 1984, MNRAS, 211, 111
Valenti J. A., Fischer D. A., 2005, ApJS, 159, 141
Wahhaj Z. et al., 2010, ApJ, 724, 835
Weinberger A. J., Anglada-Escudé G., Boss A. P., 2013, ApJ, 767, 96
Yu L. et al., 2017, MNRAS, 467, 1342
Zechmeister M., Kürster M., 2009, A&A, 496, 577

This paper has been typeset from a TEX/LATEX file prepared by the author.

Downloaded from https://academic.oup.com/mnras/article-abstract/480/2/1754/5059584
by University of Southern Queensland user
on 23 August 2018

3

The Surface Magnetic Activity of the M-type Weak-Line T Tauri Stars TWA 25 and TWA 7

Prepared for publication in the Monthly Notices of the Royal Astronomical Society.

MNRAS **000**, 1–13 (2018) Preprint 12 December 2018 Compiled using MNRAS LATEX style file v3.0

The Surface Magnetic Activity of the M-type Weak-Line T Tauri Stars TWA 25 and TWA 7

B. A. Nicholson,[1]★ G. Hussain,[2] D. Wright,[1] J. F. Donati,[3,4] C. Folsom,[3,4] R. Wittenmyer,[1] B. D. Carter,[1] and the MaTYSSE collaboration
[1] *University of Southern Queensland, Centre for Astrophysics, Toowoomba, Australia*
[2] *European Southern Observatory, Karl Schwarzschild Str. 2, 85748 Garching, Germany*
[3] *Univ. de Toulouse, UPS-OMP, IRAP, 14 av Belin, F31400 Toulouse, France.*
[4] *CNRS, IRAP / UMR 5277, 14 av Belin, F31400 Toulouse, France.*

Accepted XXX. Received YYY; in original form ZZZ

ABSTRACT
We present analysis of spectropolarimetric observations of the M-type weak-line T Tauri stars TWA 25 and TWA 7. The large-scale magnetic fields were reconstructed for both stars, revealing predominantly toroidal and non-axisymmetric fields for both stars, especially for TWA 25. These maps add to the diversity of magnetic fields seen in pre-main sequence stars. We reconstruct the large scale brightness distribution for TWA 25, and use this to filter out the activity-induced radial velocity jitter, reducing the RMS of the radial velocity variations from 495 $\mathrm{m\,s^{-1}}$ to 32 $\mathrm{m\,s^{-1}}$. While the $v\sin(i)$ of TWA 7 is too small to permit the reconstruction of a reliable brightness map, we find significant radial velocity variations of 163 $\mathrm{m\,s^{-1}}$, which are anti correlated with the variations in the longitudinal magnetic field. We conclude that this variability is most likely caused by rotationally modulated activity.

Key words: stars:magneticfields, techniques:polarimetric, stars:formation, stars:imaging, stars: individual: TWA 25, stars: individual: TWA 7

1 INTRODUCTION

Magnetic fields play a key role in the evolution of low mass stars onto the pre-main sequence (PMS), particularly during the T Tauri stage of cool star evolution. The T Tauri stage is divided into two major categories: classical T Tauri stars (cTTSs), and weak-line T Tauri stars (wTTSs). The cTTS stage starts when the central star has emerged form the cocoon of gas in which it formed, and is surrounded by a substantial disc of gas and dust, from which matter is accreted onto the stellar surface. At this time, magnetic fields are thought to help dissipate the angular momentum of the star and accreting matter such that the stellar rotation does not reach break-up speed as it forms. Once the gas from the inner disc is cleared and accretion has ceased, the star is the classed as a wTTS; a fully formed star that is still undergoing contraction towards its main sequence size.

The study of the differences between these populations of PMS stars has been one of the goals of the Magnetic Topologies of Young Stars and Survival of close in Giant Exoplanets (MaTYSSE) large program. MaTYSSE is a multi-telescope programme using high resolution spectropolarimetric observations to map the large scale brightness and magnetic fields of a range of wTTSs, and compare them to a sample of cTTSs observed in the Magnetic Protostars and Planets[1] (MaPP) program (see e.g. Donati et al. 2007, 2008; Donati et al. 2010a; Donati et al. 2011a; Donati et al. 2012; Hussain et al. 2009).

Few M-type stars have been observed in either sample, as their peak emission in the infrared and low brightness make them challenging targets for the current optical spectropolarimeters. Within the MaPP sample there have been 2 M type PMS stars published, namely DN Tau (Donati et al. 2013) and V2247 Oph (Donati et al. 2010a). The magnetic field of the latter star appeared significantly different, being fully convective like its higher mass counterparts of the same age, but displaying a wildly different magnetic field morphology.

To further our understanding of M-type PMS dynamo fields, this work presents analysis of high-resolution spectropolarimetric data of two M-type weak-line T Tauri stars as part of the MaTYSSE sample: TWA 25 and TWA 7. Both are 10Myr old M type stars in the TW Hya association (Mentuch et al. 2008), and represent more evolved versions

★ E-mail: belinda.nicholson@usq.edu.au

[1] https://wiki.lam.fr/mapp/FrontPage

© 2018 The Authors

of the the two MaPP M-type stars. We reconstruct both the surface brightness and magnetic field morphologies of TWA 25, and the large-scale magnetic field of TWA 7. In addition we examine the variation in longitudinal (line of sight) magnetic field with stellar rotation for both stars, as well as the spectral activity markers of Hα and Na I doublet indices.

The other major focus of the MaTYSSE program is the search for close-in giant planets around wTTSs. Finding planets around very active stars is challenging, as the surface activity of these stars can contribute radial velocity variations on the order of hundreds of meters per second, obscuring even a giant planet's signal. The MaTYSSE program has addressed this by using the surface activity information provided from surface brightness mapping to measure and remove the radial velocity contribution due to this activity (Donati et al. 2014). This work, therefore, also analyses the radial velocities of TWA 25 and TWA 7, and for TWA 25 we use the surface brightness information from our Doppler mapping to filter out activity jitter from its radial velocities.

In Section 2 we detail the observations and data processing of TWA 25 and 7. The evolutionary states of both stars are determined, and the stellar properties calculated in Section 3. Section 4 describes the mapping of large-scale brightness and magnetic fields, Section 5 explores the rotational modulation of the longitudinal magnetic field and activity indices, and Section 6 describes our analysis of the radial velocities for both stars. Lastly, we summarise and discuss our findings in Section 7.

2 OBSERVATIONS

High-resolution spectropolarimetric data were taken for TWA 25 and TWA 7 using the HARPS spectropolarimeter on the ESO 3.6m telescope in La Silla, Chile. TWA 25 was observed over 15 nights from March 12$^{\text{th}}$ to 31$^{\text{st}}$, 2017. Journals if the observations for each star are given in Tables 1 and 2. Each observation consists of 4 sub-exposures with alternating configurations of a quarter wave plate to remove first order spurious polarisation signals. Two observations of TWA 7 contain only two sub-exposures due to weather, and so are only used for analysis involving brightness information, and are excluded from the magnetic field analysis. Our spectra have a wavelength coverage of ~380 nm to ~690nm, and spectral resolution of ~115000. The spectral data were reduced using the Libre ESpRIT pipeline software adapted for use with HARPS polarimetric data (Hébrard et al. 2016), following the procedure outlined in Donati et al. (1997). Across our observations we attain a peak circular polarisation (Stokes V) signal-to-noise ratio (SNR) of between 72 and 116 for TWA 25 and between 71 and 110 for TWA 7.

2.1 Least Squares Deconvolution

To increase the signal-to-noise for our tomographic mapping, we combine the lines in our observed spectra using Least Squares Deconvolution (LSD, Donati et al. 1997). This process combines the signal in absorption features, by deconvolving our observed spectra with a mask of photospheric lines constructed using the Vienna Atomic Line Database (VALD3, Ryabchikova et al. 2015) based on the effective temperature and surface gravity of each star (see Section 3), and removing lines in emission, or with broad absorption. Given the abundance in these stars of weak and blended absorption lines, we remove lines with a strength relative to the deepest lines of less than 0.1, as per Nicholson et al. (2018). After generating these LSD profiles, the continuum level was renormalised, and all were scaled by the mean equivalent width for each star. For TWA 25, the peak SNR in the intensity and circular polarisation spectra are 123 and 119, increasing to 637 and 4763 in the Stokes I and Stokes V LSD profiles. For TWA 7, we obtain a peak SNR in our intensity and circular polarisation spectra of 111 and 110, increasing to 400 and 3882 in the Stokes I and Stokes V LSD profiles.

3 EVOLUTIONARY STATES OF TWA 25 AND TWA 7

TWA 25 and TWA 7 are both single stars in the TW Hya. association (Song et al. 2003; Webb et al. 1999), which has a mean age of 10Myrs (Mentuch et al. 2008). To estimate the individual ages and hence evolutionary states for each star, we use their effective temperatures from the literature, and calculate their bolometric luminosities here.

There are a number of effective temperature estimates for both stars in the literature ranging from 3742 K (da Silva et al. 2009) to 4250 K (Ammons et al. 2006) for TWA 25, and from 3300 K (Yang et al. 2008) to 4017 K (Gaia Collaboration et al. 2018) for TWA 7. Such a range in effective temperatures is unsurprising for pre-main sequence stars, and is likely due to the differences in methods used, and the sensitivity of those methods to the presence of spots on the photosphere. For this work we use the effective temperature values of Mentuch et al. (2008), who have consistently analysed low resolution spectra of both TWA 7 and TWA 25, and use select atomic absorption regions to model the effective temperature and surface gravity of each star. We use Mentuch et al.'s estimate of the external uncertainties of the T_{eff} values of ±150 K and $\log(g)$ values of ±0.5 dex, as the external uncertainty more accurately reflects the true uncertainty of these quantities.

Stellar luminosity is calculated for both stars based on their apparent magnitudes, extinction estimates, bolometric corrections and distances. For TWA 25 we use an apparent magnitude of 11.160 ± 0.083 mag from Henden et al. (2016), and a bolometric correction of -1.19 ± 0.06 mag from Pecaut & Mamajek (2013). Interstellar extinction, A_v, is calculated using the observed B-V colour of 1.428±0.162 mag from Henden et al. (2016) and intrinsic colour, $(\text{B-V})_0$, of 1.33 ± 0.04 mag from Pecaut & Mamajek (2013), giving $A_v = 0.3 \pm 0.5$ mag for TWA 25. The distance to TWA 25 is calculated as 53.1±0.2 pc from parallax measurements from Gaia Data Release 2 (DR2, Gaia Collaboration et al. 2016, 2018). These values result in a luminosity of 0.3 ± 0.1 $L_\odot$ for TWA 25. This value is higher than any previously published values, though the large uncertainty means that is it in agreement with all values, except for the value of 0.077 $L_\odot$ from Gaidos et al. (2014), who treat TWA 25 as a main-sequence M dwarf. Our luminosity value is in closest agreement with the value of 0.252 $L_\odot$ published by McDonald et al. (2017), who estimate an even higher extinction value of 0.643 mag, but use a smaller distance derived from the first Gaia data release. The extinction values for TWA 25 are all calculated as

Table 1. Journal of observations for star TWA 25. From left to right, this table lists the date of observation, the Heliocentric Julian date, the exposure time as a set of sub-exposures, the stellar rotational phase based on a period of 5.05 days (with the zero-point set as the middle of the first observation), the peak SNR in the Stokes V spectra per observation, and the SNR in Stokes V after lease squares deconvolution (LSD, see Section 2.1).

Date (2017)	HJD (2457000+)	Exposure Time (s)	Rotation Cycle	Stokes V Obs. SNR	Stokes V LSD SNR
12 March	825.83150	4×1600	0.00	103.0	4322
13 March	826.82463	4×1600	0.20	74.0	2863
16 March	829.80554	4×1600	0.79	116.0	4736
17 March	830.83104	4×1600	0.99	92.0	3753
18 March	831.81629	4×1600	1.19	102.0	4023
20 March	833.81797	4×1600	1.58	83.0	3258
21 March	834.86501	4×1600	1.79	111.0	4354
22 March	835.86077	4×1600	1.99	95.0	3666
23 March	836.82937	4×1600	2.18	91.0	3439
24 March	837.82846	4×1600	2.38	88.0	3379
25 March	838.82821	4×1600	2.57	91.0	3528
26 March	839.82925	4×1600	2.77	119.0	4763
27 March	840.83804	4×1600	2.97	95.0	3780
28 March	841.82974	4×1600	3.17	72.0	2737
30 March	843.82681	4×1600	3.56	104.0	4137
31 March	844.83717	4×1600	3.76	105.0	4175

Table 2. Table of observations for star TWA 7. For description, see caption of Table 1. Rotation cycle is calculated based on a 5.01 day period.

Date (2017)	HJD (2457000+)	Exposure Time (s)	Rotation Cycle	Stokes V Obs. SNR	Stokes V LSD SNR
12 March	825.75835	4×1300	0.00	73.0	2414
13 March	826.74890	4×1500	0.19	71.0	2499
16 March	829.69035	4×1600	0.78	110.0	3882
17 March	830.75377	4×1600	0.99	92.0	3225
18 March	831.72533	2×1600	1.19	72.0	2631
19 March	832.72506	2×1600	1.39	55.0	2042
21 March	834.78337	4×1650	1.80	82.0	2831
22 March	835.78202	4×1650	2.00	71.0	2403
23 March	836.74918	4×1750	2.19	87.0	2993
24 March	837.74774	4×1750	2.39	101.0	3666
25 March	838.53731	4×1750	2.55	106.0	3933
25 March	838.74812	4×1750	2.59	92.0	3242
26 March	839.74884	4×1750	2.79	101.0	3537
27 March	840.75775	4×1750	2.99	98.0	3336
28 March	841.74953	4×1750	3.19	74.0	2572
30 March	843.74606	4×1750	3.59	101.0	3533
31 March	844.75641	4×1750	3.79	105.0	3561

greater than zero despite its close proximity (making significant interstellar extinction unlikely), indicating that there may be reddening due to the near-edge-on disc surrounding it (Choquet et al. 2016), or reddening due to spots on the stellar surface.

For TWA 7, we use an apparent magnitude of 11.754 ± 057 mag from Henden et al. (2016), and a bolometric correction of -1.72 ± 0.08 mag from Pecaut & Mamajek (2013). We calculate A_v using observed B-V colour of 1.475 ± 0.063 mag from Henden et al. (2016) and $(B\text{-}V)_0$ of 1.462 ± 0.004 from Pecaut & Mamajek (2013), giving $A_v = 0.04 \pm 0.2$ mag for TWA 7. The Gaia DR2 parallax measurement of TWA 7 gives a distance of 34.03 ± 0.08 pc. These values result in a luminosity of 0.09 ± 0.02 $L_\odot$ for TWA 7. This value is also in good agreement with the all literature values, with the exception of a very high estimate of 0.32 $L_\odot$ by López-Martínez & Gómez de Castro (2015), who assume zero extinction, but use a smaller distance. Our estimate of extinction, given its large uncertainties, in equivalent to the usual assumed extinction of zero for this star.

Using our calculated luminosities and Mentuch et al. (2008) effective temperatures, we calculate mass, age and stellar radius for both stars based on the Baraffe et al. (2015) pre-main sequence stellar evolution models. The locations of TWA 25 and TWA 7 on the HR diagram with respect to these mass tracks and isochrones are shown in Figure 1. For TWA 25 we find a mass of $0.67^{+0.06}_{-0.2}$ $M_\odot$, age of 5^{+35}_{-4} Myrs and radius of 1.2 ± 0.4 $R_\odot$, and for TWA 7 we find a mass of 0.4 ± 0.1 $M_\odot$, age of 10^{+26}_{-7} Myrs and radius of 0.82 ± 0.13. The age estimates for both stars are in agreement with the average age 10 Myrs the TW Hya Association. These stars straddle the radiative core formation boundary (solid green line in Figure 1), with TWA 7 expected to still be fully convective, and TWA 25 estimated to have formed a

radiative core of size 0.2 ± 0.2 R$_*$. A summary of the stellar parameters are given in Table 3.

3.1 Determining stellar radius and inclination

Stellar inclination is a key parameter for our tomographic modelling. For TWA 25 and TWA 7 we consider both the estimates of debris disc inclination from imaging studies as a proxy for stellar inclination, and calculate the inclination based on stellar parameters. Choquet et al. (2016) imaged both TWA 25 and TWA 7 with NICMOS on the Hubble Space Telescope, and calculate a disc inclination of 75 ± 6 degrees for TWA 25 and 22 ± 22 degrees for TWA 7. TWA 7 has also been observed by Olofsson et al. (2018) who used SPHERE on ESO's Very Large Telescope, refining TWA 7's disc inclination to $13.1^{+3.1}_{-2.6}$ degrees.

We calculate the inclination from the measured $v \sin(i)$ and $P_{\rm rot}$ values in our data, and the stellar radius determined from our bolometric luminosities and effective temperatures determined above. For TWA 25, no combination of effective temperatures or luminosities in the literature, nor the luminosity calculated in this work results in a radius that give a value of $\sin i$ less than 1, meaning that they are not physically meaningful given our estimates of the $v \sin(i)$ or rotation period. This could be due to an underestimate in the bolometric correction and/or extinction, or an under estimate of the distance in the calculation of luminosity. Since we are unable to calculate the inclination from stellar parameters, we use the inclination of the debris disc of 75 ± 6 degrees from Choquet et al. (2016) for our tomographic modelling. We test to see if this inclination is physically feasible by reversing our inclination calculation to find corresponding theoretical radius. Given our $v \sin(i)$ and rotation period values we find a theoretical radius of $1.37 R_\odot$, which agrees with our estimates from PMS evolution models within the 1σ uncertainty.

In the case of TWA 7, we calculate an inclination of $39° \pm 8°$ using our radius calculated from the effective temperature and luminosity determined above. We again test to see if it is feasible for the star to have the same inclination as the disc, given our measured $v \sin(i)$ and $P_{\rm rot}$. For an inclination value of 13.1 degrees we find a theoretical radius of $2.2\,R_\odot$. This is far larger than any radius suggested by the PMS models for a star of this temperature and luminosity, and is unlikely given the age of this star and star forming region. This is also true for radii calculated from inclinations 3σ above the disc inclnation estimate. We thus conclude that the observed disc is misaligned from the stellar rotation axis, and use our calculated inclination of $39° \pm 8°$ for our tomographic modelling.

4 TOMOGRAPHIC MODELLING

4.1 Doppler Imaging

Using the Stokes I LSD profiles described in Section 2.1, and the stellar parameters given in Table 3, we reconstruct the surface brightness of TWA 25 using the technique of Doppler Imaging (DI). For this we used the DoTS code (Collier Cameron 1997), which has been modified to now reconstruct areas of both bright plage and cool spot, as described in Donati et al. (2014). This code inverts the Stoke I data and applies a maximum entropy regularisation to determine the simplest map that best fits our data. The surface brightness was reconstructed assuming a Milne-Eddington model atmosphere for the local line profile, and using mean Landé factor of 1.192, mean wavelength of 544nm (same as for our LSD profiles) and a linear limb darkening coefficient of 0.72. In this process we are able to estimate the average radial velocity, rotation period and $v \sin(i)$ of TWA 25, and these are found to be 7.94 ± 0.01 km s^{-1}, 5.05 ± 0.01 days and 13.32 ± 0.01 km s^{-1}, respectively. Our fit is shown in red in Figure 2, and our reconstructed surface brightness map is shown in figure 4. TWA 25 display large areas of both bright plage and cool spots and mid to low latitudes. Due to the high inclination angle of the star, this solution does show some 'mirroring' phenomena about the equator, as the DI process is unable to constrain the hemisphere of lower latitude features.

We attempt a DI analysis for TWA 7, but are unable to obtain a satisfactory fit to the bottom of these profile, likely

Table 3. Summary of the properties of TWA 25 and 7. Uncertainties are given where available. References: [1] Mentuch et al. (2008), [2] Choquet et al. (2016)

	TWA 25	TWA 7
Mass, M_* ($M_\odot$)	$0.67^{+0.06}_{-0.2}$	0.4 ± 0.1
Radius, R_* ($R_\odot$)	1.2 ± 0.4	0.82 ± 0.13
$R_* \sin i$ ($R_\odot$)	1.330 ± 0.003	0.510 ± 0.005
Age (Myrs)	5^{+35}_{-4}	10^{+26}_{-7}
Luminosity, L_* ($L_\odot$)	0.3 ± 0.2	0.09 ± 0.03
Distance, (pc)	53.1 ± 0.2	34.03 ± 0.08
Extinction, A_v (mag)	0.3 ± 0.6	0.04 ± 0.2
$v \sin(i)$ (km s^{-1})	13.32 ± 0.01	5.15 ± 0.05
Rotation Period, $P_{\rm rot}$ (Days)	5.05 ± 0.01	5.01 ± 0.01
Effective Temperature, $T_{\rm eff}$ (K)	3920 ± 150 [1]	3540 ± 150 [1]
Surface Gravity, log(g)	4.45 ± 0.5 [1]	4.18 ± 0.5 [1]
Inclination Angle, i (Degrees)	75 ± 6 [2]	39 ± 8

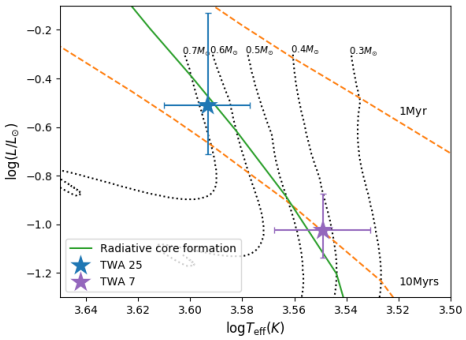

Figure 1. HR diagram showing the locations, including 1σ uncertainties, of TWA 25 (blue) and TWA 7 (purple) with relation to the Baraffe et al. (2015) PMS evolutionary models. The black dotted lines are evolutionary tracks for $0.7\,M_\odot$, $0.6\,M_\odot$, $0.5\,M_\odot$, $0.4\,M_\odot$ and $0.3\,M_\odot$, and the orange dashed lines are isochrones for 1 Myr and 10 Myrs. The solid green line indicates the boundary between full convection and the formation of a radiative core.

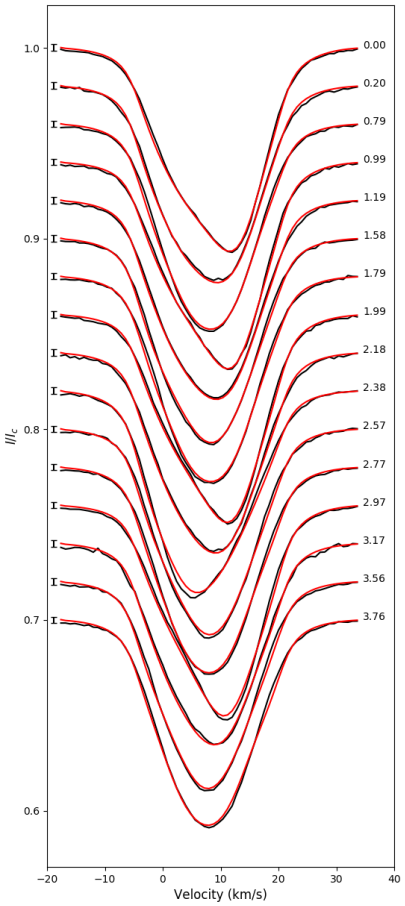

Figure 2. Stokes I LSD profiles of TWA 25(black line), and Doppler Imaging fits to these profiling using DoTS (red line). Mean 1σ error bars are given to the left of each profile, and rotation phase is given on the right.

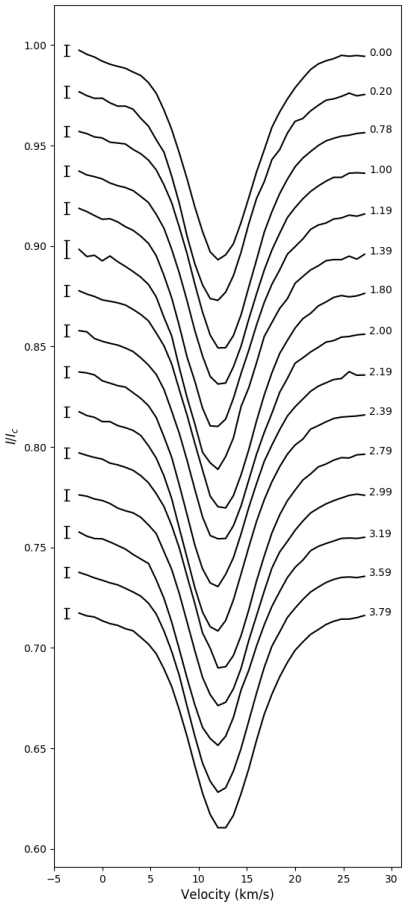

Figure 3. Stoke I LSD profiles of TWA 7. Mean 1σ error bars are given on the left-hand side of each profile, and rotation phase is given on the right.

due to the small $v\sin(i)$. Nevertheless, we are able to determine a mean radial velocity of 12.22 ± 0.03, a rotation period of 5.01 ± 0.01 days, and a $v\sin(i)$ value of $5.15\pm0.05\mathrm{km\,s^{-1}}$. In addition, the significant radial velocity variations observed in Stokes I around this mean (see Figure 3, and see also the discussion in Section 6) indicate there may be large, low latitude spots present.

4.2 Zeeman Doppler Imaging

The large-scale surface magnetic fields are reconstructed for each star from their Stokes V LSD profiles using the Zeeman Doppler Imaging (ZDI) code ZDIPy. This code follows the method of Semel (1989); Donati et al. (1997, 2006), where the magnetic field is expressed as a series of spherical harmonics, and uses a maximum entropy regularisation to find the simplest field configuration that best fits our Stokes V LSD profiles. The stokes V are modelled in a weak field approximation, using a mean Landé factor and central wave-

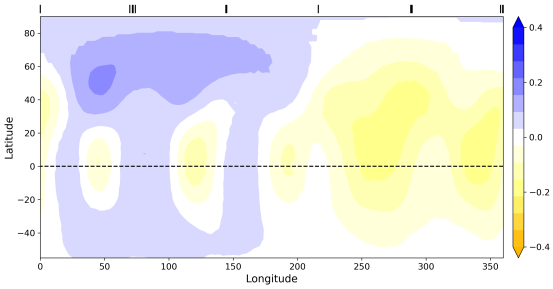

Figure 4. Surface brightness map of TWA 25, showing areas of bright plage (blue, > 0), and areas of cool spot (yellow, < 0), relative to the photosphere (0.0). The black dashed line indicates the equator, and the top tick marks indicate observed longitudes.

length equivalent to those of the Stokes V LSD profiles. We use the same set of stellar parameters as in our DI analysis, defining an equivalent local line profile with a Voight profile.

For TWA 25 the reconstructed radial, azimuthal and meridional components of the large-scale magnetic file are shown in Figure 7, with the associated fits of the stokes V profiles shown in figure 5. In the fitting process we investigate the presence of differential rotation, and find a best fit equatorial rotation period of 4.95 ± 0.08 days, and a shear value of 0.2 ± 0.13 radians/day. Our reconstructed field has a mean field strength of 270 G, and a maximum field strength of 952 G. The maps show a far stronger azimuthal field compared to the radial or meridional field, and a high level of complexity and asymmetry in the radial component. We quantify this by examining the distribution of energy among the different spherical harmonic components. This solution indicates a dominantly toroidal field (75% energy in toroidal components). The poloidal field is highly non-axisymmetric, with 94% of the poloidal field energy not aligned with the stellar rotation axis. The pole of the dipolar field is offset 38.5 degrees from the rotation axis, aligned with a longitude of 36.2 degrees (rotation phase 0.90).

The reconstructed large-scale magnetic field maps for TWA 7 are shown in Figure 8, and the fits to the Stokes V LSD profiles are shown in Figure 6. Given the poorer signal-to-noise of these observations, we note in Figure 6 which profiles are definite magnetic detections, defined as having a false alarm probability (FAP) less than 10^{-5}, or a marginal detection with a FAP between 10^{-5} and 10^{-3}. Not included in this figure are profiles that have no detectable magnetic signature (FAP greater than 10^{-3}), or observations without the full set of 4 sub-exposures, as they are also excluded from the ZDI analysis. We are unable to obtain information about any surface differential rotation, though we do obtain a best fit rotation period of 5.01 ± 0.01 days, which is in agreement with the rotation period determined from Doppler imaging using just the intensity profiles. The resulting reconstructed large-scale magnetic field has a mean strength of 65 G and a maximum strength of 167 G. The maps, as with TWA 25, show a strong azimuthal band at mid latitudes, though in this case it is equal in strength to the radial field. The meridional field is weaker, but this is typically the case with ZDI, as there can be significant

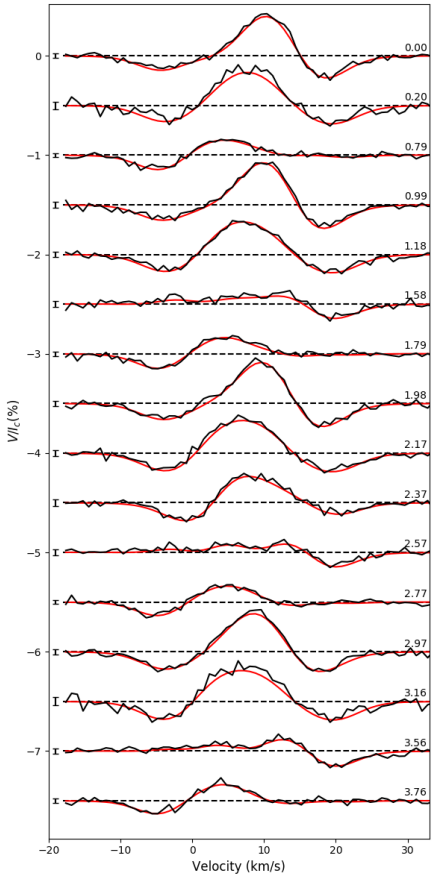

Figure 5. Circular polarisation (Stokes V) LSD profiles for TWA 25 (black line), with fit from Zeeman Doppler Imaging (red line). Mean error bars for each observation are shown on the left had sode, and rotation phase of each observation is given on the right hand side.

crosstalk between the meridional and radial magnetic field components. We again quantify the large-scale by examining the percentage of energy divided among the different magnetic field components. We see significant toroidal field (59% energy in toroidal components), but a simpler poloidal filed than that of TWA 25, with greater than 75% of the energy in the dipolar and quadrupolar components. The poloidal field has marginally more energy in axisymmetric components than non-axisymmetric components (51% axisymmetric), with the pole of the dipolar field offset by 56.5 degrees from the rotation axis, aligned with 247.8 degrees longitude (rotation phase 0.31).

5 LONGITUDINAL MAGNETIC FIELD, AND ACTIVITY INDICATORS

In addition to reconstructing the large brightness and magnetic field morphologies, we explore other probes of stellar

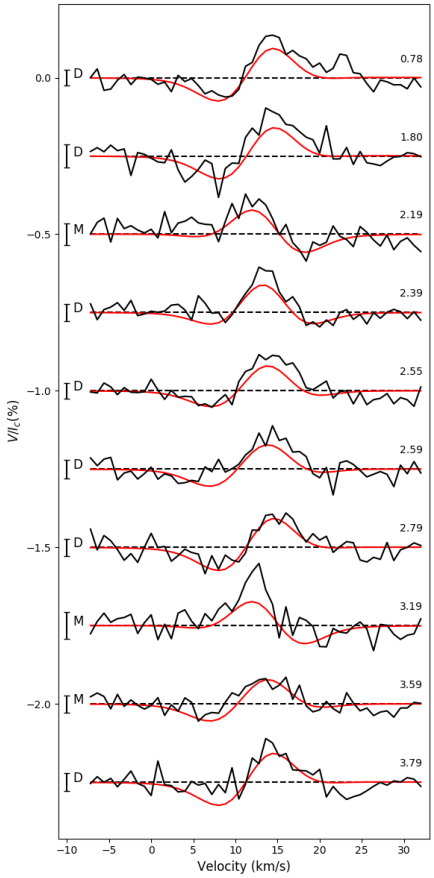

Figure 6. Circular polarisation (Stokes V) LSD profiles for TWA 7 (black line), with fit from Zeeman Doppler Imaging (red line). On the left hand side of each profile is the ean error bar, and a letter denoting the level of magnetic signal detection for each observation are shown on the left had side, and rotation phase of each observation is given on the right hand side.

magnetic activity namely the line-of-sight, or longitudinal, magnetic field, B_l, and the Hα and Na I doublet indices. These are plotted for both stars in Figures 9 and 10. The longitudinal magnetic field is calculated for each Stokes V profile, as in Grunhut et al. (2013), using the mean Landé factor and mean wavelength of our Stokes V LSD profiles. For TWA 7 we exclude incomplete observations (only two of the four required sub-exposures completed), as they likely contain spurious signal. We define an Hα index as per Marsden et al. (2014), using a rectangular emission bandpass of 0.36 nm, centred on 656.285 nm, and two continuum bandpasses in 0.22 nm, centred on 655.885 nm and 656.730 nm. For Na I doublet indices we define the index as in Gomes da Silva et al. (2014), with two emission bandpasses of width 0.1 nm centred on 589.592 nm and 588.995 nm, and two continuum bandpasses centred on 580.50 nm and 609.00 nm, with width 1.0 nm and 2.0 nm, respectively. B_l values are plotted in Figures 9 and 10 with 1σ error bars, and Hα and Na I doublet indices are shown with 3σ error bars for clarity.

For both stars we see a range of values in all activity measures, which is expected given the evolutionary states of these stars. TWA 25 shows variation in longitudinal magnetic field strength, $|B_l|$, between between 0.2 ± 5.9 G and 56 ± 7 G. Significant variation is also observed in the Hα indices, and to a lesser extent in the Na I doublet indices. Across all observations of TWA 25, B_l measurements at a given observed phase have a small dispersion, indicating that the large scale magnetic field is stable over the timespan of our observations. This is also the case for the Hα and Na I doublet indices, indicating that these changes are associated with particular features in the stellar surface, and that these features are largely stable over the timespan of ur observations.

TWA 7 also displays variation in the longitudinal magnetic field, with $|B_l|$ values ranging between 4 ± 10 G and 50 ± 8 G. At a given observed phase B_l values are consistent, indicating that the large-scale field is stable over the our observations. The Hα and Na I doublet indices, however, both display large dispersion in value at a given phase, and so are not correlated to a given surface feature.

We analyse the periodicity of our B_l, Hα and Na I doublet indices for both stars with a Generalised Lomb Scargle periodogram (Zechmeister & Kürster 2009), using the PyAstronomy[2] package. These are shown in Figure 11 for TWA 25 and in Figure 12 for TWA 7. Included in these figures are vertical dotted lines indicating the stellar rotation period and fractions of the rotation period, as well as horizontal dashed lines indicating false alarm probability (FAP) levels. These FAP values are calculated in the PyAstronomy program as per Equation 24 of (Zechmeister & Kürster 2009).

The periodograms of B_l, Hα and Na I doublet indices for TWA 25 all show peaks around the stellar rational period. For the Hα and the Na I doublet this is the second highest peak (the highest is around the 1/4 rotation period), but is still detectable above a FAP of 0.001. For the B_l values however, the peak at the rotation period in small. Instead, the highest peak in B_l is at 1/2 the rotation period, with the second highest peak at 1/3 the rotation period. All periodograms show a spike around 1, as this is the cadence of observations for TWA 25.

For TWA 7, the periodogram of B_l has the highest peak at the stellar rotation period with detectability at the FAP level of 0.01, and the second highest peak at 1/4 of the rotation period. The Hα and Na I doublet indices, however, do not have any peaks of significant power associated with the stellar rotation period. Instead, their highest peaks are around the cadence of observations of 1 day.

This shown that while activity indices like Na I and Hα can be useful in determining the stellar rotation period (e.g. TWA 25), this is not always the case (e.g. TWA 7). Thus, monitoring of the longitudinal magnetic field can provide an alternative method of measuring stellar rotation, independent of the behaviour of the chromospheric activity indices.

[2] https://github.com/sczesla/PyAstronomy

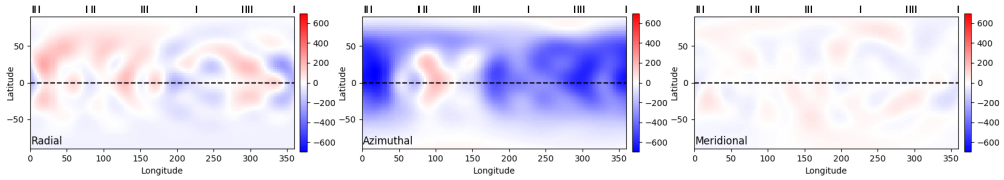

Figure 7. ZDI reconstructed large-scale radial (left), azimuthal (centre) and meridional (right) magnetic field maps of TWA 25 from the Stokes V profile in figure 5. These results a show strong azimuthal field compared to the radial and meridional field components. The radial field is quite complex and non-axisymmetric, with > 40% for the poloidal field energy contained in octopolar or higher order components, and ∼ 95% poloidal field energy in non-axisymmetric components.

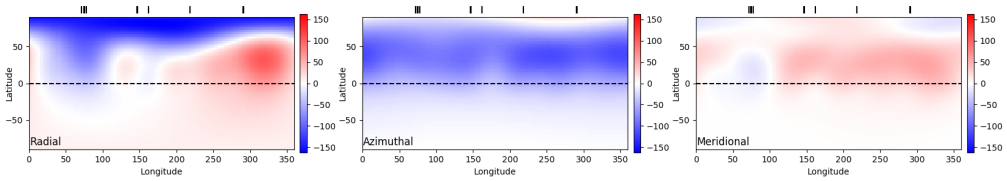

Figure 8. ZDI reconstructed large-scale radial (left), azimuthal (centre) and meridional (right) magnetic field maps of TWA 7 from the Stokes V profile in figure 6. These results show a stronger azimuthal field than either the radial or meridional components. The poloidal field is quite simple with > 75% of the poloidal field energy in dipolar or quadrupolar components, and predominantly non-axisymmetry, with ∼ 51% of the poloidal field energy in non-axisymmetric components

6 RADIAL VELOCITIES

We analyse the radial velocities of TWA 25 by measuring the first order moment of the Stokes I profiles in the heliocentric rest frame. The uncertainty on these values are calculated as in Butler et al. (1996). These RV values are shown as pink diamonds in Figure 13. We then use the surface brightness fit from Doppler Imaging to filter out the activity-induced RV signal, by measuring the RVs of our DI fits (shown as orange line in Figure 13), and subtracting them from the radial velocities of our observations. The resulting residuals (shown as purple circles in Figure 13), as per the method of Donati et al. (2015). In doing this we reduce the RMS of the radial velocity variation from 495m s^{-1}to 37m s^{-1}, in line with the mean uncertainty of 39m s^{-1}. The detection limit was determined by adding an artificial Keplerian signal to the data, then attempting to recover it via a generalised Lomb-Scargle periodogram (Zechmeister & Kürster 2009). This injection-recovery approach is identical to that used in related exoplanet detection-efficiency studies (e.g. Wittenmyer et al. 2006, 2016; Wittenmyer & Marshall 2015). Given that the velocity data only span 19 days, we only test periods $P < 10$ days, corresponding to a semimajor axis of $a = 0.08$ au. We further assume that planets in such short periods would be tidally circularised, and so we test for circular orbits only. The results indicate that in general, we can rule out planets at the 99% confidence level with $M_p \sin i \gtrsim 0.7$ M_{Jup}in close orbits around TWA 25.

We are unable to perform the same filtering process for TWA 7, as the Stokes I LSD profiles are too narrow to be suitable for DI. Because of this, we instead measure the radial velocities using an alternate method better suited to precision radial velocity measurements. We take the HARPS DRS pipeline reduced spectra, resample them to a uniform velocity step of 300 m s^{-1}, combine them to make a mean spectrum, and then cross-correlate each observation with the mean spectrum. This provides a cross-correlation function (CCF) for each observation. CCFs have much smaller uncertainties and provide more precise radial velocity measurement than LSD profiles, but do not preserve the information about line shape, particularly in the wings of the line and hence are not used for tomographic modelling. The radial velocity of each CCF is determined by fitting a Generalised Gaussian Distribution. This method is similar to that of Baranne et al. (1996) and Pepe et al. (2002), except for the use of the mean spectrum here as the template for creating the CCFs.

We see a variation in the radial velocities that is very well fit with a sinusoid with period 4.98 days, and a semi amplitude of 163m s^{-1}. These are plotted in the upper panel of Figure 14. To investigate this RV variation further, we calculate the radial velocities of 29 HARPS observation of TWA 7 found in the ESO archive taken between February 2005 and February 2008 (observing programs 074.C-0037, 076.C-0010, 077.C-0012 and 079.C-0046). These are plotted in Figure 15. They show a very similar period of 5.014 days, but with a lower amplitude and greater dispersion. The differences in the fits to the 2017 data and the 2005 2008 data suggest that the radial velocity variations are more likely due to surface activity then the presence of a planet, despite the very good sinusoidal fit to the 2017 velocities. This conclusion is further supported by the close anti-correlation of the longitudinal magnetic field variations and the radial velocities, further indicating role of activity in the radial velocity signal.

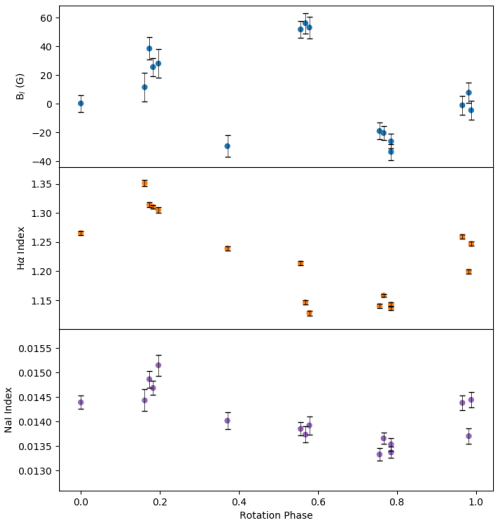

Figure 9. Plots of longitudinal magnetic field measurement (top), Hα indices (middle) and Na I doublet indices (bottom) for TWA 25.

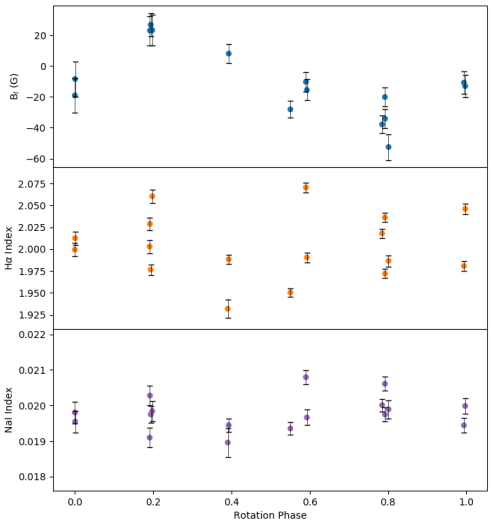

Figure 10. Plots of longitudinal magnetic field measurement (top), Hα indices (middle) and Na I doublet indices (bottom) for TWA 7.

7 SUMMARY AND DISCUSSION

This paper presents detailed analysis of high resolution spectropolarimetric data of 2 M-type wTTS, TWA 25 and TWA 7. Observation were taken between 12 to 31 March 2017, with a total of 16 observations for TWA 25, and 15 observations for TWA 7. Using the techniques of DI and ZDI, we reconstruct the large-scale surface brightness for TWA 25, and the large-scale magnetic fields for TWA 25 and TWA 7. In addition to this, we probe the stellar magnetic activity as a function of rotation, by measuring the line of sight magnetic field, H alpha emission and core emission in the Na I doublet. We examine the radial velocity variations of both stars, and filter the activity jitter from the radial velocity curve using the brightness information from DI.

7.1 Dynamos in M-type PMS stars

The magnetic field reconstructions for TWA 25 and TWA 7 add to the diversity of magnetic field morphologies both in the magnetically observed population of wTTS and in the wider PMS population. The strong azimuthal fields of TWA 25 and TWA 7 add to the range of magnetic fields seen in wTTSs. TWA 25 and TWA 7 are plotted in Figure 16 along side the rest of the MaTYSSE sample (labeled and outlined in black), and the MaPP cTTS sample. WTTS display a larger diversity of magnetic field morphologies compared to cTTSs. While the large scale fields of cTTS appear to show a dependence on the internal structure, the magnetic fields of wTTS display no such trends Gregory et al. (2012). This

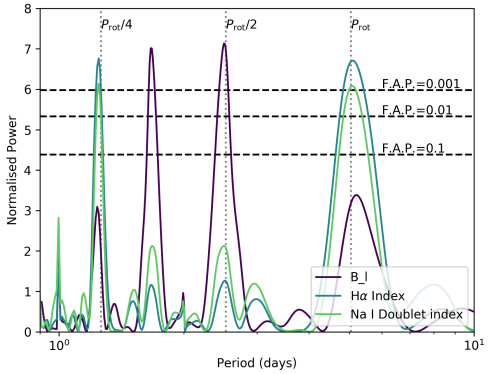

Figure 11. Periodogram of B_l, Hα indices and Na I Doublet indices for TWA 25.

perhaps indicates that accretion may have an influence on large-scale magnetic field. However, the dynamo models of Emeriau-Viard & Brun (2017) produce results that are consistent with cTTS population morphologies, despite no inclusion of accretion processes in their simulations, indicating accretion may not be the reason for the difference in the field morphologies.

Instead, the different dynamo fields may be related to

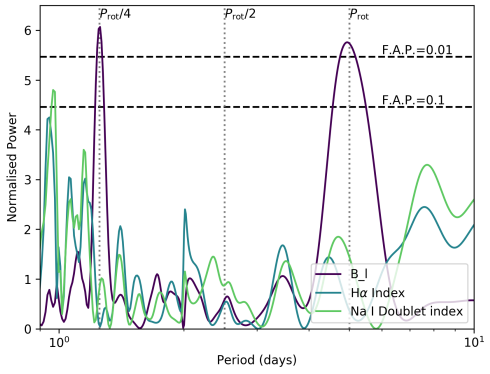

Figure 12. Periodogram of B_l, Hα indices and Na I Doublet indices for TWA 7.

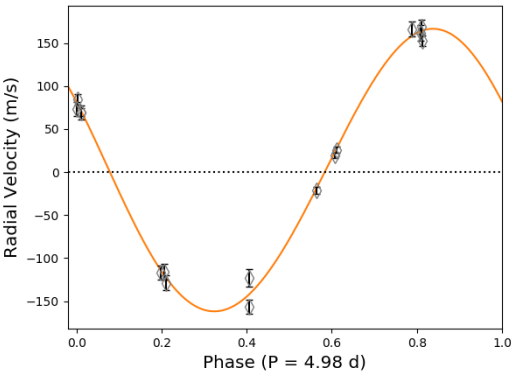

Figure 14. Radial velocities of TWA 7 (grey points), with RMS of 113m s^{-1}and mean uncertainty of 7 m s^{-1}, fitted with a sinusoid (orange line) with period 4.98 days and semi amplitude of 163 m s^{-1}. These points are anti-correlated with the variations in longitudinal magnetic field (top panel of Figure 10).

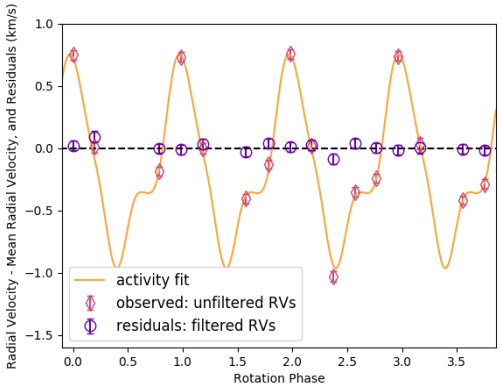

Figure 13. Radial Velocities of TWA 25. Pink diamonds are the measured radial velocities of the LSD profiles (black lines in Figure 2), the orange line is the radial velocity contribution from the surface brightness inhomogeneities, as measured from our fit to the surface brightness (red line in Figure 2), and the purple circles are the activity filtered radial velocities, calculated by subtracting the brightness fit (orange line) from the measured radial velocity (pink diamonds). The RMS in the raw radial velocities is 495 m s^{-1}, which is reduced to 37 m s^{-1}after filtering, which is smaller than the mean error of 39m s^{-1}.

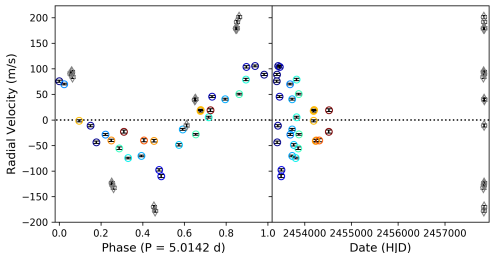

Figure 15. Radial Velocities of TWA 7 from archival and current data, plotted as a function of phase with respect to the best fit period of the whole data set of 5.0142 days (left), and as a function of Heliocentric Julian Date (right). Data from the current paper are in grey, and archival data are coloured according to phase. Archival data show a lower amplitude radial velocity variation, with much more scatter at a given phase. The amplitude of the archival RVs appear to decrease with time, but are too poorly sampled for this to be definitive.

the initial formation conditions that also determine the disc-clearing timescales. The MaTYSSE wTTSs have been selected to overlap in age and evolutionary state with the MaPP cTTS sample, so the selected wTTS sample have cleared their discs far more rapidly than the cTTS, indicating different conditions in their formation and early evolution. It could be this difference, rather than the presence of accretion, that explains the observed differences in their magnetic field morphologies.

For the very low mass, fully convective T Tauri stars, the weaker, predominantly toroidal fields may be explained by the 'bistability' phenomenon found in low mass, fully convective M dwarfs, where stars of the same broad parameters can display either strong, poloidal and axisymmetric field, or weak, toroidal, and non-axisymmetric fields (Morin et al. 2011). Dynamo simulations by Simitev & Busse (2009) have shown the same phenomena; different field configurations are seen for stars with the same parameters, but differing initial conditions.

We are unable to draw any definitive conclusions here, as the observed sample of T Tauri stars is still quite small. However, the rise of new infrared high-resolution spectropolarimeters, such as SpIROU on CFHT (Donati et al. 2018) and CRIRES+ on the ESO VLT(Follert et al. 2014),

presents exciting opportunities in the study of T Tauri star magnetic fields, and particularly for the M-type stars in this class. These new instruments will provide useful insights into these cooler stars in greater numbers that is possible at optical wavelengths.

7.2 Radial velocities and active stars

TWA 25 and TWA 7 both exhibit large, periodic variations in their radial velocities. For TWA 25, surface spot and plage features create large distortions in the spectral absorption line, which we are able to characterise using DI, and filter their effect from our RV observations, reducing the RMS of our RVS from 495 $\mathrm{m\,s^{-1}}$ to 37 $\mathrm{m\,s^{-1}}$, which is in line with our mean uncertainty of 39 $\mathrm{m\,s^{-1}}$. Given the amplitude of these filtered radial velocities, the period and sampling of observations, and the uncertainties on our radial velocity measurements, we can rule out a planet with $\mathrm{M}_p \sin i$ greater than 0.7 Jupiter masses, orbiting closer than 0.08 au.

TWA 7 appears to be another example of a 'false positive' planet signal in the radial velocities of an active stars. It shows large radial velocity variations without obvious line distortion. At face value it is easy to assume that such a motion could be caused by a planet, and the lack of periodicity in activity indices and small amplitudes in line bisectors compared with the RV amplitude supports this. However, given the circular polarisation information in our observations that traces the variations in longitudinal magnetic field, we can infer that this radial velocity signal is likely caused by stellar activity. It is reminiscent of the case of TWA Hya, where a hot Jupiter was hypothesised to be orbiting on the same period as the stellar rotation period, but this signal was later shown to be caused by a dark surface feature (Donati et al. 2011a). Further to the correlation of the longitudinal field signal with the radial velocities, the lower amplitude and dispersion of radial velocities in the archival data of TWA 7, and indicates that, at the very least, a planetary signal is too difficult to disentangle from the behaviour of the star. Nevertheless, this is still an intriguing RV signal, and further observations are warranted to truly characterise this behaviour in the stellar spectrum.

Given the lack of exoplanet detections for both stars, we can adjust the observed occurrence rate of hot Jupiters around wTTSs to from 1 in 5 to 1 in 6, as measured by the MaTYSSE sample. This is still dramatically higher than the MS occurrence rate of 1%, but the MaTYSSE sample is still very small. A lager sample is needed to estimate the true occurrence rate. The commissioning of new high resolution spectropolarimeters mentioned above will greatly help with this.

ACKNOWLEDGEMENTS

This work has made use of the VALD database, operated at Uppsala University, the Institute of Astronomy RAS in Moscow, and the University of Vienna. This work has made use of data from the European Space Agency (ESA) mission *Gaia* (http://www.cosmos.esa.int/gaia), processed by the *Gaia* Data Processing and Analysis Consortium (DPAC, http://www.cosmos.esa.int/web/gaia/dpac/consortium). Funding for the DPAC has been provided by national institutions, in particular the institutions participating in the *Gaia* Multilateral Agreement. We also warmly thank the IDEX initiative at Université Férale Toulouse Midi-Pyrt'ees (UFTMiP) for funding the STEPS collaboration programme between IRAP/OMP and ESO and for allocating a Chaire d'Attractivité to GAJH, allowing her to regularly visit Toulouse to work on MaTYSSE data. This research is supported by USQ's Strategic Research Initiative programme.

REFERENCES

Ammons S. M., Robinson S. E., Strader J., Laughlin G., Fischer D., Wolf A., 2006, ApJ, 638, 1004
Baraffe I., Homeier D., Allard F., Chabrier G., 2015, A&A, 577, A42
Baranne A., et al., 1996, Astronomy & Astrophysics Supplement Series, 119, 373
Butler R. P., Marcy G. W., Williams E., McCarthy C., Dosanjh P., Vogt S. S., 1996, PASP, 108, 500
Choquet É., et al., 2016, The Astrophysical Journal, 817, L2
Collier Cameron A., 1997, MNRAS, 287, 556
Donati J. F., Semel M., Carter B. D., Rees D. E., Collier Cameron A., 1997, MNRAS, 291, 658
Donati J. F., et al., 2006, MNRAS, 370, 629
Donati J.-F., et al., 2007, MNRAS, 380, 1297
Donati J.-F., et al., 2008, MNRAS, 386, 1234
Donati J. F., et al., 2010a, Monthly Notices of the Royal Astronomical Society, 402, 1426
Donati J.-F., et al., 2010b, MNRAS, 409, 1347
Donati J.-F., et al., 2011a, MNRAS, 417, 1747
Donati J. F., et al., 2011b, Monthly Notices of the Royal Astronomical Society, 417, 472
Donati J.-F., et al., 2012, Mon. Not. R. Astron. Soc, 425, 2948
Donati J. F., et al., 2013, Monthly Notices of the Royal Astronomical Society, 436, 881
Donati J. F., et al., 2014, Monthly Notices of the Royal Astronomical Society, 444, 3220
Donati J. F., et al., 2015, MNRAS, 453, 3706
Donati J.-F., et al., 2018, SPIRou: A nIR Spectropolarimeter/High-precision Velocimeter for the CFHT. Springer International Publishing, Cham, pp 1–27, doi:10.1007/978-3-319-30648-3_107-1, https://doi.org/10.1007/978-3-319-30648-3_107-1
Emeriau-Viard C., Brun A. S., 2017, The Astrophysical Journal, 846, 8
Follert R., et al., 2014, in Ground-based and Airborne Instrumentation for Astronomy V. p. 914719, doi:10.1117/12.2054197
Gaia Collaboration et al., 2016, A&A, 595, A1
Gaia Collaboration Brown A. G. A., Vallenari A., Prusti T., de Bruijne J. H. J., Babusiaux C., Bailer-Jones C. A. L., 2018, preprint, p. arXiv:1804.09365 (arXiv:1804.09365)
Gaidos E., et al., 2014, MNRAS, 443, 2561
Gomes da Silva J., Santos N. C., Boisse I., Dumusque X., Lovis C., 2014, Astronomy & Astrophysics, 566, A66
Gregory S. G., Donati J.-F., Morin J., Hussain G. A. J., Mayne N. J., Hillenbrand L. A., Jardine M., 2012, apj, 755, 97
Grunhut J. H., et al., 2013, Monthly Notices of the Royal Astronomical Society, 428, 1686
Hébrard É. M., Donati J. F., Delfosse X., Morin J., Moutou C., Boisse I., 2016, MNRAS, 461, 1465
Henden A. A., Templeton M., Terrell D., Smith T. C., Levine S., Welch D., 2016, VizieR Online Data Catalog, 2336
Hill C. A., Carmona A., Donati J. F., Hussain G. A. J., Gregory

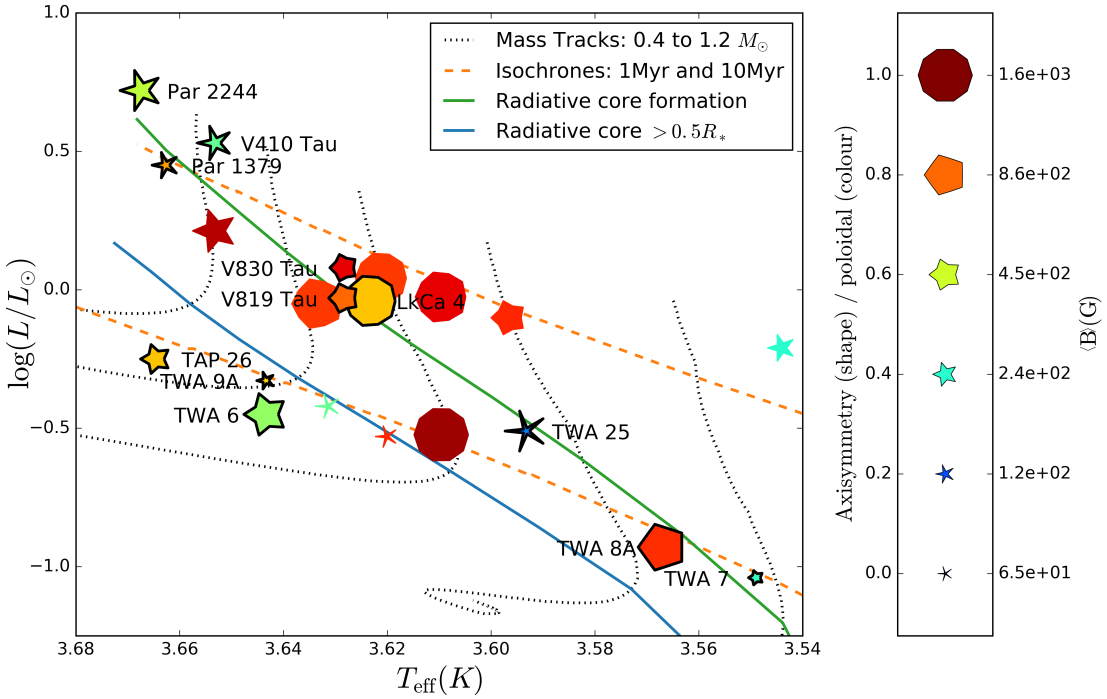

Figure 16. A Hertzsprung-Russell Diagram showing the updated MaTYSSE sample of WTTSs (outlined in black; additional data from Donati et al. 2014, 2015; Yu et al. 2017; Hill et al. 2017; Nicholson et al. 2018, Hill et al. In Prep.), and the MaPP sample of CTTSs (data from Donati et al. 2007, 2008; Donati et al. 2010a; Donati et al. 2010b, 2011a; Donati et al. 2011b, 2012, 2013). The size of each point represents the mean magnetic field strength, the colour indicates the percentage of magnetic field energy in poloidal components, and the shape indicates the percentage of poloidal field energy in axisymmetric components. The black dotted lines show mass tracks from the Baraffe et al. (2015) PMS evolution models, as well as isochrones as orange dashed lines. The boundary in evolution where a radiative core begins to form in indicated by the solid green line, and where the radiative core becomes greater than half the radius of the star is given by the solid blue line.

S. G., Alencar S. H. P., Bouvier J., The Matysse Collaboration 2017, MNRAS, 472, 1716
Hussain G. A. J., et al., 2009, MNRAS, 398, 189
López-Martínez F., Gómez de Castro A. I., 2015, MNRAS, 448, 484
Marsden S. C., et al., 2014, MNRAS, 444, 3517
McDonald I., Zijlstra A. A., Watson R. A., 2017, MNRAS, 471, 770
Mentuch E., Brandeker A., van Kerkwijk M., Jayawardhana R., Hauschildt P., 2008, ApJ, 689, 1127
Morin J., Delfosse X., Donati J.-F., Dormy E., Forveille T., Jardine M. M., Petit P., Schrinner M., 2011, in Alecian G., Belkacem K., Samadi R., Valls-Gabaud D., eds, SF2A-2011: Proceedings of the Annual meeting of the French Society of Astronomy and Astrophysics. pp 503–508 (arXiv:1208.3341)
Nicholson B. A., Hussain G. A. J., Donati J.-F., Folsom C. P., Mengel M., Carter B. D., Wright D., 2018, Monthly Notices of the Royal Astronomical Society, 480, 1754
Olofsson J., et al., 2018, preprint, (arXiv:1804.01929)
Pecaut M. J., Mamajek E. E., 2013, The Astrophysical Journal Supplement Series, 208, 9
Pepe F., Mayor M., Galland F., Naef D., Queloz D., Santos N. C., Udry S., Burnet M., 2002, Astronomy & Astrophysics, 388, 632
Ryabchikova T., Piskunov N., Kurucz R. L., Stempels H. C., Heiter U., Pakhomov Y., Barklem P. S., 2015, Phys. Scr., 90, 054005
Semel M., 1989, A&A, 225, 456
Simitev R. D., Busse F. H., 2009, EPL (Europhysics Letters), 85, 19001
Song I., Zuckerman B., Bessell M. S., 2003, The Astrophysical Journal, 599, 342
Webb R. A., Zuckerman B., Platais I., Patience J., White R. J., Schwartz M. J., McCarthy C., 1999, The Astrophysical Journal, 512, L63
Wittenmyer R. A., Marshall J. P., 2015, AJ, 149, 86
Wittenmyer R. A., Endl M., Cochran W. D., Hatzes A. P., Walker G. A. H., Yang S. L. S., Paulson D. B., 2006, AJ, 132, 177
Wittenmyer R. A., et al., 2016, ApJ, 819, 28
Yang H., Johns-Krull C. M., Valenti J. A., 2008, The Astronomical Journal, 136, 2286
Yu L., et al., 2017, MNRAS, 467, 1342
Zechmeister M., Kürster M., 2009, A&A, 496, 577
da Silva L., Torres C. A. O., de La Reza R., Quast G. R., Melo C. H. F., Sterzik M. F., 2009, A&A, 508, 833

This paper has been typeset from a TEX/LATEX file prepared by the author.

4

Temporal variability of the wind from the star τ Boötis

Published in the Monthly Notices of the Royal Astronomical Society, 2016, Volume 459, pp.1907-1915.

Monthly Notices
of the
ROYAL ASTRONOMICAL SOCIETY

MNRAS **459,** 1907–1915 (2016)
Advance Access publication 2016 March 30

doi:10.1093/mnras/stw731

Temporal variability of the wind from the star τ Boötis

B. A. Nicholson,[1,2★] A. A. Vidotto,[3,4] M. Mengel,[1] L. Brookshaw,[1] B. Carter,[1] P. Petit,[5,6] S. C. Marsden,[1] S. V. Jeffers,[7] R. Fares[8] and the BCool Collaboration

[1]*Computational Engineering and Science Research Centre, University of Southern Queensland, Toowoomba, Australia*
[2]*European Southern Observatory, Karl Schwarzschild Str. 2, D-85748 Garching, Germany*
[3]*Observatoire de l'Université de Genève, Chemin des Maillettes 51, Versoix CH-1290, Switzerland*
[4]*School of Physics, Trinity College Dublin, The University of Dublin, Dublin-2, Ireland*
[5]*CNRS, Institut de Recherche en Astrophysique et Planétologie, 14 Avenue Edouard Belin, F-31400 Toulouse, France*
[6]*Université de Toulouse, UPS-OMP, Institut de Recherche en Astrophysique et Planétologie, Toulouse, France*
[7]*Institut für Astrophysik, Universität Göttingen, Friedrich Hund Platz 1, D-37077 Göttingen, Germany*
[8]*INAF - Osservatorio Astrofisico di Catania, Via Santa Sofia, 78, I-95123 Catania, Italy*

Accepted 2016 March 24. Received 2016 March 24; in original form 2016 January 14

ABSTRACT

We present new wind models for τ Boötis (τ Boo), a hot-Jupiter-host-star whose observable magnetic cycles makes it a uniquely useful target for our goal of monitoring the temporal variability of stellar winds and their exoplanetary impacts. Using spectropolarimetric observations from May 2009 to January 2015, the most extensive information of this type yet available, to reconstruct the stellar magnetic field, we produce multiple 3D magnetohydrodynamic stellar wind models. Our results show that characteristic changes in the large-scale magnetic field as the star undergoes magnetic cycles produce changes in the wind properties, both globally and locally at the position of the orbiting planet. Whilst the mass loss rate of the star varies by only a minimal amount (∼4 per cent), the rates of angular momentum loss and associated spin-down time-scales are seen to vary widely (up to ∼140 per cent), findings consistent with and extending previous research. In addition, we find that temporal variation in the global wind is governed mainly by changes in total magnetic flux rather than changes in wind plasma properties. The magnetic pressure varies with time and location and dominates the stellar wind pressure at the planetary orbit. By assuming a Jovian planetary magnetic field for τ Boo b, we nevertheless conclude that the planetary magnetosphere can remain stable in size for all observed stellar cycle epochs, despite significant changes in the stellar field and the resulting local space weather environment.

Key words: MHD – methods: numerical – stars: individual: τ Boötis – stars: magnetic field – stars: winds, outflows.

1 INTRODUCTION

The study of stellar winds gives insight into the evolution of stars and the planets that orbit them. The wind affects the stellar rotation rate through mass loss and magnetic braking (Schatzman 1962; Weber & Davis 1967; Bouvier 2013), and can also impact the atmospheres of orbiting planets (Adams 2011; Lammer et al. 2012), with potential implications on planet habitability (Horner & Jones 2010; Vidotto et al. 2013). An example of this impact is seen in our own Solar system with the stripping of Mars' atmosphere by the young Sun (Lundin, Lammer & Ribas 2007). However, studying stellar winds is problematic, as winds of stars like our Sun are too diffuse to observe directly (Wood, Linsky & Güdel 2015). Investigation of these stars therefore requires a combination of observation and magnetohydrodynamic (MHD) simulation in order to estimate the properties of these winds.

The star τ Boötis (τ Boo, spectral type F7V) is an ideal candidate for a study of the temporal variability of stellar winds, and their potential impacts on orbiting planets. It is the only star to date, other than our Sun, observed to have a magnetic field cycle, with multiple field reversals observed (Catala et al. 2007; Donati et al. 2008; Fares et al. 2009; Fares et al. 2013; Mengel et al. 2016). These observations reveal that the star has a magnetic cyclic period estimated to be a rapid 740 d (Fares et al. 2013). The availability of multiple epochs of magnetic field observations allows us to make observationally informed MHD models of τ Boo's wind, such as those detailed by Vidotto et al. (2012) (4 epochs observed between June 2006 and July 2008).

In this paper, we present an additional eight MHD simulations of the winds of τ Boo from magnetic field observations taken between

★ E-mail: belinda.nicholson@usq.edu.au

© 2016 The Authors
Published by Oxford University Press on behalf of the Royal Astronomical Society

Downloaded from http://mnras.oxfordjournals.org/ at University of Southern Queensland on May 3, 2016

May 2009 and January 2015. Our aim is to examine the changes in the wind behaviour due to the variations in the magnetic field over the observed epochs, which include multiple polarity reversals, and to demonstrate how these changes could impact the planet τ Boo b.

In Section 2, we detail the wind model and magnetic field input. The results of our simulations are presented in two parts: Section 3 presents the global wind properties over the eight epochs, and in Section 4 we investigate the properties of the wind around τ Boo b and the potential impact of the wind on the planet. We discuss these results in Section 5 and make conclusions based on our findings in Section 6.

2 STELLAR WIND MODEL

2.1 The BATS-R-US code

The stellar wind model used here is the same as used in Vidotto et al. (2012), but with higher resolution (as in Vidotto et al. 2014). For simulating the winds we use the BATS-R-US code (Powell et al. 1999; Tóth et al. 2012); a three-dimensional code that solves the ideal MHD equations

$$\frac{\partial \rho}{\partial t} + \nabla \cdot (\rho \mathbf{u}) = 0, \tag{1}$$

$$\frac{\partial (\rho \mathbf{u})}{\partial t} + \nabla \cdot \left[\rho \mathbf{u} \otimes \mathbf{u} + \left(P + \frac{B^2}{8\pi} \right) I - \frac{\mathbf{B} \otimes \mathbf{B}}{4\pi} \right] = \rho g, \tag{2}$$

$$\frac{\partial \mathbf{B}}{\partial t} + \nabla \cdot (\mathbf{u} \otimes \mathbf{B} - \mathbf{B}) = 0, \tag{3}$$

$$\frac{\partial \epsilon}{\partial t} + \nabla \cdot \left[\mathbf{u} \left(\epsilon + P + \frac{B^2}{8\pi} \right) - \frac{(\mathbf{u} \cdot \mathbf{B})\mathbf{B}}{4\pi} \right] = \rho \mathbf{g} \cdot \mathbf{u}, \tag{4}$$

where ρ and $\mathbf{u}$ are the plasma mass density and velocity, P is the gas pressure, $\mathbf{B}$ the magnetic flux, and $\mathbf{g}$ is the gravitational acceleration due to a star of mass M_*. The total energy density, ϵ, is given by

$$\epsilon = \frac{\rho u^2}{2} + \frac{P}{\gamma - 1} + \frac{B^2}{8\pi}. \tag{5}$$

The polytropic index, γ, is defined such that

$$P \propto \rho^{\gamma}. \tag{6}$$

Table 1 lists the stellar and wind values used for this simulation. The values of τ Boo's mass and radius, M_* and R_*, are taken from Takeda et al. (2007), and the rotation period, $t_{\rm rot}$, is taken from Fares et al. (2009). The wind mean particle mass, μ, is chosen on the assumption that the wind is only composed of protons and electrons. Each simulation is initialized using a polytropic wind solution and the magnetic field information from observations of a given epoch. It is then iterated forward around 30 000 time steps. This ensures that a steady state is achieved. Each simulation, therefore, is a snapshot of the wind at each epoch.

Table 1. Adopted stellar parameters for τ Boo used in the wind model.

M_* ($M_\odot$)	1.34
R_* ($R_\odot$)	1.46
Rotation period, $t_{\rm rot}$ (days)	3.0
Base wind temperature (K)	2×10^6
Base wind density (g cm^{-3})	8.36×10^{-16}
Wind mean particle mass, μ	0.5
Polytropic index, γ	1.1

2.2 Adopted surface magnetic fields

The BATS-R-US code uses a star's surface magnetic field as input to the inner boundary conditions. The magnetic field information for τ Boo comes from spectropolarimetric observations with the NARVAL instrument at Télescope Bernard Lyot in the Midi Pyrénées, accessed through the BCool collaboration (Marsden et al. 2014). The polarization information in the spectra observed at different stellar rotation phases are used to reconstruct the surface magnetic field topologies using Zeeman–Doppler imaging (ZDI, Donati & Landstreet 2009). The reconstruction of the magnetic field maps used in this work is presented in Mengel et al. (2016). The radial field topologies are of sole interest for the stellar wind modelling as the other, non-potential field components have been shown to have a negligible effect on the wind solution (Jardine et al. 2013).

Fig. 1 shows the reconstructed radial magnetic fields, in units of Gauss (G), for eight sets of observations (epochs): May 2009, January 2010, January 2011, May 2011, May 2013, December 2013, May 2014 and January 2015. The grey lines here are contours at 0 G. The first three of these epochs were published by Fares et al. (2013); however, for consistency the maps presented here are an updated version using the same methodology as used with the other five epochs, the details of which are presented in Mengel et al. (2016). Due to the inclination of the star, the area below -40° is not observable. The field in this area of the stellar surface is solved for by enforcing $\nabla \cdot \mathbf{B} = 0$. Vidotto et al. (2012) showed that choosing this constraint, versus explicitly forcing a symmetric or antisymmetric solution to the large-scale field topology has little impact on the wind solution, especially in the visible hemisphere.

Table 2 shows a summary of the global magnetic field properties over the observed epochs. The magnetic cycle phase is calculated based on a 740-day cycle found by Fares et al. (2013), with the cycle zero phase chosen to be 2453818 Heliocentric Julian Date (HJD) to align with the magnetic cycle zero-point of Vidotto et al. (2012). The complexity of the field topology can be quantified by examining the amounts of energy in the different set spherical harmonics that are used to describe the field (Donati et al. 2006). The modes of these coefficients where $l \leq 2$ give the dipolar and quadrupolar field configurations. The complexity of the large-scale field is quantified by the percentage of magnetic energy present in the modes where $l > 2$ over the total energy. A lower percentage indicates a simpler field configuration, whereas a higher percentage means that a larger amount of energy is present in more complicated, smaller scale features.

The field remains dominantly poloidal throughout all observations, with most of the magnetic energy being contained in more complex field components and the complexity varying from 45 per cent to 83 per cent over the cycle. The star is observed to undergo three polarity reversals, with two reversals assumed to have occurred between the May 2011 and May 2013 observations. The absolute surface radial magnetic flux (see Section 3.2) ranges from 1.53×10^{23} Maxwells (Mx) to a peak of 3.28×10^{23} Mx before the polarity reversal that was then seen in the May 2014 observations. This same peak and fall in magnetic flux is not observed in the previous polarity reversals probably due to the timing of the observation, and the length of time between observed epochs.

3 WIND SIMULATION RESULTS: GLOBAL WIND PROPERTIES

3.1 Magnetic field

The behaviour of the stellar wind is dependent on the geometry and strength of the global stellar magnetic field. Here we examine the

Downloaded from http://mnras.oxfordjournals.org/ at University of Southern Queensland on May 3, 2016

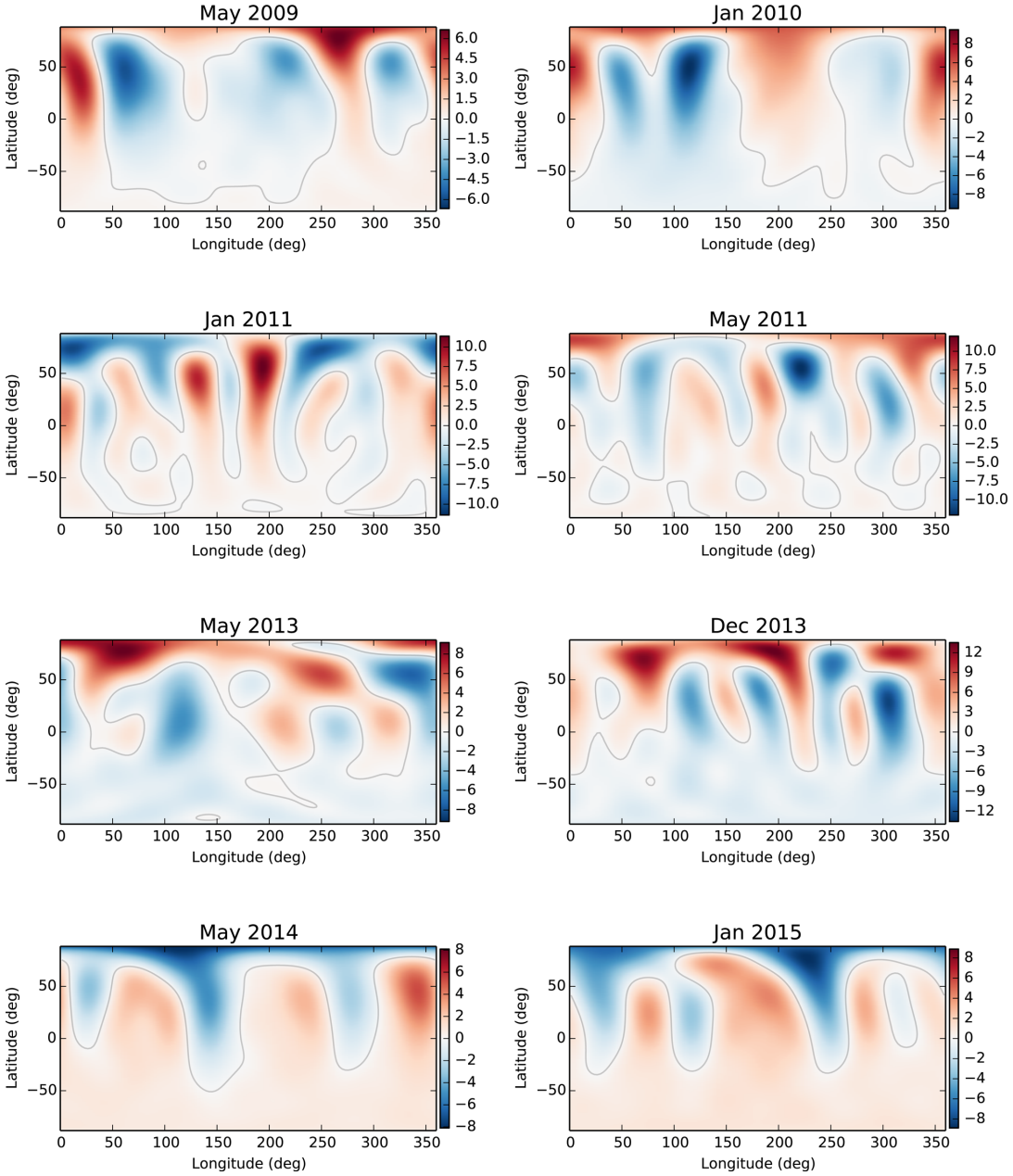

Figure 1. Radial magnetic field maps for the eight observed epochs, measured in Gauss (G), with the grey line indicating $B_r = 0$ G. The May 2009 to January 2011 maps come from Fares et al. (2013), and the May 2011 to January 2015 maps from Mengel et al. (2016). The Fares et al. epochs have been reanalysed for consistency with the Mengel et al. maps. The field remains dominantly poloidal across the eight observations, and three polarity reversals are observed. It is believed that two polarity reversals have occurred between May 2011 and May 2013.

behaviour of the wind at intervals of five months to one year, over a total period of five years and seven months. It is expected that the wind will vary little over the time it takes to observe one epoch (∼14 d; Vidotto et al. 2012).

As the magnetic field extends outward from the stellar surface, it will be influenced by the presence of the stellar wind. Fig. 2 shows the magnetic field lines (grey lines) outwards from the surface of the star. The colour contours on the surface represent radial magnetic

Downloaded from http://mnras.oxfordjournals.org/ at University of Southern Queensland on May 3, 2016

Table 2. Summary of the radial magnetic field polarity and complexity of τ Boo for observations from May 2009 to January 2015. The magnetic cycle period is taken to be 740 d from Fares et al. (2013), with the phase zero-point at 2453818 HJD.

Date	Magnetic cycle phase	Visible pole polarity	Radial field complexity (per cent of $l > 2$)
May 2009	0.57	Positive	77
Jan 2010	0.91	Positive	45
Jan 2011	0.38	Negative	73
May 2011	0.54	Positive	83
May 2013	0.51	Positive	62
Dec 2013	0.81	Positive	65
May 2014	0.02	Negative	58
Jan 2015	0.34	Negative	62

flux. The lines are seen to twist along the rotation axis (z-axis) of the star. The number of large closed loops is notable compared to similar plots produced by Vidotto et al. (2012), which is due to a difference in simulation resolution and different reconstruction process to create the magnetic maps. The impact of grid resolution on results is explored in more detail in Appendix A.

This proportion of open to closed magnetic flux can be quantified by examining magnetic flux at different points in the simulation. The unsigned radial flux, Π, is given by

$$\Pi = \oint_{S_R} |B_\mathrm{r}| dS_R, \tag{7}$$

where S_R is a spherical surface of radius R. The unsigned surface radial magnetic flux, Π_0, can be calculated from equation (7) at the surface $R = R_*$. At $R \geq 10R_*$ the magnetic flux is contained solely within open field lines, and equation (7) integrated over a sphere $S_{R\geq 10}$ in this region then represents the absolute open magnetic flux, Π_open. The fraction of open flux, f_open is then defined as

$$f_\mathrm{open} = \frac{\Pi_\mathrm{open}}{\Pi_0}. \tag{8}$$

These values are given in Table 3. The proportion of open to closed flux is seen to be low, with a majority of the flux from the surface being contained within closed field lines.

3.2 Derived wind properties

Quantities of interest to the study of stellar rotation evolution, such as mass loss, angular momentum loss and spin-down time-scale, can be calculated from the output of the wind simulation. Table 3 summarizes the properties of the wind derived from our simulation. The mass loss rate,

$$\dot{M} = \oint_{S_{R\geq 10}} \rho \mathbf{u} \cdot d\mathbf{S}_{R\geq 10}, \tag{9}$$

and angular momentum loss rate

$$\dot{J} = \oint_{S_{R\geq 10}} \left[\frac{-B_\phi B_\mathrm{r} \sqrt{x^2+y^2}}{4\pi} + u_\phi \rho u_\mathrm{r} \sqrt{x^2+y^2} \right] dS_{R\geq 10} \tag{10}$$

(Mestel 1999; Vidotto et al. 2014) are also evaluated over $S_{R\geq 10}$, where these quantities reach a constant value. The angular momentum loss is used to infer the time-scale of magnetic braking, τ, defined as $\tau = J/\dot{J}$, measured in Gyr, where J is the angular momentum of the star given by $J = (I_\mathrm{core} + I_\mathrm{envelope})\Omega_*$, with Ω_* being the stellar angular velocity. We estimate the spin-down time of τ Boo by using stellar evolution models to estimate the moment of inertia of the core, I_core, and convective envelope, I_envelope, separately. This spin-down time-scale, τ, is given by

$$\tau = \frac{2\pi(I_\mathrm{core} + I_\mathrm{envelope})}{t_\mathrm{rot}\dot{J}}. \tag{11}$$

Table 3 gives this these spin-down times using $I_\mathrm{core} = 1.05 \times 10^{54}$ g cm^2 and $I_\mathrm{envelope} = 4.53 \times 10^{51}$ g cm^2, calculated from the model of Baraffe et al. (1998) (Gallet, private communication).

The mass loss rates show little variation over the eight epochs, ranging between 2.29×10^{-12} and 2.38×10^{-12} M$_\odot$ yr^{-1}, approximately 100 times the Solar mass loss rate. This level of variation ($\sim$4 per cent) is in agreement with the epoch-to-epoch mass loss rate variability found by Vidotto et al. (2012) ($\sim$3 per cent).

We calculate a lower limit on the X-ray luminosity, as in Llama et al. (2013), assuming that the quiescent X-ray emission of the coronal wind is caused by free–free radiation. We find little variation ($\sim$2 per cent) over the observed epochs. This is in agreement with the previous wind model results of Vidotto et al. (2012), and the X-ray observations of τ Boo by Poppenhaeger, Günther & Schmitt (2012) and Poppenhaeger & Wolk (2014).

The angular momentum loss rate values are seen to vary by $\sim$140 per cent over the eight epochs, with a peak at December 2013, corresponding to a peak in the observed radial surface flux, Π_0, as do the spin-down time-scales, τ. Our values of spin-down time differ by 1 order of magnitude than those derived by Vidotto et al. (2012). This is due to different assumptions in the moment of inertia of the star (Vidotto et al. (2012) assumed that of a solid sphere, while we use a more sophisticated approach).

4 WIND ENVIRONMENT AROUND THE PLANET

4.1 Wind properties at τ Boo b

Since the planet τ Boo b is tidally locked to its star in a 1:1 resonance, the location of the planet with respect to the surface of the star does not change. The planet's orbit lies in the equatorial (x–y) plane of the star (Brogi et al. 2012) on the negative x-axis at $x = -6.8R_*$. Table 4 gives the properties of the environment surrounding the planet. The total pressure, P_tot, is the sum of the thermal, ram and magnetic pressures. The thermal pressure due to the wind, P, is an output of the simulation. The ram pressure, P_ram, is given by:

$$P_\mathrm{ram} = \rho |\Delta \mathbf{u}|^2 \tag{12}$$

where $|\Delta \mathbf{u}| = |\mathbf{u} - \mathbf{v_k}|$ is the relative velocity between the planet and the wind, with $\mathbf{v_k}$ being the planet's Keplerian velocity. The magnetic pressure, P_mag is given by:

$$P_\mathrm{mag} = \frac{|\mathbf{B}|^2}{8\pi}. \tag{13}$$

The variation in surface absolute magnetic flux shown in Table 3 is reflected in the variation in level of absolute magnetic flux, $|\mathbf{B}|$, at the position of the planet. In contrast to this, the wind velocity, $|\mathbf{u}|$, and particle density, Γ, vary only a small amount ($\sim$17 per cent and $\sim$14 per cent, respectively) over the observed epochs. The temperature, however, is seen to change by nearly approximately 46 per cent, and total pressure, P_tot, varies between maxima and minima by $\sim$94 per cent.

Fig. 3 shows the total, ram, magnetic and thermal pressure measurement for each observed epoch. The magnetic pressure varies by up to 48 per cent, whereas the ram and thermal pressures vary minimally ($\sim$5 per cent) over the eight epochs, indicating that

Downloaded from http://mnras.oxfordjournals.org/ at University of Southern Queensland on May 3, 2016

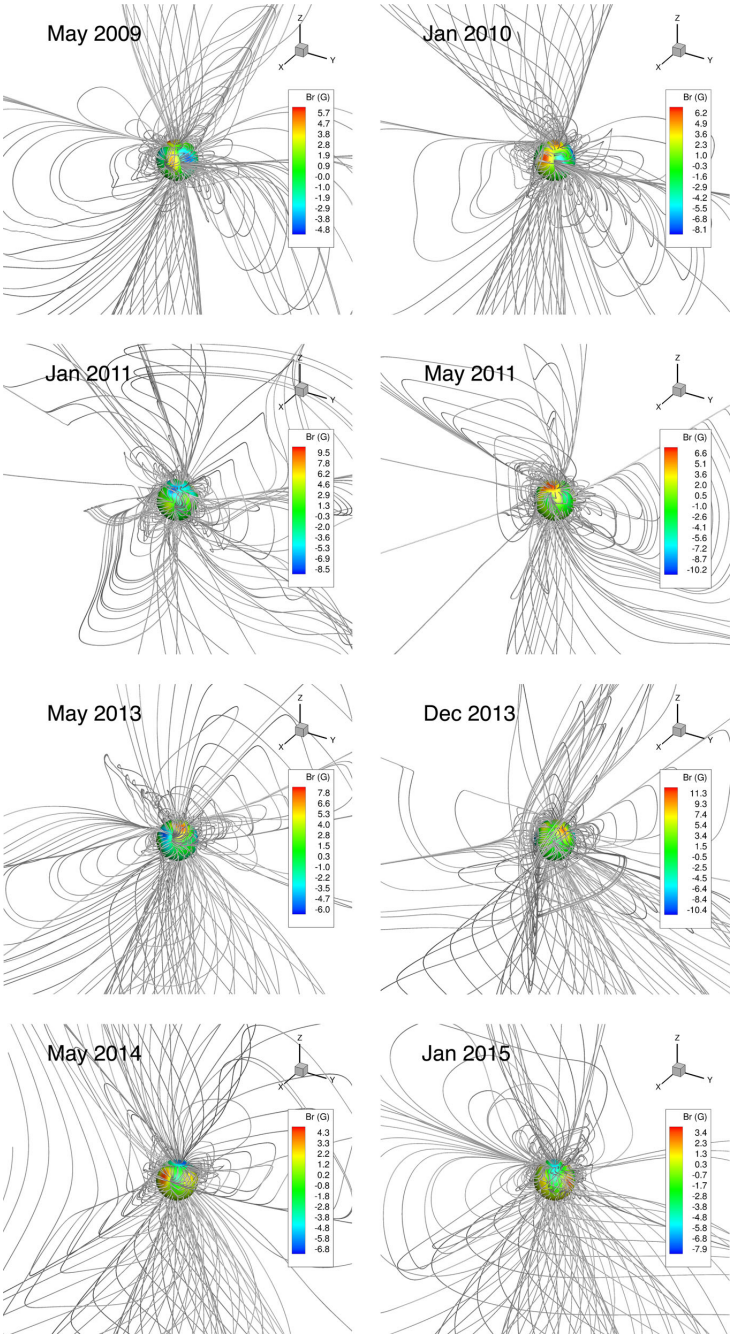

Figure 2. These plots show the simulation results of the large-scale magnetic field lines surrounding τ Boo. The sphere in the centre represents the stellar surface, with the colour contours indicating the radial magnetic field strength at the surface. The rotational axis of the star is along the z-axis, with the equator lying in the xy-plane. It can be seen that the field lines become twisted around the axis of rotation (z-axis) due to the presence of the wind.

Downloaded from http://mnras.oxfordjournals.org/ at University of Southern Queensland on May 3, 2016

Table 3. Summary of the simulated global wind properties of τ Boo based on observations from May 2009 to January 2015. The behaviour of the magnetic field is described by the unsigned surface flux, Π_0, the open flux beyond 10 stellar radii, $\Pi_{\rm open}$, and the ratio of these quantities, $f_{\rm open}$. These values indicate a significant variation in magnetic field behaviour between epochs. The stellar mass loss rate, $\dot{M}$, varies an insignificant amount over the observed epochs. The angular momentum loss rate, $\dot{J}$, however, and associated spin-down time-scales, τ, are observed to vary significantly over the eight epochs, correlating with the observed changes in the magnetic field.

Date	Π_0 (10^{22}Mx)	$\Pi_{\rm open}$ (10^{22}Mx)	$f_{\rm open}$	$\dot{M}$ (10^{-12}M$_\odot$ yr^{-1})	$\dot{J}$ (10^{32} erg)	τ (Gyr)
May 2009	15.3	4.5	0.29	2.34	1.3	6.5
Jan 2010	22.3	7.6	0.34	2.31	2.0	4.1
Jan 2011	22.3	5.6	0.25	2.34	1.6	5.0
May 2011	20.0	4.4	0.22	2.31	1.3	6.1
May 2013	21.4	7.1	0.33	2.29	1.7	4.7
Dec 2013	32.8	10.5	0.32	2.38	3.0	2.7
May 2014	18.7	8.0	0.43	2.30	1.6	5.2
Jan 2015	21.6	8.2	0.38	2.28	1.7	4.5

Table 4. Summary of the wind properties at the position of the planet τ Boo b. The variations in absolute magnetic field, $|\mathbf{B}|$, reflects the variation in the observed field. The influence of the magnetic flux changes are seen in variations of the total pressure experienced by the planet.

Date	$\lvert\mathbf{B}\rvert$ ($\times10^{-2}$ G)	$\lvert\mathbf{u}\rvert$ (km s^{-1})	T ($\times10^6$ K)	Γ ($\times10^6$ Particles cm^{-3})	$P_{\rm tot}$ ($\times10^{-3}$ dyn cm^{-2})
May 2009	0.41	209	1.05	1.46	0.81
Jan 2010	3.12	245	1.04	1.33	1.28
Jan 2011	3.65	229	1.07	1.43	1.44
May 2011	2.46	215	1.05	1.42	1.06
May 2013	3.06	226	1.05	1.40	1.19
Dec 2013	4.10	232	1.52	1.52	1.57
May 2014	2.82	216	1.11	1.41	1.16
Jan 2015	2.10	224	1.05	1.36	1.02

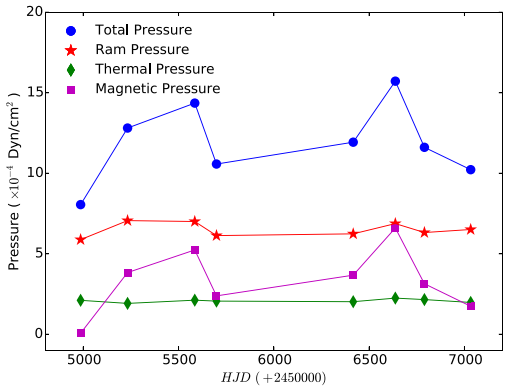

Figure 3. Pressure values at the orbit of the planet τ Boo b for each observed epoch. The total pressure is the sum of the ram, thermal and magnetic pressures. The ram and thermal pressures vary only slightly over the observed epochs, whereas the magnetic pressure varies more significantly. The lines between points are to guide the eye, and do not represent a fit to the data.

the changes in total pressure are due to changes in the magnetic pressure.

4.2 Planetary magnetospheric behaviour

The external pressure around the planet can be used to infer possible behaviours of the planet's magnetosphere. The ratio of the planetary magnetospheric radius, $R_{\rm m}$, to the planetary radius, $R_{\rm p}$, is derived from the equilibrium between the pressure from the wind and the outward force of the planetary magnetosphere. This can be written as

$$\frac{R_{\rm m}}{R_{\rm p}} = \left(\frac{(B_{\rm p}/2)^2}{8\pi P_{\rm tot}}\right)^{\frac{1}{6}} \quad (14)$$

(Vidotto et al. 2012),where $B_{\rm p}$ is the strength of the planetary magnetic field at the pole. Since there have been no measurements of the magnetic field strength of hot Jupiters to date, we have assumed a planetary magnetic field strength similar to that of Jupiter, which is a maximum of ∼14 G (Bagenal 1992). The values of $R_{\rm m}/R_{\rm p}$ evaluated over the eight epochs are shown in Table 5.

The behaviour of the planetary magnetosphere can also be described in terms of the auroral ring: the area around the poles of the planet over which the planetary magnetic flux is open, allowing the flow of particles to and from the planetary atmosphere. This can be described in terms of the percentage of the planet's surface area:

$$A_{\rm open} = (1 - \cos(\alpha)) \times 100, \quad (15)$$

where α is the auroral angular aperture, defined as

$$\alpha = \arcsin\left(\left(\frac{R_{\rm m}}{R_{\rm p}}\right)^{-\frac{1}{2}}\right) \quad (16)$$

Vidotto et al. (in preparation).

Despite notable changes in the total pressure exerted in the planet by the star, the planet's magnetosphere remains around 3.6 times the planet's radius, varying by only ∼3 per cent over the observed epochs. This is due to the relative insensitivity of $R_{\rm m}/R_{\rm p}$ to changes

Downloaded from http://mnras.oxfordjournals.org/ at University of Southern Queensland on May 3, 2016

Table 5. Values for the ratio of planet magnetospheric radius to planet radius, R_m/R_p, auroral aperture α and the percentage coverage of the polar cap, A_{open}, for the planet τ Boo b. These have been calculated assuming magnetic field strength at the pole of 14 G. Despite notable changes in the behaviour of the star's magnetic field and in the total pressure exerted on the planet by the stellar wind, these values remain quite stable over the observed epochs.

Date	R_m/R_p	α (degrees)	A_{open} (per cent)
May 2009	3.67	31.5	14.7
Jan 2010	3.57	31.9	15.1
Jan 2011	3.56	32.0	15.2
May 2011	3.64	31.6	14.8
May 2013	3.62	31.7	14.9
Dec 2013	3.55	32.1	15.3
May 2014	3.61	31.7	15.0
Jan 2015	3.62	31.7	14.9

in P_{tot} (due to the $-1/6$ power dependence). As with the planetary magnetospheric radius, there are minimal changes in the auroral aperture and polar surface area, which remain around 32° and 15 per cent, respectively. From this we can infer that despite considerable changes in the behaviour of τ Boo's magnetic field, τ Boo b's magnetosphere remains relatively stable.

5 DISCUSSION

5.1 Global wind properties

The wind simulations presented here are an advance on models that do not use observationally reconstructed magnetic fields as input, or that assume a simplified stellar magnetic field topology. The coronal base temperature and density are poorly constrained by observations, and are free parameters of our model. We chose a wind base temperature that is typical of stellar coronae, and the same base density as adopted in Vidotto et al. (2012). Out estimated mass loss rate ($\sim 2.3 \times 10^{-12} M_\odot$ yr^{-1}) is within the range of previous estimates of 1.67×10^{-12} (Stevens 2005) to $6.6 \times 10^{-12} M_\odot$ yr^{-1} (Cranmer & Saar 2011). Given that Sun's corona is adequately described by the adiabatic process given by equation (6), with the index $\gamma = 1.1$ (Van Doorsselaere et al. 2011), we assume the same for this star.

The behaviour of the angular momentum loss rate and associated spin-down time-scales found here agree with the predictions of Gallet & Bouvier (2013), who computed rotational evolution models based on wind-breaking laws derived for magnetised Solar-type stars. They find that the spin-down time-scales of stars at 1 Gyr old, which is the approximate age of τ Boo (Borsa et al. 2015), should converge to the length of a few Gyrs, the same as presented in the results here. This further strengthens our choice of model parameters.

The lifetime of a main-sequence star, τ_{MS}, with the mass of τ Boo (1.34 $M_\odot$) is expected to be ~4.8 Gyr ($\tau_{MS} = 10(M_*/M_\odot)^{-2.5}$). Given τ Boo's estimated age of 1 Gyr and our calculated mean spin-down time of ~4.9 Gyr, this implies that Tau Boo will remain a rapid rotator throughout its main sequence lifetime, provided that only the stellar wind is affecting its rotational evolution.

The changing stellar magnetic field polarity of the poles does not have an effect on the wind solution. This is because there is no preferred up or down orientation of the star, and the global wind properties are calculated as surface integrals around the star. Instead, it is the changing field strength as the star undergoes its reversals that drives changes in the wind behaviour.

Over the cycle there is a change in field complexity, and this is anti-correlated with on the fraction of open flux f_{open} (linear correlation coefficient $= -0.72$). As the field becomes more complex, the amount of flux contained in closed lines increases and the fraction of open flux decreases (see also Lang et al. 2012). No correlation is found, however, between changes in field complexity and changes, or lack there of, in the angular momentum or mass loss rates.

5.2 Wind–planet interaction

Wind simulations can give insight into the potential behaviour of the planetary magnetosphere in the presence of the stellar wind. Since there have been no observations of magnetic fields of exoplanets to date, assumptions must be made as to what magnetic field can be expected from τ Boo b. There is much discussion over the possible magnetic fields of exoplanets. It has been theorized that close in hot-Jupiters such as τ Boo b are thought to have a weaker magnetic field than similar planets further away from the host star due to the tidal locking slowing the planet's rotation, and hence reducing its magnetic field (Grießmeier et al. 2004). However, there are some studies that indicate that planetary rotation does not directly influence the strength of a planet's magnetic field (Christensen, Holzwarth & Reiners 2009), but plays a role in the field geometry (Zuluaga & Cuartas 2012). Given the uncertainty in hot-Jupiters magnetic fields and the similar nature of this planet to Jupiter, we have assumed a Jovian planetary magnetic field strength for this work. The resulting magnetosphere suggests the planet is protected from the stellar wind, despite large changes in the magnetic field and wind strengths over the cycle.

The minimum field strength required to sustain a magnetosphere above the surface of τ Boo b (i.e. $R_m > R_p$) can be estimated by examining the condition of the space weather environment during at the most extreme part of the magnetic cycle (i.e., when P_{tot} is at a maximum). This is calculated to be ~0.4 G. This does not mean, however, that the planet is protected at this point, as at this limit the Auroral aperture reaches 90 degrees, exposing 100 per cent of the planets surface area to particle inflow and outflow. If we were to call a planet 'protected' provided less than 25 per cent of its surface area was contained within the auroral aperture, then the minimum magnetic field strength to achieve this is ~4.7 G for the τ Boo system.

6 SUMMARY AND CONCLUSIONS

This study examines the variability in the wind behaviour of the star τ Boo over eight epochs from May 2009 to January 2015 - the most extensive monitoring of the wind behaviour of a single object to date (apart from the Sun). The winds are examined globally to study the star's rotational evolution, and locally around τ Boo b for the possible impacts the wind might have on the planet's magnetosphere.

Despite significant changes in the magnetic field behaviour, the mass loss rates do not significantly vary from epoch to epoch (~4 per cent), remaining around 2.3×10^{-12} $M_\odot$yr^{-1}. However, the angular momentum loss rate is observed to change considerably over the eight observations, ranging from 1.3×10^{32} to 3.0×10^{32} erg. These findings are consistent with angular momentum loss rates and associated spin-down time-scales predicted by stellar evolution models.

Downloaded from http://mnras.oxfordjournals.org/ at University of Southern Queensland on May 3, 2016

Examining the wind environment of the planet shows that variations in the absolute flux due to changes in the magnetic field behaviour of the star are reflected in changes in the local space weather of τ Boo b. Despite these changes, the magnetosphere from an assumed Jupiter-like planetary magnetic field is relatively invariant over the observed epochs, with the magnetospheric radius remaining around 3.6 times the size of the planetary radius.

ACKNOWLEDGEMENTS

This work was partly funded through the University of Southern Queensland Strategic Research Fund Starwinds Project. Some of the simulations presented in this paper were computed on the University of Southern Queensland's High Performance Computer. This research has made use of NASA's Astrophysics Data System. This work was carried out using the BATS-R-US tools developed at The University of Michigan Center for Space Environment Modeling (CSEM) and made available through the NASA Community Coordinated Modeling Center (CCMC). This work was supported by a grant from the Swiss National Supercomputing Centre (CSCS) under project ID s516. AAV acknowledges support from the Swiss National Science Foundation through an Ambizione Fellowship. Many thanks to Florian Gallet for providing the moment of inertia values for this work, and many thanks also to Colin Folsom for his help and advice.

REFERENCES

Adams F. C., 2011, ApJ, 730, 27
Bagenal F., 1992, Annu. Rev. Earth Planet. Sci., 20, 289
Baraffe I., Chabrier G., Allard F., Hauschildt P. H., 1998, A&A, 337, 403
Borsa F. et al., 2015, A&A, 578, A64
Bouvier J., 2013, EAS Publ. Ser., 62, 143
Brogi M., Snellen I. A. G., de Kok R. J., Albrecht S., Birkby J., de Mooij E. J. W., 2012, Nature, 486, 502
Catala C., Donati J. F., Shkolnik E., Bohlender D., Alecian E., 2007, MNRAS, 374, L42
Christensen U. R., Holzwarth V., Reiners A., 2009, Nature, 457, 167
Cranmer S. R., Saar S. H., 2011, ApJ, 741, 54
Donati J. F., Landstreet J. D., 2009, ARA&A, 47, 333
Donati J. F. et al., 2006, MNRAS, 370, 629
Donati J. F. et al., 2008, MNRAS, 385, 1179
Fares R. et al., 2009, MNRAS, 398, 1383
Fares R., Moutou C., Donati J.-F., Catala C., Shkolnik E. L., Jardine M. M., Cameron A. C., Deleuil M., 2013, MNRAS, 435, 1451
Gallet F., Bouvier J., 2013, A&A, 556, A36
Grießmeier J. M. et al., 2004, A&A, 425, 753
Horner J., Jones B. W., 2010, Int. J. Astrobiol., 9, 273
Jardine M., Vidotto A. A., van Ballegooijen A., Donati J. F., Morin J., Fares R., Gombosi T. I., 2013, MNRAS, 431, 528
Lammer H. et al., 2012, Earth Planets Space, 64, 179
Lang P., Jardine M., Donati J.-F., Morin J., Vidotto A., 2012, MNRAS, 424, 1077
Llama J., Vidotto A. A., Jardine M., Wood K., Fares R., Gombosi T. I., 2013, MNRAS, 436, 2179
Lundin R., Lammer H., Ribas I., 2007, Space Sci. Rev., 129, 245
Marsden S. C. et al., 2014, MNRAS, 444, 3517
Mengel M. W., Fares R., Marsden S. C., Carter B. D., Jeffers S. V., Folsom C. P., 2016, MNRAS, in press
Mestel L., 1999, Stellar Magnetism, Oxford Univ. Press, Oxford
Poppenhaeger K., Wolk S. J., 2014, A&A, 565, L1
Poppenhaeger K., Günther H. M., Schmitt J. H. M. M., 2012, Astron. Nachr., 333, 26
Powell K. G., Roe P. L., Linde T. J., Gombosi T. I., De Zeeuw D. L., 1999, J. Comput. Phys., 154, 284
Schatzman E., 1962, Annales d'Astrophysique, 25, 18
Stevens I. R., 2005, MNRAS, 356, 1053
Takeda G., Ford E. B., Sills A., Rasio F. A., Fischer D. A., Valenti J. A., 2007, ApJS, 168, 297
Tóth G. et al., 2012, J. Comput. Phys., 231, 870
Van Doorsselaere T., Wardle N., Del Zanna G., Jansari K., Verwichte E., Nakariakov V. M., 2011, ApJ, 727, L32
Vidotto A. A., Fares R., Jardine M., Donati J. F., Opher M., Moutou C., Catala C., Gombosi T. I., 2012, MNRAS, 423, 3285
Vidotto A. A., Jardine M., Morin J., Donati J. F., Lang P., Russell A. J. B., 2013, A&A, 557, 67
Vidotto A. A., Jardine M., Morin J., Donati J. F., Opher M., Gombosi T. I., 2014, MNRAS, 438, 1162
Weber E. J., Davis L., Jr, 1967, ApJ, 148, 217
Wood B. E., Linsky J. L., Güdel M., 2015, in Lammer H., Khodachenko M., eds, Astrophysics and Space Science Library Vol. 411, Astrophysics and Space Science Library. p. 19
Zuluaga J. I., Cuartas P. A., 2012, Icarus, 217, 88

APPENDIX A: SENSITIVITY OF RESULTS TO GRID REFINEMENT LEVEL

The design of the BATS-R-US code allows the simulation grid to be constructed so that areas of interest can be studied in greater detail by local grid refinement. This means that the region closest to the surface of the star that is changing the greatest can be simulated at a much finer resolution, but leaving the outer regions of the simulation with a much coarser grid structure to save on computing resources.

This section examines how the level of refinement of the grid, that is, the number of times the grid in the region close to the star is subdivided into smaller cells, affects the simulation outcomes. Using the May 2011 data, we examined $\dot{M}$, $\dot{J}$ and $f_{\rm open}$ (as calculated in Section 3.2) for three different refinement levels. Table A1 shows these global wind parameters, along with the total number of computational cells and smallest cell size for each refinement level. In our grid design, the grid refinement changes occur in the simulation region close to the surface of the star, so that the grid size out beyond $10R_*$ remains the same.

The values of the wind parameters are seen to vary across refinement levels, and these variations are on the same order as the variations observed across epochs, or greater as in the case of mass loss rate. However, these variations are much smaller than the

Table A1. This table shows the changes in the May 2011 global wind parameters with differing grid refinement levels. These variations are on similar to or greater than the variation between epochs. As such it is important to ensure that the grid levels are the same when comparing global wind properties between simulations.

Grid refinement level	Total number of cells	Smallest cell ($\times 10^{-2}$ R_*)	$\dot{M}$ (10^{-12} $M_\odot$ yr^{-1})	$\dot{J}$ (10^{32} erg)	$f_{\rm open}$
8	2.78×10^6	5.7	2.9	1.8	0.35
9	7.10×10^6	2.9	2.5	1.5	0.23
10	3.92×10^7	1.4	2.3	1.3	0.22

Downloaded from http://mnras.oxfordjournals.org/ at University of Southern Queensland on May 3, 2016

Table A2. This table shows the changes in the May 2011 local wind environment around τ Boo b with differing grid refinement levels. The variation in due to grid refinement level is on the same level or greater than the variation epoch to epoch. As such it is important to ensure that the grid levels are the same when comparing wind models across epochs.

Grid refinement level	$\|\mathbf{u}\|$ (km s^{-1})	$\|\mathbf{B}\|$ ($\times 10^{-2}$ G)	$P_{\rm tot}$ ($\times 10^{-3}$ dyn cm^{-2})	$R_{\rm m}/R_{\rm p}$
8	230	1.46	1.18	3.47
9	221	2.15	1.08	3.58
10	215	2.46	1.06	3.64

observational uncertainties and theoretical limits of both $\dot{M}$ and $\dot{J}$. The changes in $f_{\rm open}$ are not unexpected as the finer cell structure means that more of the magnetic field structure is being resolved, and field lines that could be taken to be open in a coarser grid structure are found to be closed at a higher refinement level.

Table A2 shows the changes in the simulation results at the position of τ Boo b due to changes in grid refinement. As with the global wind properties, the local wind properties at the planet vary between grid sizes on the same scale as variations between epochs. Even though it might appear that an under-resolved grid overestimates the impact of the wind on the planet, these variations are smaller than the observational uncertainties on these parameters.

Given the variations seen due to different grid sizes it is important to use the same grid refinement level to compare simulations of different epochs. Using a higher resolution would give marginally more accurate results, but given the unreasonable amount for computation requires to reach refinement level 11 (total number of cells $\sim 2.86 \times 10^8$), we conclude that refinement level 10 is the most appropriate for the current study.

This paper has been typeset from a TEX/LATEX file prepared by the author.

Downloaded from http://mnras.oxfordjournals.org/ at University of Southern Queensland on May 3, 2016

5 Conclusions

This thesis explores the use of high resolution spectropolarimetry to study the dynamo generation of magnetic fields and resulting winds from young, low-mass stars, and the implications for detecting and characterising planetary systems. Detailed analysis of observations of a sample of four weak-line T Tauri stars reveal information about their magnetic fields, surface activity, and role of activity in searching for close-in giant planets. In addition, a time series of magnetic field observations spanning more than half a decade are used to infer changes in the stellar wind of a young, solar-type star across multiple magnetic cycles, and the potential impacts of the wind on its orbiting giant planet.

5.1 The Surface Magnetic Activity of Low-Mass, Pre-Main-Sequence Stars

A majority of this thesis focuses of the study of 4 wTTSs: V1095 Sco, TWA 7, TWA 9A and TWA 25, and their parameters are summarised in Table 5.1 below. The study

of the surface brightness reconstructed for three of the four stars reveals a variety of morphologies, from multiple mid-to-low latitude spots in the case of TWA 25, to a single, polar spot in the case of V1095 Sco. The brightness morphology of V1095 Sco, as well as for a number of other MaTYSSE wTTSs is consistent with polar spot phenomena observed and predicted for rapidly rotating stars (Schuessler & Solanki, 1992; Yadav et al., 2015). However, not all MaTYSSE wTTSs display polar spots, even the stars classed as rapid rotators.

The large-scale field is reconstructed for three of the four wTTS in this sample, namely TWA 7, TWA 9A and TWA 25. Their magnetic field morphologies all differ, with also TWA 25 having the highest ratio of toroidal to poloidal field energy of any MaTYSSE stars observed to date. There is also a range of poloidal field axisymmetry displayed within the sample ranging form 51% axisymmetric down to only 0.06% axisymmetric. All stars in this sample display a dipolar field offset from the stellar rotation axis. This implies that any surround debris disc or planetary system will be experiencing a variable stellar magnetic field as the star rotates.

The magnetic field studies in this thesis support the broader findings of the MaTYSSE large programme that wTTS magnetic field morphologies are more diverse than those of cTTSs, and that wTTS magnetic field topologies have no apparent trend with internal structural evolution. This lack of apparent trend is in contrast to the results from the MaPP cTTS sample (Gregory et al., 2012), and the dynamo simulation results of Emeriau-Viard & Brun (2017), which both indicate a correlation between field topology and the development of a substantial radiative core. These differences in the observed magnetic field behaviour of wTTS and cTTS suggests potential differences in the dynamos of accreting and non-accreting stars. It is interesting to note, however, that the dynamo models of Emeriau-Viard & Brun (2017) do not include accretion processes in their simulations, and yet produce results that are only consistent for the observed sample of accreting stars. Given MaTYSSE has selected for wTTS that overlap in ages and evolutionary states with the MaPP cTTSs, this has also selected for targets that have rapidly cleared their discs. Thus the important differences between the cTTS and wTTS samples may not be the presence of accretion, but the speed at which

Table 5.1: Summary of the properties of stars analysed in Chapters 2 and 3. Uncertainties are given where available. Spectral types estimated from effective temperatures using the conversion table of Herczeg & Hillenbrand (2014). References: [1] Mentuch et al. (2008)

	TWA 9A	V1095 Sco.	TWA 25	TWA 7
M_* ($M_\odot$)	1.00 ± 0.1	$0.96^{+0.05}_{-0.08}$	$0.67^{+0.06}_{-0.2}$	0.4 ± 0.1
$R_* \sin i$, ($R_\odot$)	1.070 ± 0.003	1.75 ± 0.03	1.330 ± 0.003	0.510 ± 0.005
R_* ($R_\odot$)	$1.2^{+0.3}_{-0.2}$	$2.5^{+0.4}_{-0.5}$	1.2 ± 0.4	0.82 ± 0.13
Age (Myrs)	10^{+13}_{-5}	$0.9^{+1.1}_{-0.4}$	5^{+35}_{-4}	10^{+26}_{-7}
L_* ($L_\odot$)	0.5 ± 0.2	2.0 ± 0.7	0.3 ± 0.1	0.09 ± 0.02
Distance, (pc)	76.4 ± 0.3	162 ± 1	53.1 ± 0.2	34.03 ± 0.08
$v \sin(i)$ (km s^{-1})	10.8 ± 0.02	30.6 ± 0.1	13.32 ± 0.01	5.15 ± 0.05
$P_{\rm rot}$ (d)	5.01 ± 0.01	2.9 ± 0.05	5.05 ± 0.01	5.01 ± 0.01
$T_{\rm eff}$ (K)	4400 ± 50	4350 ± 50	3920 ± 150 [1]	3541 ± 150 [1]
$\log(g)$	4.1 ± 0.2	3.8 ± 0.2	4.45 ± 0.5 [1]	4.18 ± 0.5 [1]
Spectral Type	K4	K4	M0	M2
$\langle B \rangle$ (G)	113	N/A	270	65
% Pol.	0.68	N/A	0.25	0.41
% Axisymm.	0.27	N/A	0.06	0.51

the star has cleared its disc. Simulations of the magnetic field in low mass stars report a 'bistability' in the dynamo simulations (Simitev & Busse, 2009), where the resulting field configuration (either strong, poloidal and axisymmetric, or weak, toroidal, and non-axisymmetric) is sensitive to initial conditions, and a similar phenomenon may explain the behaviour evident here. The observed sample of T Tauri stars is still small, though, so more observations across a wider range of ages, masses and accretion rates are needed.

5.2 The wind of a solar-type star

A time series of reconstructed magnetic field maps from ZDI were used as boundary conditions to generate 3D MHD stellar wind simulations for the Star τ Boötis. These simulations showed that the changing magnetic field of τ Boo has a dramatic influence on the angular momentum loss rate, with values varying by more than a factor of 2 over the magnetic cycle. These changes in angular momentum loss rate were driven more by the changes in the total field strength rather than the changes in field complexity or

the fraction of open versus closed field lines.

Examining the wind simulations at the location of τ Boo b reveals its harsh space weather environment at all phases of the magnetic cycle. The dominating pressure on the planet was the magnetic pressure, which varied by up to 48%, inducing a factor of ~2 variation in the total pressure on the planet. Under the assumption of a Jupiter sized planetary magnetic field, this gave a magnetospheric radius of ~ 4 times the radius of the planet, and $\sim 15\%$ of the planet's surface area at the poles exposed to potential atmospheric stripping along open planetary magnetic field lines. These are far harsher conditions that what is experienced by Jupiter in our Solar system.

Since publication of Chapter 4, research by Mengel (2017) indicates that the magnetic field cycle of τ Boo is much shorter than previously thought, with a period of ~ 240 days. Such a short magnetic cycle thus means that the wind results presented in Chapter 4 extend over a larger number of magnetic cycles, but this does not alter the conclusions from this wind modelling.

Stellar winds are important to the study of planetary evolution and habitability (Vidotto et al., 2013). Thus, the wind study of this thesis needs to be expanded to a broader range of stars to gauge the impact of host star magnetic fields, winds and activity on young planetary systems. Furthermore, observational validation of both stellar wind and coronal properties are needed to better constrain these models and provide more robust absolute values for the key wind parameters, such as mass loss and angular momentum loss rates. Nevertheless, the ongoing study of young stellar dynamos though magnetic field mapping provides a basis for more empirically based and systematic studies of stellar winds across the HR diagram.

5.3 Giant Planets Around Young and Active Stars

The need to understand the early evolution of stars and their planetary systems provides the overarching scientific motivation for this thesis. A particular focus is on close-in giant planets and the magnetic behaviour of their host stars, achieved by studying a known hot Jupiter, τ Boo b, and the winds of its host τ Boo, as well as a search for

close-in giant planets around young stars.

The search for planets around young stars is technically challenging, because the magnetic activity of the star can obscure or mimic planetary signals. Large radial velocity amplitudes were evident for the wTTSs studied in this thesis, with RV RMS values ranging from 113 m s^{-1} for TWA 7 up to 495 m s^{-1} for TWA 25. For all but TWA 7, the RV amplitudes were reduced by characterising the star's surface brightness variations with DI and removing their RV contributions. This activity filtering led to large decreases in RV RMS, at least by a factor of $\sim$ 3 for V1095 Sco and up to a factor of $\sim$13 for TWA 25. While no planetary signals were detected in these RV data sets, upper limits were placed on the presence of giant planets in those systems. Even with these non-detections, the occurrence rate for giant close-in planets around young stars is still likely higher than the 1% found for MS stars Guo et al. (2017), with 2 detected (Donati et al., 2015; Yu et al., 2017) within the MaTYSSE sample of only a few tens of stars.

TWA 7 is an intriguing case in the search for young planets. This is because the sinusoidal variation in its radial velocities closely mimicked the signal of a close-in giant planet tidally locked to the stellar rotation period of 5 days. Rather than being from a planet, the observed signal is more likely to arise from low latitude star spots. Intriguingly, TWA 7 displays a lack of correlation between the rotational modulation of its chromospheric activity indices and the location of starspots on its surface. Such a lack of correlation is a problem for those seeking planets around active stars, and may be due to the high level of activity of such stars. Rotational modulation of plage emission has long been used to model stellar rotation. However, for more active stars, plage emission may be so widespread so as to no longer exhibit significant rotational modulation. In contrast, the spot on the surface continues to produce a measurable effect on the stellar radial velocity. While simultaneous multi-colour photometry could be used for spot monitoring, spectropolarimetry itself can be used to monitor rotational modulation, as has been demonstrated in Chapter 3. Spectropolarimetry of active stars thus offers double benefits: simultaneously enabling detailed studies of stellar activity and magnetic fields, as well as providing valuable information for robustly detecting

and characterising exoplanets around active stars, including newly formed planetary systems.

5.4 Future Work

If we are to genuinely understand planetary systems, more young planets will need to be found, so that the formation and evolution of planetary systems around different types of stars and in different environments can be surveyed. The challenge then is to expand on the current observed sample of young stars and their planets, applying existing and emerging (see e.g. Haywood et al., 2016) techniques to characterise stellar activity signals. The development of new techniques to better characterise and mitigate stellar signals in radial velocity or transit data will be vital, both for finding planets around active stars and Earth-like planets around quiescent, Sun-like stars.

M dwarfs are the most abundant type of star, and are important in the search for habitable exoplanets. These stars will be best studied by the next generation of infrared high-resolution spectropolarimetric instruments, SpIROU on the CFHT (Donati et al., 2018) and CRIRES+ on the ESO VLT (Follert et al., 2014). These instruments thus provide an excellent opportunity to investigate planet formation, evolution and habitability around the lowest mass stars. In addition to aiding the search for planets around cool stars, these instruments will aid in the study of stellar dynamos. Given the wavelength dependance of Zeeman splitting, the detection of Zeeman broadening and polarisation signatures is better in the operating wavelength of these new instruments compared with current generation of optical instruments. This will simultaneously allow better study of the dynamo activity of M dwarfs and low mass pre-main sequence stars, alongside exoplanetary studies.

NASA/MIT's Transiting Exoplanet Survey Satellite[1] (TESS) is a key new resource for both stellar astrophysics and exoplanetary science. TESS will perform a photometric survey of the nearest and brightest stars in the sky, and within the fields observed will be active, young stars. TESS will thus deliver a wealth of data on host stars and

[1] https://tess.mit.edu

their exoplanets, including systems where planets orbit active stars. Follow up of these interesting targets with high-resolution spectropolarimetric observations will be a key part of discovering and characterising young and formative planetary systems. For stars whose planets are detected by standard transit and radial velocity methods, spectropolarimetry will enable the observation of host star magnetic fields and activity for studies of planetary evolution and habitability. Furthermore, spectropolarimetry and accompanying active region mapping can enable the detection of planets around more active stars than the current standard methods allow. Spectropolarimetry will thus be a vital tool in understanding of the formation and early evolution of these cool stars and their planetary systems.

References

Note that the references presented here are for Chapters 1 and 5. References for the papers included in Chapters 2 - 4 are included in the references sections of the papers.

Alvarado-Gómez, J. D., Hussain, G. A. J., Cohen, O., Drake, J. J., Garraffo, C., Grunhut, J., & Gombosi, T. I. (2016). Simulating the environment around planet-hosting stars. Astronomy & Astrophysics, 588, A28.

Babcock, H. W. (1947). Zeeman effect in stellar spectra. The Astrophysical Journal, 105, 105–119.

Babcock, H. W. (1961). The topology of the Sun's magnetic field and the 22-year cycle. The Astrophysical Journal, 133, 572–587.

Bagnulo, S., Landolfi, M., Landstreet, J. D., Landi Degl'Innocenti, E., Fossati, L., & Sterzik, M. (2009). PASP, 121(883), 993–1015.

Baranne, A., Queloz, D., Mayor, M., Adrianzyk, G., Knispel, G., Kohler, D., Lacroix, D., Meunier, J.-P., Rimbaud, G., & Vin, A. (1996). ELODIE: A spectrograph for accurate radial velocity measurements. Astronomy & Astrophysics Supplement Series, 119, 373–390.

Berdyugina, S. V. (2005). Starspots: A key to the stellar dynamo. Living Reviews in Solar Physics, 2(1), 1–62.

Bertout, C. (1989). T Tauri Stars: Wild as Dust. Annual Review of Astronomy and Astrophysics, 27(1), 351–395.

Boisse, I., Moutou, C., Vidal-Madjar, A., Bouchy, F., Pont, F., Hébrard, G., Bonfils, X., Croll, B., Delfosse, X., Desort, M., Forveille, T., Lagrange, A.-M., Loeillet, B., Lovis, C., Matthews, J. M., Mayor, M., Pepe, F., Perrier, C., Queloz, D., Rowe, J. F., Santos, N. C., Ségransan, D., & Udry, S. (2009). Stellar activity of planetary host star HD 189 733. Astronomy & Astrophysics, 495(3), 959–966.

Brown, S. F., Donati, J.-F., Rees, D. E., & Semel, M. (1991). Zeeman-Doppler imaging of solar-type and Ap stars. IV. Maximum entropy reconstruction of 2D magnetic topologies. Astronomy & Astrophysics, 250, 463–474.

Brun, A. S. & Browning, M. K. (2017). Magnetism, dynamo action and the solar-stellar connection. Living Reviews in Solar Physics, 14(1), 4.

Butler, R. P. & Marcy, G. W. (1996). A planet orbiting 47 Ursae Majoris. The Astrophysical Journal, 464, L153–L156.

Carroll, B. W. & Ostlie, D. A. (2007). An introduction to modern astrophysics. Pearson Addision Wesley, second edition edition.

Charbonneau, P. & MacGregor, K. B. (1997). Solar Interface Dynamos. II. Linear, Kinematic Models in Spherical Geometry. The Astrophysical Journal, 486, 502–520.

Christiansen, J. L., Clarke, B. D., Burke, C. J., Jenkins, J. M., Bryson, S. T., Coughlin, J. L., Mullally, F., Thompson, S. E., Twicken, J. D., Batalha, N. M., Haas, M. R., Catanzarite, J., Campbell, J. R., Uddin, A. K., Zamudio, K., Smith, J. C., & Henze, C. E. (2016). MEASURING TRANSIT SIGNAL RECOVERY IN THE KEPLER PIPELINE. III. COMPLETENESS OF THE Q1–Q17 DR24 PLANET CANDIDATE CATALOG WITH IMPORTANT CAVEATS FOR OCCURRENCE RATE CALCULATIONS. The Astrophysical Journal, 828(2), 99.

Cohen, M. & Kuhi, L. V. (1979). Observational studies of pre-main-sequence evolution. The Astrophysical Journal Supplement Series, 41, 743.

Díaz, R. F., González, J. F., Cincunegui, C., & Mauas, P. J. D. (2007). The spectroscopic binary system Gl 375. Astronomy & Astrophysics, 474(2), 345–353.

Donati, J.-F. & Brown, S. F. (1997). Zeeman-Doppler imaging of active stars V. Sensitivity of maximum entropy magnetic maps to field orientation. Astronomy & Astrophysics, 326, 1135–1142.

Donati, J.-F., Collier Cameron, A., & Petit, P. (2003). Temporal fluctuations in the differential rotation of cool active stars. Monthly Notices of the Royal Astronomical Society, 345(4), 1187–1199.

Donati, J. F., Hebrard, E., Hussain, G., Moutou, C., Grankin, K., Boisse, I., Morin, J., Gregory, S. G., Vidotto, A. A., Bouvier, J., Alencar, S. H. P., Delfosse, X., Doyon, R., Takami, M., Jardine, M. M., Fares, R., Cameron, A. C., Menard, F., Dougados, C., Herczeg, G., & the MaTYSSE collaboration (2014). Modelling the magnetic activity and filtering radial velocity curves of young Suns : the weak-line T Tauri star LkCa 4. Monthly Notices of the Royal Astronomical Society, 444(4), 3220–3229.

Donati, J. F., Hebrard, E., Hussain, G. A. J., Moutou, C., Malo, L., Grankin, K., Vidotto, A. A., Alencar, S. H. P., Gregory, S. G., Jardine, M. M., Herczeg, G., Morin, J., Fares, R., Menard, F., Bouvier, J., Delfosse, X., Doyon, R., Takami, M., Figueira, P., Petit, P., Boisse, I., & the MaTYSSE collaboration (2015). Magnetic activity and hot Jupiters of young Suns: the weak-line T Tauri stars V819 Tau and V830 Tau. Monthly Notices of the Royal Astronomical Society, 453(4), 3706–3719.

Donati, J. F., Howarth, I. D., Jardine, M. M., Petit, P., Catala, C., Landstreet, J. D., Bouret, J. C., Alecian, E., Barnes, J. R., Forveille, T., Paletou, F., & Manset, N. (2006). The surprising magnetic topology of τ Sco: fossil remnant or dynamo output? Monthly Notices of the Royal Astronomical Society, 370(2), 629–644.

Donati, J.-F., Jardine, M. M., Gregory, S. G., Petit, P., Paletou, F., Bouvier, J., Dougados, C., Ménard, F., Collier Cameron, A., Harries, T. J., Hussain,

G. A. J., Unruh, Y., Morin, J., Marsden, S. C., Manset, N., Aurière, M., Catala, C., & Alecian, E. (2008). Magnetospheric accretion on the T Tauri star BP Tauri. Monthly Notices of the Royal Astronomical Society, 386, 1234–1251.

Donati, J.-F., Kouach, D., Lacombe, M., Baratchart, S., Doyon, R., Delfosse, X., Artigau, E., Moutou, C., Hébrard, G., Bouchy, F., Bouvier, J., Alencar, S., Saddlemyer, L., Parès, L., Rabou, P., Micheau, Y., Dolon, F., Barrick, G., Hernandez, O., Wang, S. Y., Reshetov, V., Striebig, N., Challita, Z., Carmona, A., Tibault, S., Martioli, E., Figueira, P., Boisse, I., & Pepe, F. (2018). SPIRou: A nIR Spectropolarimeter/High-precision Velocimeter for the CFHT, (pp. 1–27). Springer International Publishing: Cham.

Donati, J.-F. & Landstreet, J. (2009). Magnetic Fields of Nondegenerate Stars. Annual Review of Astronomy and Astrophysics, 47(1), 333–370.

Donati, J. F., Moutou, C., Malo, L., Baruteau, C., Yu, L., Hébrard, E., Hussain, G., Alencar, S., Ménard, F., Bouvier, J., Petit, P., Takami, M., Doyon, R., & Cameron, A. C. (2016). A hot Jupiter orbiting a 2-million-year-old solar-mass T Tauri star. Nature, 534, 662–666.

Donati, J.-F., Semel, M., Carter, B. D., Rees, D. E., & Cameron, A. C. (1997). Spectropolarimetric observations of active stars. Monthly Notices of the Royal Astronomical Society, 291, 658–682.

Donati, J.-F., Yu, L., Moutou, C., Cameron, A. C., Malo, L., Grankin, K., Hébrard, E., Hussain, G. A. J., Vidotto, A. A., Alencar, S. H. P., Haywood, R. D., Bouvier, J., Petit, P., Takami, M., Herczeg, G. J., Gregory, S. G., Jardine, M. M., & Morin, J. (2017). The hot Jupiter of the magnetically active weak-line T Tauri star V830 Tau. Monthly Notices of the Royal Astronomical Society, 465, 3343–3360.

Emeriau-Viard, C. & Brun, A. S. (2017). Origin and evolution of magnetic fields in PMS stars : influence of rotation and structural changes. The Astrophysical Journal, 846(1), 8.

Follert, R., Dorn, R. J., Oliva, E., Lizon, J. L., Hatzes, A., Piskunov, N., Reiners, A., Seemann, U., Stempels, E., Heiter, U., Marquart, T., Lockhart, M., Anglada-Escude, G., Löwinger, T., Baade, D., Grunhut, J., Bristow, P., Klein, B., Jung, Y., Ives, D. J., Kerber, F., Pozna, E., Paufique, J., Kaeufl, H. U., Origlia, L., Valenti, E., Gojak, D., Hilker, M., Pasquini, L., Smette, A., & Smoker, J. (2014). CRIRES+: a cross-dispersed high-resolution infrared spectrograph for the ESO VLT. In Ground-based and Airborne Instrumentation for Astronomy V, volume 9147 of SPIE proceedings (pp. 914719).

Folsom, C. P., Bouvier, J., Petit, P., Lèbre, A., Amard, L., Palacios, A., Morin, J., Donati, J.-F., & Vidotto, A. A. (2018). The evolution of surface magnetic fields in young solar-type stars II: the early main sequence (250-650 Myr). Monthly Notices of the Royal Astronomical Society, 474, 4956–4987.

Folsom, C. P., Petit, P., Bouvier, J., Lèbre, A., Amard, L., Palacios, A., Morin, J., Donati, J. F., Jeffers, S. V., Marsden, S. C., & Vidotto, A. A. (2016). The evolution of surface magnetic fields in young solar-type stars – I. The first 250 Myr. Monthly Notices of the Royal Astronomical Society, 457(1), 580–607.

Gallet, F. & Bouvier, J. (2013). Improved angular momentum evolution model for solar-like stars. Astronomy & Astrophysics, 556, A36.

Giles, H. A. C., Collier Cameron, A., & Haywood, R. D. (2017). A Kepler study of starspot lifetimes with respect to light-curve amplitude and spectral type. Monthly Notices of the Royal Astronomical Society, 472(2), 1618–1627.

Gomes da Silva, J., Santos, N. C., Bonfils, X., Delfosse, X., Forveille, T., & Udry, S. (2011). Long-term magnetic activity of a sample of M-dwarf stars from the HARPS program. I. Comparison of activity indices. Astronomy & Astrophysics, 534, A30.

Gray, D. F. (2008). The Observation and Analysis of Stellar Photospheres. Third edition edition.

Gregory, S. G., Donati, J.-F., Morin, J., Hussain, G. A. J., Mayne, N. J., Hillenbrand, L. A., & Jardine, M. (2012). Can We Predict the Global Magnetic Topology of a Pre-Main-Sequence Star From Its Position in the Hertzsprung–Russell Diagram? The Astrophysical Journal, 755(2), 97.

Guerrero, G., Smolarkiewicz, P. K., de Gouveia Dal Pino, E. M., Kosovichev, A. G., & Mansour, N. N. (2016). On the Role of Tachoclines in Solar and Stellar Dynamos. The Astrophysical Journal, 819, 104.

Guo, X., Johnson, J. A., Mann, A. W., Kraus, A. L., Curtis, J. L., & Latham, D. W. (2017). The Metallicity Distribution and Hot Jupiter Rate of the Kepler Field: Hectochelle High-resolution Spectroscopy for 776 Kepler Target Stars. The Astrophysical Journal, 838, 25.

Haywood, R. D., Collier Cameron, A., Unruh, Y. C., Lovis, C., Lanza, A. F., Llama, J., Deleuil, M., Fares, R., Gillon, M., Moutou, C., Pepe, F., Pollacco, D., Queloz, D., & Ségransan, D. (2016). The Sun as a planet-host star: Proxies from SDO images for HARPS radial-velocity variations. Monthly Notices of the Royal Astronomical Society, 457(4), 3637–3651.

Herczeg, G. J. & Hillenbrand, L. A. (2014). an Optical Spectroscopic Study of T Tauri Stars. I. Photospheric Properties. The Astrophysical Journal, 786(2), 97.

Hotta, H., Rempel, M., & Yokoyama, T. (2016). Large-scale magnetic fields at high Reynolds numbers in magnetohydrodynamic simulations. Science, 351, 1427–1430.

Hussain, G. A. J., Alvarado-Gómez, J. D., Grunhut, J., Donati, J.-F., Alecian, E., Oksala, M., Morin, J., Fares, R., Jardine, M., Drake, J. J., Cohen, O., Matt, S., Petit, P., Redfield, S., & Walter, F. M. (2016). A spectropolarimetric study of the planet-hosting G dwarf, HD 147513. Astronomy & Astrophysics, 585, A77.

Hussain, G. A. J., Donati, J.-F., Collier Cameron, A., & Barnes, J. R. (2000). Comparisons of images derived from independent Zeeman Doppler imaging codes. Monthly Notices of the Royal Astronomical Society, 318, 961–973.

Kippenhahn, R., Weigert, A., & Weiss, A. (2012). Stellar Structure and Evolution.

Landman, D. A. (1981). Measurements of He D3 profiles in solar plages. The Astrophysical Journal, 244, 345.

Lean, J. (1997). THE SUN'S VARIABLE RADIATION AND ITS RELEVANCE FOR EARTH. Annual Review of Astronomy and Astrophysics, 35(1), 33–67.

Marsden, S. C., Petit, P., Jeffers, S. V., Morin, J., Fares, R., Reiners, A., Do Nascimento, J. D., Auri??re, M., Bouvier, J., Carter, B. D., Catala, C., Dintrans, B., Donati, J. F., Gastine, T., Jardine, M., Konstantinova-Antova, R., Lanoux, J., Ligni??res, F., Morgenthaler, A., Ram??rez-V??lez, J. C., Th??ado, S., & Van Grootel, V. (2014). A BCool magnetic snapshot survey of solar-type stars. Monthly Notices of the Royal Astronomical Society, 444(4), 3517–3536.

Mathys, G. (1989). The Observation of Magnetic Fields in Nondegenerate Stars. Fundamentals of Cosmic Physics, 13, 143–308.

Mauas, P. J. D. (2000). Building Reliable Models of M Dwarf Chromospheres: The Spectral Diagnostics. The Astrophysical Journal, 539(2), 858–864.

Mengel, M. (2017). THE LARGE-SCALE MAGNETIC FIELDS OF PLANET-HOSTING SOLAR-TYPE STARS. PhD thesis, University of Southern Queensland.

Mentuch, E., Brandeker, A., van Kerkwijk, M., Jayawardhana, R., & Hauschildt, P. (2008). Lithium Depletion of Nearby Young Stellar Associations. The Astrophysical Journal, 689(2006), 1127–1140.

Navascués, D. B. y. & Martín, E. L. (2003). An Empirical Criterion to Classify T Tauri Stars and Substellar Analogs Using Low-Resolution Optical Spectroscopy. The Astronomical Journal, 126(6), 2997–3006.

Newton, E. R., Irwin, J., Charbonneau, D., Berlind, P., Calkins, M. L., & Mink, J. (2017). THE H α EMISSION OF NEARBY M DWARFS AND ITS RELATION TO STELLAR ROTATION. The Astrophysical Journal, 834(1), 85.

Nicholson, B. A., Hussain, G. A. J., Donati, J.-F., Folsom, C. P., Mengel, M., Carter, B. D., & Wright, D. (2018). The surface magnetic activity of the weak-line T Tauri stars TWA 9A and V1095 Sco. Monthly Notices of the Royal Astronomical Society, 480(2), 1754–1766.

Nicholson, B. A., Vidotto, A. A., Mengel, M., Brookshaw, L., Carter, B., Petit, P., Marsden, S. C., Jeffers, S. V., & Fares, R. (2016). Temporal variability of the wind from the star τ Boötis. Monthly Notices of the Royal Astronomical Society, 459(2), 1907–1915.

Noyes, R. W., Weiss, N. O., & Vaughan, A. H. (1984). The relation between stellar rotation rate and activity cycle periods. The Astrophysical Journal, 287, 769.

Parker, E. N. (1993). A solar dynamo surface wave at the interface between convection and nonuniform rotation. The Astrophysical Journal, 408, 707–719.

Pepe, F., Mayor, M., Galland, F., Naef, D., Queloz, D., Santos, N. C., Udry, S., & Burnet, M. (2002). The CORALIE survey for southern extra-solar planets VII. Astronomy & Astrophysics, 388(2), 632–638.

Petit, P., Donati, J. F., & Collier Cameron, A. (2002). Differential rotation of cool active stars: the case of intermediate rotators. Monthly Notices of the Royal Astronomical Society, 334(2), 374–382.

Petit, P., Donati, J.-F., & the ESPaDOnS Project Team (2003). Magnetism and activity of the sun and stars. In J. Arnaud & N. Meunier (Eds.), Magnetism and Activity of the Sun and Stars, volume 9 of EAS Pub. Ser. (pp.97).

Powell, K. G., Roe, P. L., Linde, T. J., Gombosi, T. I., & De Zeeuw, D. L. (1999). A Solution-Adaptive Upwind Scheme for Ideal Magnetohydrodynamics. Journal of Computational Physics, 154(2), 284–309.

Reiners, A. (2010). Magnetic Fields on Cool Stars. arXive:1012.1183v1 [astro-ph.SR], (pp.12).

Reiners, A. (2012). Observations of Cool-Star Magnetic Fields. Living Reviews in Solar Physics, 9.

Rüdiger, G., Elstner, D., & Ossendrijver, M. (2003). Do spherical α^2-dynamos oscillate? Astronomy & Astrophysics, 406, 15–21.

Schuessler, M. & Solanki, S. K. (1992). Why rapid rotators have polar spots. Astronomy & Astrophysics, 264, L13–L16.

Semel, M. (1989). Zeeman-Doppler imaging of active stars. I – Basic principles. Astronomy & Astrophysics, 225, 456–466.

Semel, M., Donati, J.-F., & Rees, D. E. (1993). Zeeman-Doppler imaging of active stars. 3: Instrumental and technical considerations. Astronomy & Astrophysics, 278, 231–237.

Simitev, R. D. & Busse, F. H. (2009). Bistability and hysteresis of dipolar dynamos generated by turbulent convection in rotating spherical shells. EPL (Europhysics Letters), 85(1), 19001.

Skumanich, A. (1972). Time Scales for CA II Emission Decay, Rotational Braking, and Lithium Depletion. The Astrophysical Journal, 171(Frazier 1970), 565.

Tóth, G., Sokolov, I. V., Gombosi, T. I., Chesney, D. R., Clauer, C. R., De Zeeuw, D. L., Hansen, K. C., Kane, K. J., Manchester, W. B., Oehmke, R. C., Powell, K. G., Ridley, A. J., Roussev, I. I., Stout, Q. F., Volberg, O., Wolf, R. A., Sazykin, S., Chan, A., Yu, B., & Kóta, J. (2005). Space Weather Modeling Framework: A new tool for the space science community. Journal of Geophysical Research, 110(A12), A12226.

Tóth, G., van der Holst, B., Sokolov, I. V., De Zeeuw, D. L., Gombosi, T. I., Fang, F., Manchester, W. B., Meng, X., Najib, D., Powell, K. G., Stout, Q. F., Glocer, A., Ma, Y.-J., & Opher, M. (2012). Adaptive numerical algorithms in space weather modeling. Journal of Computational Physics, 231(3), 870–903.

Vidotto, A. A. & Donati, J.-F. (2017). Predicting radio emission from the newborn hot Jupiter V830 Tauri b and its host star. Astronomy & Astrophysics, 602, A39.

Vidotto, A. A., Fares, R., Jardine, M., Donati, J.-F., Opher, M., Moutou, C., Catala, C., & Gombosi, T. I. (2012). The stellar wind cycles and planetary radio emission of the τ Boo system. Monthly Notices of the Royal Astronomical Society, 423, 3285–3298.

Vidotto, A. A., Jardine, M., Morin, J., Donati, J. F., Lang, P., & Russell, A. J. B. (2013). Effects of M dwarf magnetic fields on potentially habitable planets. Astronomy & Astrophysics, 67, 1–11.

Vidotto, A. A., Opher, M., Jatenco-Pereira, V., & Gombosi, T. I. (2014). Interactions between exoplanets and the winds of young stars. EPJ Web of Conferences, 64, 4006.

Walsh, B. M., Welling, D. T., Zou, Y., & Nishimura, Y. (2018). A Maximum Spreading Speed for Magnetopause Reconnection. Geophysical Research Letters, 45(11), 5268–5273.

Wargelin, B. J. & Drake, J. J. (2001). Observability of Stellar Winds from Late-Type Dwarfs via Charge Exchange X-Ray Emission. The Astrophysical Journal Letters, 546, L57–L60.

Wood, B. E. (2004). Astrospheres and Solar-like Stellar Winds. Living Reviews in Solar Physics, 1.

Wright, N. J., Drake, J. J., Mamajek, E. E., & Henry, G. W. (2011). The Stellar-Activity-Rotation Relationship and the Evolution of Stellar Dynamos. The Astrophysical Journal, 743(1), 48.

Wright, N. J., Newton, E. R., Williams, P. K. G., Drake, J. J., & Yadav, R. K. (2018). The stellar rotation–activity relationship in fully convective M dwarfs. Monthly Notices of the Royal Astronomical Society, 479(2), 2351–2360.

Yadav, R. K., Gastine, T., Christensen, U. R., & Reiners, A. (2015). Formation of starspots in self-consistent global dynamo models: Polar spots on cool stars. Astronomy & Astrophysics, 573, A68.

Yu, L., Donati, J.-F., Hébrard, E. M., Moutou, C., Malo, L., Grankin, K., Hussain, G., Collier Cameron, A., Vidotto, A. A., Baruteau, C., Alencar, S., Bouvier, J., Petit, P., Takami, M., Herczeg, G., Gregory, S. G., Jardine, M., Morin, J., & Ménard, F. (2017). A hot Jupiter around the very active weak-line T Tauri star TAP 26. Monthly Notices of the Royal Astronomical Society, 467, 1342.

This page intentionally left blank.